Experimental and Numerical Study of a Novel Airfoil Morphing Concept for UAV Wings

(versão final após defesa)

Egor Ukolov

Dissertação para obtenção do Grau de Mestre em
Engenharia Aeronáutica
(mestrado integrado)

Orientador: Prof. Doutor Pedro Vieira Gamboa

dezembro de 2024

Declaração de Integridade

Eu, Egor Ukolov, que abaixo assino, estudante com o número de inscrição 43882 de/o Mestrado Integrado em Engenharia Aeronáutica da Faculdade de Engenharia, declaro ter desenvolvido o presente trabalho e elaborado o presente texto em total consonância com o **Código de Integridades da Universidade da Beira Interior**.

Mais concretamente afirmo não ter incorrido em qualquer das variedades de Fraude Académica, e que aqui declaro conhecer, que em particular atendi à exigida referenciação de frases, extratos, imagens e outras formas de trabalho intelectual, e assumindo assim na íntegra as responsabilidades da autoria.

Universidade da Beira Interior, Covilhã 20/12/2024

Ukolov

Acknowledgements

I would like to express my deepest gratitude to my parents, whose unwavering love, encouragement, and belief in me have been a constant source of strength throughout this journey. Their support has been fundamental not only during the completion of this thesis, but also throughout my academic and personal growth.

I would also like to extend my heartfelt thanks to Professor Pedro Gamboa for his invaluable mentorship, support, and availability. Your insightful guidance and constructive feedback have been instrumental in shaping this work. Your dedication and willingness to share your knowledge have greatly enriched my learning experience, and I am deeply appreciative of the time and effort you have invested in my research.

Furthermore, I would like to thank all my professors for their continued support throughout my studies. I am particularly grateful to Professor Miguel Silvestre for his mentorship and encouragement in extracurricular university projects. Your guidance and enthusiasm have been pivotal in my academic journey.

Resumo

O processo de projeto convencional de uma aeronave resulta numa solução de compromisso de uma geometria das suas asas que atende a todos os requisitos de projeto e garante um desempenho satisfatório em todo o seu envelope de operação. Consequentemente, a aeronave pode operar em condições sub-ótimas do seu desempenho em várias condições de voo. A presente dissertação apresenta um conceito novo para executar o morphing na componente do perfil alar de uma asa, que tem potencial para aplicação em aeronaves não-tripuladas de tamanho pequeno-médio, de forma a melhorar o seu desempenho de voo numa maior gama de condições de voo.

Um surrogate model é desenvolvido de forma a avaliar as variáveis de projeto do conceito mais importantes nas métricas de desempenho aerodinâmico – coeficiente de sustentação máximo, eficiência aerodinâmica máxima e o correspondente coeficiente de momento de arfagem. Um protótipo do conceito é implementado de forma a executar a prova do conceito e comparar os resultados da atuação experimental de morphing com os resultados obtidos numericamente com um modelo computacional. Casos de estudo são analisados com os perfis alares “NACA 2412”, “NACA 2415” e “NACA 4418” de forma a analisar com maior detalhe os potenciais benefícios de morphing, e uma comparação dos desempenhos do conceito e de superfícies articuladas convencionais é realizada.

Os resultados mostram que o conceito tem capacidade para aumentar a eficiência aerodinâmica numa gama considerável de coeficientes de sustentação e reduzir, em valor absoluto, o coeficiente de momento de arfagem. O conceito ainda permite atingir um coeficiente de sustentação máximo 12% superior e uma eficiência aerodinâmica máxima 88% superior a uma superfície articulada convencional. O estudo conclui que uma potencial implementação prática do conceito permite reduzir as distâncias de aterragem e descolagem, reduzir o requisito de potência instalada, aumentar o alcance e a autonomia, e permitir a uma aeronave operar em diferentes condições de peso eficientemente.

Palavras-chave

Morphing, Perfil alar, Surrogate model, Kriging, Eficiência aerodinâmica.

Abstract

The conventional aircraft design process results in a compromise solution for its wings geometry that meets all design requirements and ensures satisfactory performance throughout its operational envelope. Consequently, the aircraft may operate under suboptimal performance conditions in various flight conditions. This dissertation presents a novel concept for executing wing morphing in its airfoil degree-of-freedom, which has the potential applications in small-to-medium size unmanned aerial vehicles, aimed at enhancing their flight performance across a broader range of flight conditions.

A surrogate model is developed to evaluate the most significant design variables of the concept in relation to aerodynamic performance metrics – maximum lift coefficient, maximum lift-to-drag ratio, and the corresponding pitching moment coefficient. A prototype of the concept is implemented to demonstrate proof-of-concept and compare the experimental results of morphing actuation with those obtained numerically from a computational model. Case studies are conducted using the airfoils “NACA 2412”, “NACA 2415”, and “NACA 4418” to further investigate the potential benefits of morphing, alongside a comparison of the concept’s performance with conventional hinged surfaces.

The results indicate that the concept is capable of enhancing lift-to-drag ratio across a considerable range of lift coefficients and reducing, in absolute value, the pitching moment coefficient. Furthermore, the concept allows for achieving a 12% higher maximum lift coefficient and an 88% higher maximum lift-to-drag ratio than that of a conventional hinged surface. The study concludes that the potential practical implementation of the concept can reduce take-off and landing distances, decrease the installed power requirements, extend range and endurance, and enable an aircraft to operate efficiently under varying weight conditions.

Keywords

Morphing, Airfoil, Surrogate model, Kriging, Lift-to-drag ratio.

Contents

List of Figures

List of Tables

Acronyms and Abbreviations

ABS	Acrylonitrile Butadiene Styrene
CFD	Computational Fluid Dynamics
CFRP	Carbon Fibre Reinforced Polymer
CHS	Conventional Hinged Surface
EMC	Elastomeric Matrix Composite
FDM	Finite Differences Method
FEM	Finite Element Method
FFS	Full Factorial Sampling
LDS	Low-Discrepancy Sequences
LHS	Latin Hypercube Sampling
LSM	Least Squares Method
MLE	Maximum Likelihood Estimation
PLA	Polylactic Acid
PVA	Polyvinyl Alcohol
NPC	Node-to-Point Contact
SMA	Shape Memory Alloy
SU	Soviet Union
UAV	Unmanned Aerial Vehicle
USA	United States of America

Symbols

Latin Symbols

A_t	Specimen cross-sectional area	$[m^2]$
$A_{t,min}$	Specimen minimum cross-sectional area	$[m^2]$
b_f	Flexural test specimen width	$[m]$
b_t	Tensile test specimen width	$[m]$
c_{HS}	Chord ratio of a conventional hinged surface	–
C_d	Drag coefficient	–
C_l	Lift coefficient	–
C_{l,α_0}	Lift coefficient at zero angle-of-attack	–
$C_{l,max}$	Maximum lift coefficient	–
C_l/C_d	Lift-to-drag ratio	–
$(C_l/C_d\ )_{max}$	Maximum lift-to-drag ratio	–
$C_{m_{(C_l/C_d\ )_{max}}}$	Pitching moment coefficient at the maximum lift-to-drag ratio	–
d	Distance between two sampling points	–
d_f	Specimen midspan deflection	$[m]$
d_p	Distance between two sampling points using the *p-norm* of the space	–
d_t	Tensile displacement	$[m]$
d_{TE}	Trailing-edge perpendicular-to-chord displacement relative to the chord	–
D	Design space	–
E_f	Flexural modulus of elasticity	$[N/m^2]$
E_t	Tensile modulus of elasticity	$[N/m^2]$

f	Objective function	–
$\hat{f}$	Approximation function	–
f_{LS}	Lower surface stringer distributed force	$[N/m]$
f_{US}	Upper surface stringer distributed force	$[N/m]$
h	Step size in the Finite Differences Method	–
I	Electrical current	$[A]$
I_{LS}	Lower surface servomotor input current	$[A]$
I_{US}	Upper surface servomotor input current	$[A]$
J	Number of pairs of points in a sampling plan separated by d_p	–
k	Number of design variables	–
k_T	Motor torque constant	$[N \cdot m/A]$
l_{CH}	Control horn length	$[m]$
L	Loss function	–
L_f	Support span in the flexural test	$[m]$
L_t	Specimen length	$[m]$
m	Number of sampling points	–
m_{te}	Number of model testing points	–
m_{tr}	Number of model training points	–
n_b	Number of basis functions	–
n_s	Number of specimens	–
o	Polynomial order	–
p	Kriging model parameter	–
P_f	Transversal load	$[N]$
P_t	Tensile load	$[N]$
q_f	Cross validation number of folds	–
r^2	Correlation coefficient	–
Re	Reynolds number	–
$RMSE$	Root Mean Squared Error	–
SD	Standard Deviation	–
t_f	Flexural test specimen thickness	$[m]$

t_t	Tensile test specimen thickness	$[m]$
T	Torque	$[N \cdot m]$
T_{out}	Servomotor output torque	$[N \cdot m]$
T_{LS}	Lower surface servomotor output torque	$[N \cdot m]$
T_{US}	Upper surface servomotor output torque	$[N \cdot m]$
w	Polynomial term coefficient	$-$
$\boldsymbol{w}$	Polynomial term coefficients vector	$-$
W_{supp}	Weight supported by the servomotor	$[N]$
x	Design variable	$-$
$\boldsymbol{x}$	Design variables vector	$-$
x'	Normalized design variable	$-$
x_{max}	Design variable maximum value	$-$
x_{min}	Design variable minimum value	$-$
x_{LS}	Lower surface stringer placement	$-$
x_{US}	Upper surface stringer placement	$-$
x_{WS}	Wing spar placement	$-$
$\boldsymbol{X}$	Sampling plan	$-$
y	Value of the objective function	$-$
Z	Material generic property	$-$

Greek Symbols

α	Angle-of-attack	$[deg]$
δ_{HS}	Conventional hinged surface deflection	$[deg]$
Δ	Change in a variable	$-$
ε_{cv}	Cross validation error	$-$
ε_{cvg}	Generalized cross validation error	$-$
ε_f	Flexural strain	$-$
ε_t	Tensile strain	$-$

θ	Kriging model parameter	$-$
Φ_q	Scalar-valued criterion function for competing sample plans ranking	$-$
ξ	Subset of sampling points	$-$
ψ	Basis function	$-$
σ_f	Flexural stress	$[N/m^2]$
$\sigma_{f,ult}$	Flexural strength	$[N/m^2]$
σ_t	Tensile stress	$[N/m^2]$
$\sigma_{t,ult}$	Tensile strength	$[N/m^2]$

Chapter 1

Introduction

This chapter aims to introduce the concept of morphing as applied to the aeronautical and aerospace sectors, with particular emphasis on aircraft wing morphing. It begins by defining the term "morphing" and providing a brief overview of its historical development, various types, advantages, and limitations, as well as the primary challenges associated with its implementation, that will constitute the motivation behind the present work. Subsequently, the dissertation's objectives are articulated, accompanied by an outline of the structure of the dissertation.

1.1 Motivation

The conventional aircraft design process typically prioritizes optimizing the geometry and shape of its wings for a specific flight condition, which dominates its operational envelope, with the cruise phase being the most prevalent. However, achieving compliance with all design requirements and ensuring satisfactory performance across the entire envelope of operation often necessitates compromises. Consequently, while a compromise solution is obtained, the aircraft may operate under sub-optimal conditions in other flight regimes. Inspired by birds' ability to adapt wings geometry to various flight conditions, researchers and engineers have conceived and often implemented mechanisms capable of executing morphing.

The term "morphing" derives from "metamorphose", yet there is no precise definition nor consensus among researchers regarding the extent or type of the geometrical changes required to classify an aircraft as a "shape morphing aircraft" [1-3]. There is not a clear definition for an enabling "shape morphing" technology either. Nonetheless, there is a general agreement that conventional hinged control surfaces and high lift devices, such as flaps or slats, that provide discrete geometry changes, cannot be considered as morphing mechanisms [2, 4].

More precisely, the term "morphing" is a discipline within smart structures and is associated with enhancing systems by providing them with additional capabilities to adapt to external changes [5]. Wing morphing specifically pertains to the alteration of the geometrical shape of the wings during operation in a continuous and smooth manner. Unlike a conventional aircraft with wings' geometry optimized for a single flight condition, morphing wings are designed to optimize their geometry for multiple flight conditions [6, 7], determined by specific factors such as airspeed, atmospheric properties, and aircraft weight. A morphing aircraft enhances the control authority, flight performance, and multi-mission capability by continuously adjusting its geometry [1, 8-11].

The concepts of wing morphing can be categorized into three primary groups based on the morphing's degree-of-freedom [1, 2, 7]: planform morphing, out-of-plane morphing, and airfoil morphing, as illustrated in *Figure 1.1*. In the first group, morphing degrees-of-freedom include changes in the wings' sweep, span, and chord. In the second group, morphing occurs through wings' twist, dihedral, and span bending changes. Finally, the third group involves potential modifications to the airfoil's camber and thickness.

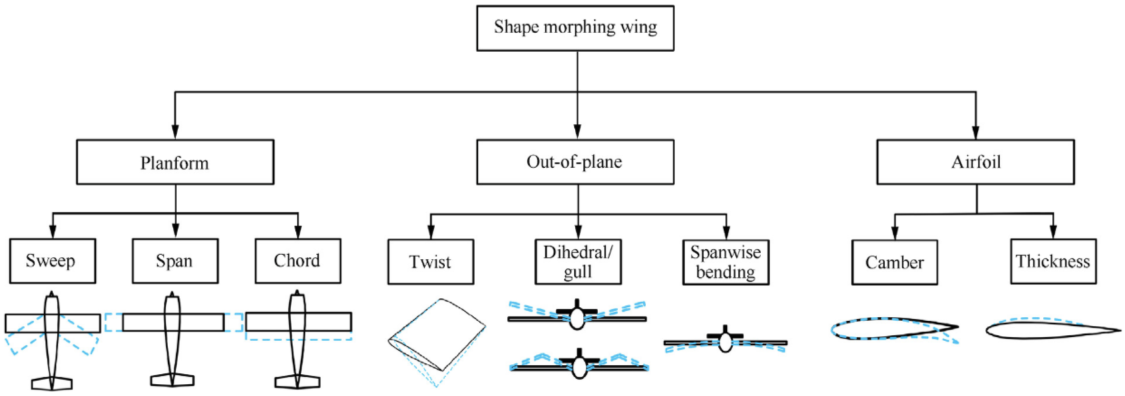

Figure 1.1 – Wing morphing degrees-of-freedom [12].

The idea of changing the geometry of aircraft wings is not a recent development. As evidenced by the "Wright Flyer" aircraft, which made its inaugural flight in 1903, it possessed the capability for roll control through the torsion of its wings, achieved using cables directly actuated by the pilot [13]. However, the growing demand for increased flight speeds and payloads necessitated the implementation of stiffer structures that limited their adaptability to varying its geometrical shape. As a result, the primary objective of aircraft design shifted from simply crating a flying-capable aircraft to developing one capable of safely, swiftly, efficiently, and stably completing its mission.

As the aircraft technology maturated, engineers faced increasingly demanding technical standards. It became essential not only to enhance some specifications of aircraft, such as increased flight velocity, flight altitude, and range, but also to develop the capability to fulfil various missions with conflicting requirements, including low and high-velocity flight, and cruise and combat missions. Since 1903, both the United States of America (USA) and the former Soviet Union (SU) embarked on investigations into morphing aircraft. To enhance aircraft endurance, shorten take-off and landing distances, and broaden the flight envelope to accommodate lower and higher airspeeds, the technology of varying the wing span was implemented in aircrafts like the *MAK-10*, *LIG-7*, and *MAK-123*. Similarly, to enable aircraft operation in both subsonic and supersonic regimes, the concept of varying wing sweep was introduced, exemplified by aircraft such as the *X-5*, *F-111*, *MIG-23*, and *F-14*.

Aircraft equipped with such technologies encountered issues with their morphing mechanisms. Additionally, with the development of more powerful engines, the technology of wing morphing ultimately proved less beneficial due to its inherent increase in structural weight, complexity, and risk of failure. Consequently, operating morphing aircraft became increasingly expensive. As a result, many of these projects were discontinued, leading to a slowdown in the development of wing morphing aircraft by the end of the 20th century. *Figure 1.2* illustrates some of the most significant morphing aircraft projects developed during the 20th century.

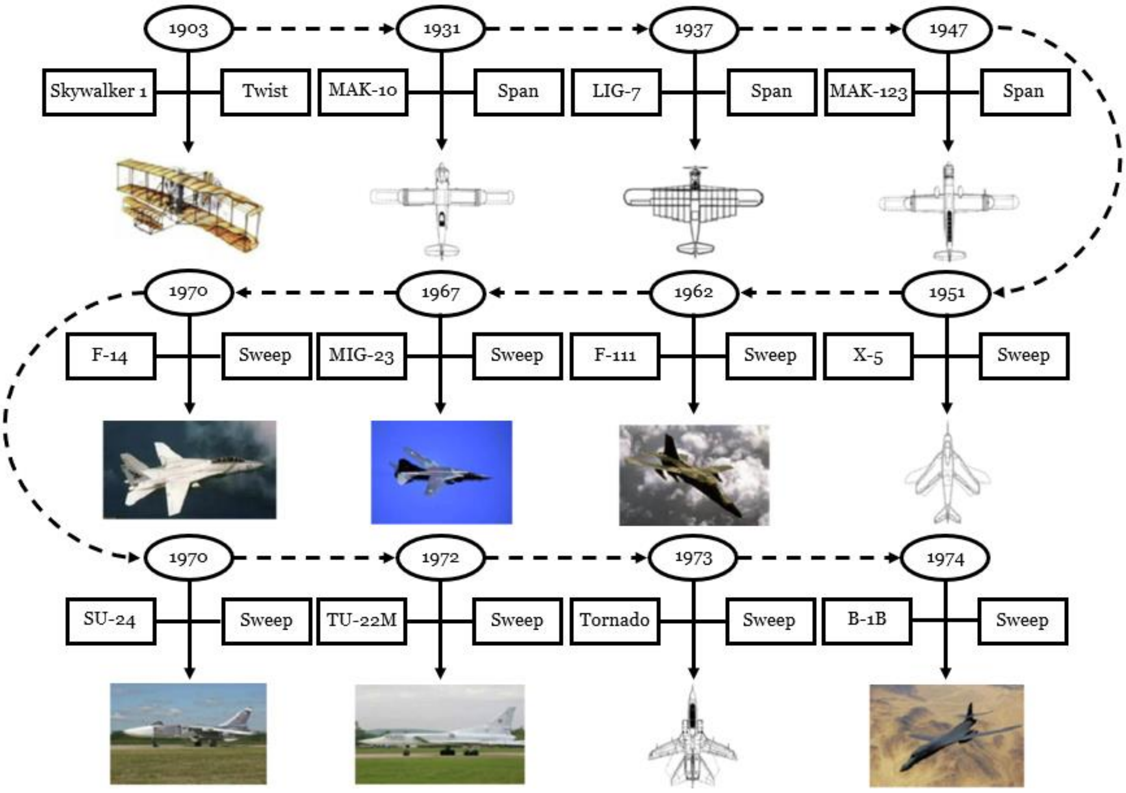

Figure 1.2 – Early important morphing aircraft projects, adapted from [13].

With the advent of smart materials and new structural technologies, the development of morphing aircraft received a new impetus, particularly in the realm of smaller aircraft, notably Unmanned Aerial Vehicles (UAVs). This trend was driven by the lower certification requirements and quality tests associated with smaller UAVs [1]. The demand for more efficient UAVs with variable mission profiles further fuelled this momentum, which was also facilitated by the simpler, faster, and more economical fabrication processes for smaller UAVs.

From the perspective of electric UAVs, which do not experience in-flight weight reduction due to energy consumption, the implementation of morphing technologies offers distinct advantages. These UAVs have the potential to operate effectively across various flight conditions and can enhance performance parameters during flight phases such as take-off, climb, acceleration, and landing. In recent years, there has been a notable increase in investment in cargo UAVs [14], which indeed operate across different flight conditions. For example, when conducting cargo drops, a morphing UAV could swiftly adapt to the new flight condition, showcasing its adaptability and versality.

From the perspective of commercial aviation, the imperative to reduce aircraft fuel consumption is becoming increasingly significant due to environmental concerns and cost considerations. For instance, even a modest 1% reduction in airfoil drag could yield substantial savings, with the USA fleet of wide-body transport aircraft potentially saving \$140 million per year, as estimated by Barbarino et al. [1] in 2011. Furthermore, for medium-range transport aircraft equipped with adaptive wings, projected fuel savings are anticipated to range between $3-5\%$, depending on mission distance. In practice, during the flight of fuel-powered commercial aircraft, weight decreases as fuel is consumed. Coupled with air traffic control restrictions, this results in the aircraft not flying under its optimal condition, thereby compromising its overall performance.

The conventional aircraft control surfaces such as ailerons, rudder, and elevator, along with high-lift devices like flaps and slats, possess the capability to alter the geometry of the wings. Specifically, high-lift devices can enhance aircraft performance during take-off and landing and enable the flight at lower airspeeds. However, despite their effectiveness in controlling airflow, these conventional hinged surfaces are not as efficient due to the presence of hinges and other junctions, which create discontinuities in the surface. These discontinuities can lead to unwanted fluid dynamic phenomena [1].

The integration of morphing technology into other vehicles and devices offers numerous potential advantages. Helicopters could experience reduced rotor power requirements in both hover and forward flight, leading to decreased atmospheric emissions. Additionally, blade morphing technologies could extend the flight envelope to higher forward speeds and alter the dynamic response of the rotor blades [15]. Similarly, wind turbines could benefit from rotor blade airfoil morphing, resulting in increased rotor efficiency across the entire range of operating airspeeds and allowing for the extraction of more power from the wind [16, 17].

The implementation of wing morphing mechanisms presents several challenges, as outlined by Inman [18], including various design requirements such as the amplitude of the movement, concerns regarding bindings and friction between elements, the effects of wing structural deformability under load, and the control of actuator stroke under load. Additionally, considerations such as the size, weight, and volume of actuators are crucial metrics [1], as is ensuring fail-safe behaviour. A locking mechanism is also paramount, as without it, the actuator must withstand the loads applied to the wing unless it operates in parallel with a structural element. Moreover, the speed at which the geometry change occurs is significant; while a slow speed may suffice to enhance aircraft performance during missions, a faster speed could enhance aircraft manoeuvrability.

Large shape changes concepts usually have associated design penalties such as added weight or complexity and, without these penalties, morphing would always make sense. For most applications, there is a cross-over point where energy penalties for not morphing begin to exceed the morphing weight penalty [19]. Therefore, the implementation of morphing technology in an aircraft should be considered during the design phase, considering the specific design and performance requirements of the aircraft.

The internal control and the strategy employed to alter the wings' geometry are also critical objectives, encompassing the selection of sensors, braking and locking mechanisms, and the integration of sensors with actuators through appropriate software. Moreover, changing the wings geometry entails modifications in aerodynamic loads, structural properties, inertial properties, aeroelastic behaviour, flight dynamics, and stability characteristics [12]. Consequently, ensuring a robust and efficient control system is imperative to maintain actuation stability and meet performance criteria.

1.2 Objectives

The main objective of this dissertation is to propose a novel wing morphing concept focused on the airfoil component, with potential applications in small-to-medium size

UAVs. This includes the manufacturing of a prototype to serve as proof-of-concept. To evaluate the potential aerodynamic benefits of the proposed design, a computational model is developed and analysed using structural and aerodynamic tools. Given the high computational cost of structural analysis for the concept and the need to understand how its design variables impact aerodynamic performance, a surrogate model is developed to assess key aerodynamic performance metrics. The following points outline, in detail, the sequence of objectives necessary to achieve this goal:

- Propose and present the airfoil morphing concept, detailing its functionality, materials, actuation system, and other practical characteristics, while discussing key aspects related to its implementation. The limitations of existing airfoil morphing mechanisms are analysed through a state-of-the-art review, culminating in the design of the proposed concept.
- Manufacture a prototype to demonstrate the proof-of-concept, allowing for the analysis of its practical implementation and functionalities.
- Develop a computational model of the concept to compare with experimental actuation results, assessing its precision and providing a foundation for the surrogate model.
- Create a surrogate model to evaluate the key aerodynamic coefficients of the airfoil as functions of the most critical design variables of the concept.
- Investigate the advantages and disadvantages of the proposed concept, using the prototype, the surrogate model, and various case studies, leading to the final conclusions of this work.

1.3 Dissertation Outline

This dissertation is organized into chapters, which follow a logical sequence to achieve the proposed objectives:

- **Chapter 1**, *Introduction*, provides an introduction to the “morphing” concept, outlining its characteristics, historical evolution, potential benefits of implementation, and associated challenges. These topics are discussed in a broad context, establishing the motivation for this work. The chapter also presents the objectives and the outline of the dissertation.
- **Chapter 2**, *State-of-the-Art in Airfoil Morphing*, explores the current state of research on airfoil component wing morphing. It presents conclusions from various studies regarding the practical benefits of airfoil morphing implementation,

discussing existing concepts and mechanisms along with their advantages and limitations. Additionally, the main challenges associated with airfoil morphing and the characteristics required for safe and viable real-world application are outlined.

- **Chapter 3**, *Proposed Airfoil Morphing Concept and its Evaluation Methodology*, introduces the proposed airfoil morphing concept, detailing its characteristics and the methodology for its evaluation. This includes the prototype manufacturing process and the associated experimental procedures, along with a description of the numerical model development.
- **Chapter 4**, *Surrogate Model*, provides an overview of surrogate models and describes the methodology for constructing a surrogate model to evaluate the potential aerodynamic benefits of implementing the airfoil morphing concept.
- **Chapter 5**, *Case Studies*, presents the detailed case studies conducted to further analyse and evaluate the aerodynamic performance of the airfoil morphing concept.
- **Chapter 6**, *Conclusions*, summarizes the main conclusions of this work, including an assessment of the practical viability of the morphing concept, its advantages, and limitations. It also proposes potential directions for future research and development.

Chapter 2

State-of-the-Art in Airfoil Morphing

This chapter aims to review the state-of-the-art in airfoil morphing concepts and mechanisms. It begins by outlining the key advantages that airfoil morphing technologies can offer, followed by an overview of the evolution of existing mechanisms. The chapter concludes by summarizing the main benefits and limitations of these technologies, highlighting the primary challenges involved in developing airfoil morphing systems.

2.1 Benefits of Airfoil Morphing

Airfoil morphing enables the adaptation of its geometry to specific flight conditions, thereby optimizing its performance and, consequently, enhancing the overall performance of aircraft wings. Numerous authors have delved into investigating the benefits that such morphing could bring to specific aircraft projects.

Joshi et al. [9] numerically investigated the impact of aircraft wing morphing on the performance at various flight phases of the UAV "Firebee", designed as a high-speed target UAV. The study's findings are presented in a "spider plot", depicted in *Figure 2.1*, where the outer circumference represents the optimal performance achievable by the UAV under imposed restrictions. Each axis of the plot corresponds to a performance metric associated with one of the eleven considered flight conditions. The planform morphing involves changes in the wings' geometry across its three degrees-of-freedom: wing span, chord, and sweep. Additionally, airfoil morphing incorporates changes to the wings' airfoil, selecting the most suitable airfoil for each flight condition from a set of different airfoils.

This study concluded that airfoil morphing primarily enhances the performance of this aircraft during flight phases such as cruise, loiter, turn, and take-off. While wing planform morphing has a significant overall impact on the aircraft's performance, airfoil morphing exerts a major influence during instantaneous turns. However, it's important to note that the resulting weight changes of the UAV due to the morphing mechanisms were not considered in this study.

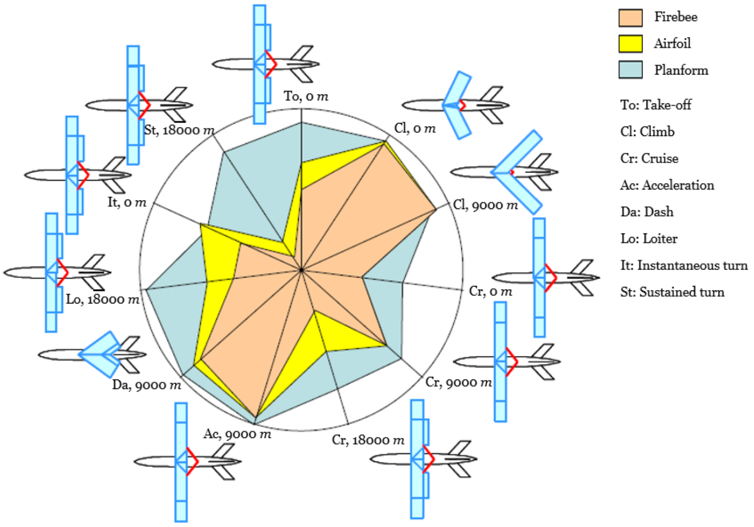

Figure 2.1 – Spider plot comparing predicted flight performance of the fixed-geometry “Firebee”, an airfoil morphing “Firebee”, and a planform morphing “Firebee”, adapted from [9].

Secanell et al. [20] numerically explored how airfoil morphing could enhance the overall performance of a specific light UAV across various flight phases by designing new airfoils tailored to each phase. The authors concluded that starting from an initial configuration of a thin airfoil, a mechanism capable of modifying the camber and leading-edge thickness of the airfoil would be almost sufficient to achieve the optimal airfoil geometry for most of the considered operational conditions. Consequently, a morphing airfoil could potentially reduce the installed power requirement, allowing the UAV greater flexibility in its operational profile, expanding its operational envelope, and sustaining manoeuvrability at low speeds. However, similar to the previous study, this research did not incorporate considerations of weight variation and mechanism selection associated with morphing.

In a Computational Fluid Dynamics (CFD) study conducted by Majid et al. [21], a comparison was made between a morphing airfoil and conventional articulated mechanisms such as plain flaps, ailerons, elevators, and rudders. The study focused on comparing the camber variation of an airfoil to an equivalent deflection of an aileron. The authors concluded that a morphing airfoil is capable of achieving up to 18.7% larger lift-to-drag ratios. Additionally, the morphing airfoil was found to attain a larger stall angle-of-attack, significantly enhancing aircraft manoeuvrability capabilities.

From the perspective of the cruise flight phase, which is predominant in the operational envelope of most aircraft, Jo et al. [22] investigated how the UAV “RQ-7a Shadow” would benefit from a morphing airfoil in its camber degree-of-freedom. The numerical study focused on increasing the camber of the original aircraft's "NACA 2410" airfoil to 4%, 6%, and 8%. While a 4% camber showed no benefits, cambers of 6% and 8% were found to increase the range and endurance of the aircraft by 17% and 60%, respectively. Indeed, it is crucial to emphasize that the original geometry of this aircraft's wings was not optimized for the cruise flight condition; instead, it represented a compromise solution necessary for the UAV to fulfil its operational objectives. This compromised initial design played a pivotal role in enabling the significant improvements realized through the hypothetical implementation of airfoil camber morphing.

In these studies, it was observed that different aircraft would derive varying degrees-of-benefit from airfoil morphing, reflecting differences in their performance requirements in different operational phases. As such, two potential paths of aircraft design are associated with these disparities, as graphically depicted by Weaver-Rosen et al. [23]. *Figure 2.2* illustrates two scenarios wherein wing morphing could enhance aircraft performance: in situation "a)", the fixed geometry of the aircraft's wings was designed to adequately fulfil all imposed design requirements to a satisfactory degree; in situation "b)", the fixed geometry of the aircraft's wings was optimized for a specific flight condition, often the cruise phase, potentially resulting in poorer aircraft performance in other flight conditions, albeit still considered satisfactory. It is important to note that only in situation "b)", where the aircraft's wing geometry is optimized for a specific flight condition, wing morphing will not necessarily improve aircraft performance in that particular flight phase. Therefore, the primary objective of wing morphing is to extend the operational envelope of an aircraft, thereby enhancing its flexibility and improving its performance across, simultaneously, various flight conditions. Consequently, the implementation of wing morphing technology necessitates careful consideration during the aircraft design phase.

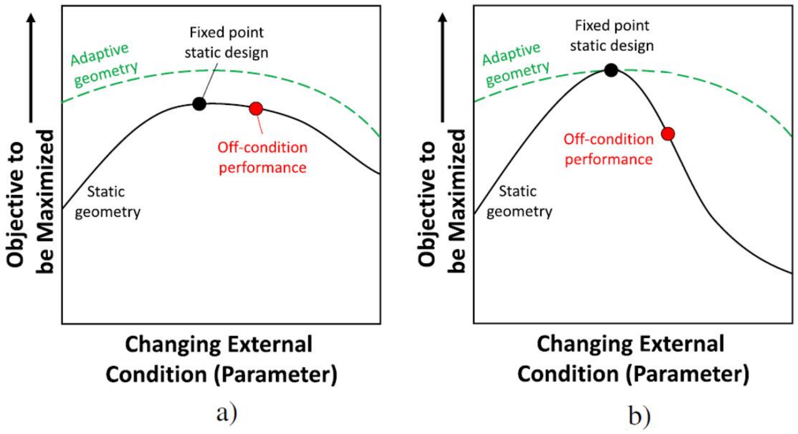

a) b)

Figure 2.2 – Aircraft performance enhancement by wing morphing: a) the fixed geometry of the aircraft wings fulfils all imposed design requirements to a satisfactory degree, b) the fixed geometry of the aircraft wings is optimized for a specific flight condition, adapted from [23].

In conclusion, a morphing airfoil offers significant improvements in aircraft performance across most flight phases within its operational envelope. This technology enables a reduction in installed power requirements and enhances flexibility in mission execution, thereby expanding the aircraft's operational envelope. In certain cases, airfoil morphing can also lead to enhancements in aircraft range and endurance or, while maintaining these parameters constant, enable a reduction in energy consumption and subsequently, the energy quantity requirements. In comparison to conventional articulated control surfaces and high-lift devices, a morphing airfoil can achieve greater lift-to-drag ratios and a higher stall angle-of-attack, thereby enhancing the manoeuvrability capabilities of an aircraft. However, these advantages hold true only up to a certain point. Beyond this threshold, the structural weight increase resulting from the use of morphing-capable mechanisms may become significant enough to deteriorate aircraft performance [19]. At this juncture, the benefits of wing airfoil morphing diminish, highlighting the importance of carefully balancing the advantages and disadvantages in aircraft design.

2.2 Evolution of Airfoil Morphing Concepts

Various concepts have been proposed for airfoil morphing in its two degrees-of-freedom: camber and/or thickness variation. Some concepts have been explored only through numerical analysis or design, while others have progressed to the experimental phase, where prototypes were manufactured and tested in wind tunnels or in-flight with full-scale models. The camber and thickness variations of an airfoil can occur in specific portions, such as near the leading-edge or trailing-edge, or in a global manner. Regarding actuators, some concepts utilize conventional actuators, including electromagnetic motors, hydraulic, pneumatic, and other actuators with movable parts; while other concepts employ solid-state smart materials, such as piezoelectric materials, Shape Memory Alloys (SMAs), and rubber muscle actuators. The actuation can also be either distributed or localized. This section presents some of the more recent concepts, discussing their advantages and limitations, with a focus on their potential application in small-to-medium size UAVs.

Smith et al. (1992) [24] proposed a mechanical mechanism actuated by an electro-hydraulic system designed to alter the camber of the airfoil near both the leading-edge and trailing-edge, intended for use on the military aircraft *F-111*. This concept features a glass-fibre composite skin and is quite complex as illustrated in *Figure 2.3*, resulting in an increased probability of failure. The mechanism was tested in flight and yielded good results, although it did experience some minor failures. While this system has the potential to enhance the lift-to-drag ratio of the airfoil at higher angles-of-attack and improve its maximum lift coefficient, it was not compared with conventional articulated mechanisms regarding the weight increase and the consequent impact on aircraft performance.

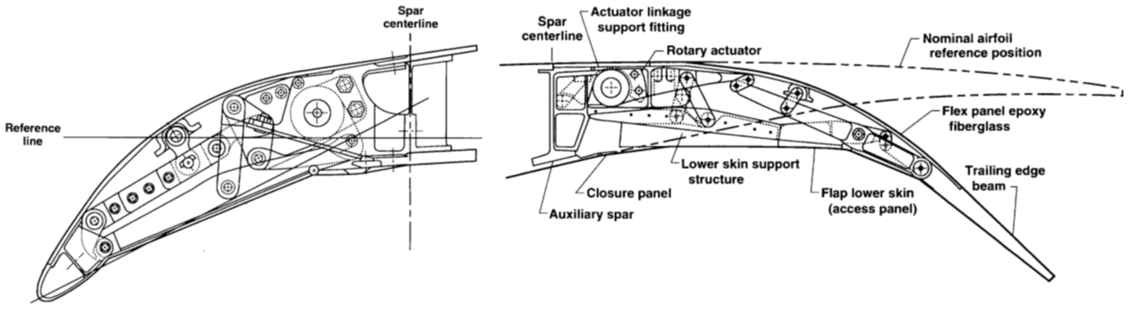

a) b)

Figure 2.3 – Airfoil morphing mechanical mechanism actuated by an electro-hydraulic system: a) leading-edge section, b) trailing-edge section; adapted from [24].

Similar concepts were proposed by Holle (1923) [25], Boeing (1973) [26], and Brissenden (1980) [27]. Although these mechanisms possess load-carrying capacity and fail-safe structural characteristics, they are inherently complex and require additional intricate systems for actuation. This complexity results in increased aircraft weight and a higher probability of failure. While such mechanisms can enhance mission flexibility in military aircraft, their implementation in civil aircraft is not yet ideal, much less for small-to-medium size UAVs.

Several authors have proposed concepts involving the variation in size of the elements of an internal rib structure or changes in the angle between these elements. Austin et al. (1994) [28] proposed the mechanism illustrated in *Figure 2.4*, capable of varying the camber and thickness of an airfoil using distributed actuators across the elements of the internal truss rib structure. Joo et al. (2009) [29] investigated on a methodology to optimally localize the actuators that enable altering the angle between structural elements. Meanwhile, Barbarino et al. (2010) [30] introduced a mechanism shown in *Figure 2.5*, where the angle variation is achieved using SMAs.

These concepts are capable of altering the camber and the thickness of an airfoil in various ways, providing significant flexibility in actuation. Moreover, the structure retains its load-carrying capability. However, the numerous distributed actuators can lead to an increase in structural weight. Additionally, these mechanisms require elastomer materials in the skin. The use of elastomer materials necessitates a pretensioned skin to withstand aerodynamic loads, presenting a major limitation due to their relatively low creep resistance. This low resistance to creep is a significant drawback for applications requiring long-term structural stability under stress [31]. Furthermore, morphing can cause the skin to experience larger strains, exacerbating the creep phenomena. An advantage of mechanisms with a large number of actuators is their fail-safe behaviour, as it ensures that even if some actuators fail, the structure remains load-carrying and controllable due to the functioning actuators.

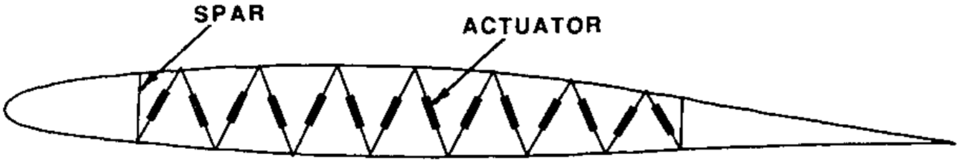

Figure 2.4 – Morphing airfoil rib truss structure with distributed actuators [28].

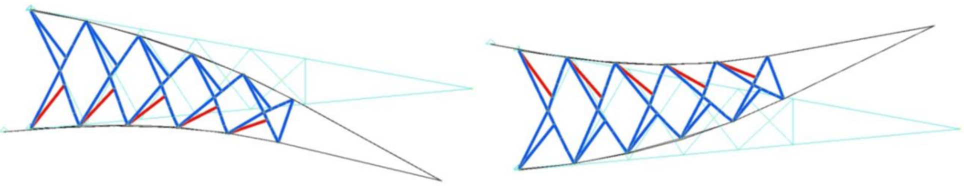

Figure 2.5 – Morphing airfoil rib structure with distributed shape memory alloy actuators (active actuators represented in red colour) [30].

Regarding the actuators, the use of SMAs presents limitations such as relatively slow actuation and the need for a system to provide heating and cooling of the alloys. Consequently, mechanisms utilizing these materials are not suitable for aircraft control but are more appropriate for adapting to the aircraft's flight condition. These mechanisms also introduce greater complexity in manufacturing. If the actuation is achieved using pneumatic or hydraulic systems, additional complications arise, as these systems require fluid accommodation and distribution, which increases fabrication complexity and control challenges, subsequently adding to the aircraft's weight.

Bartley-Cho et al. (2004) [32] proposed a variable camber trailing-edge structure design that consisted of a honeycomb centre core and elastomer outer skin, actuated by high-power ultrasonic motors using excentric motion, as presented in *Figure 2.6*. This mechanism is called "Eccentuator", was intended for implementation in a combat UAV, and was capable of a fast actuation. The structure maintained load-carrying capacity and allowed for out-of-phase actuation. However, its major limitation was the use of elastomer materials in the skin.

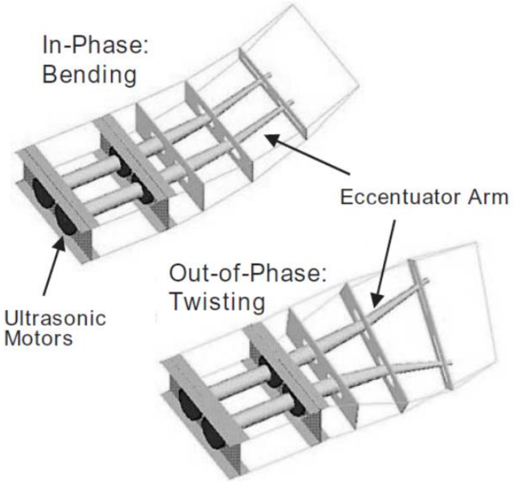

Figure 2.6 – The “Eccentuator” airfoil morphing concept [32].

Some pressure-based camber and/or thickness airfoil morphing mechanisms were proposed by Cadogan et al. (2004) [33], Vos et al. (2011) [34], and Feng et al. (2015) [35]. The first concept featured an internal adaptive inflatable bag filling the wing’s internal volume, with actuation achieved using piezoelectric actuators. The second concept employed an adaptive pressurized internal honeycomb structure, while the third concept utilized pneumatic muscle fibres forming the lower skin of the airfoil, which could change their length and, consequently, the camber of the airfoil by inflating. These concepts also require an additional system to control the pressure across various parts of the structure, increasing complexity, weight, and failure probability. Although these structures possess load-carrying capacity and offer fast actuation, they necessitate the use of elastomer skins, which have inherent limitations.

Cooper et al. (2006) [36] proposed a wing structure with wing spars that could change their longitudinal position along the airfoil chord and their inclination, thereby altering the stiffness properties of the wing structure. This approach allows aerodynamic forces to induce controlled deformation of the structure. However, this is a complex mechanism that would lead to a structural weight increase due to the necessary reinforcements required to support the loads. The structural deformation would be relatively small concerning airfoil morphing, and this mechanism also necessitates the use of an elastomer skin. Once again, this concept may not be the most suitable for application in UAVs, as it would also require additional sensors and software to predict the structure deformation according to the applied loads, thus adding complexity to the morphing control.

Mechanisms based on piezoelectric materials have been proposed by Lim et al. (2005) [37], Barrett et al. (2005) [38], Paradies et al. (2009) [39], and Bilgen et al. (2013) [40], among others. Piezoelectric materials offer relatively high and fast force output across a wide frequency bandwidth, although the strain output is relatively low. However, the weight increase with morphing implementation is considerable. For instance, the small UAV "Great Planes Edge 540" experienced almost a doubling in weight when modified to include airfoil morphing in its wings, as well as its horizontal and vertical stabilizers for control purposes [40]. Some of these mechanisms incorporate an opening in the wingbox lower part to allow the lower surface skin to enter it and enable variation in the airfoil's camber. Others utilize a slit that permits the movement, which can be covered with elastomer materials or left uncovered. This approach brings additional limitations, such as added weight for structural reinforcements and the necessity of a locking mechanism in case of actuator failure to ensure the structure can still carry loads. Moreover, if there is a gap between the skins, it will result in increased drag.

Coutu et al. (2007) [41] and Grigorie et al. (2015) [42] proposed concepts that could alter the thickness of an airfoil. These concepts are similar in terms of their working principles, as illustrated in *Figure 2.7*. These mechanisms are load-carrying capable, however, in the event of actuator failure, an additional system is required to prevent the upper skin from pulling out. These mechanisms possess the limitations already discussed, such as the use of elastomer materials in the skin, the presence of gaps between the skins, or actuation with SMAs. Another limitation is that these mechanisms can lead to a structural weight increase if the maximum thickness of the airfoil is not utilized to position the wing spar at its maximum possible height.

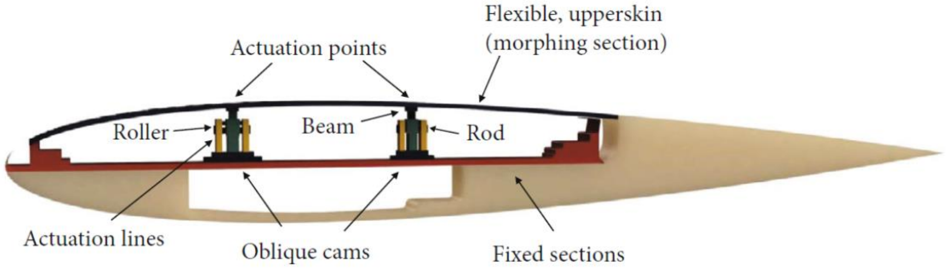

Figure 2.7 – Airfoil thickness morphing concept [7].

Developments in multi-stable composites have been made, and these were proposed for application in airfoil morphing by Diaconu et al. (2008) [43], as they offer fast actuation possibilities and load-carrying capable structures. The multi-stability is achieved by designing structures that have multiple energy strain minima. However, the manufacturing process of these composites is complex, as is the possible actuation mechanism, which results in limited morphing airfoil geometries.

Recently, notable advancements have been made in the sector of compliant mechanisms, which are defined as mechanisms designed to reach a given level of deformability by exploiting structural strain [44]. Mechanisms like these were designed by Shili et al. (2008) [45], Zhang et al. (2019) [46] – illustrated in *Figure 2.8*, and Jensen et al. (2021) [47]. The design process of a compliant mechanism typically involves a topology optimization of a wing structure where the intended actuation (force application point and direction), the initial and desired final airfoil geometries, and the loads the structure must withstand are specified. The result of this optimization is a structure capable of deforming without exceeding the specified maximum strain of the material, while simultaneously supporting the applied loads. However, these mechanisms can suffer from creep phenomena at several structural points, as the material in these areas is subjected to greater strains over extended periods. Additionally, they can experience stress concentrations, which reduce the structural life cycle and increase the probability of failure. The analysis can be combined with different materials in the internal structure, utilizing the thermal expansion of some materials (as proposed by Jensen et al. [47]), but this introduces the complexity of an additional heating and cooling system, which also slows down actuation. Additive manufacturing is emerging as a promising candidate for the manufacturing process of these mechanisms, which could be a significant advantage, providing precise control over the material properties and geometries of the compliant structures.

Figure 2.8 – Airfoil morphing compliant mechanism [46].

The “Belt-Rib” concept, described by Campanile et al. (2000) [48] and Campanile (2008) [49], and illustrated in *Figure 2.9*, is an airfoil morphing concept featuring a wing spar distribution with varying inclinations, enabling the structure to be load-carrying. However, altering the camber of the airfoil leads to the extension of either the upper or lower surface skin (depending on the direction of camber change), thus limiting the actuation to a small amplitude. Both conventional actuators and embedded smart materials were tested in this mechanism, proving its concept. Despite this, the relatively small actuation amplitude limits the versality of an aircraft's mission capabilities. Additionally, the skin experiences significant strains over long periods, leading to the creep phenomenon. Consequently, this concept might not be the most suitable for applications requiring considerable adaptability and versatility.

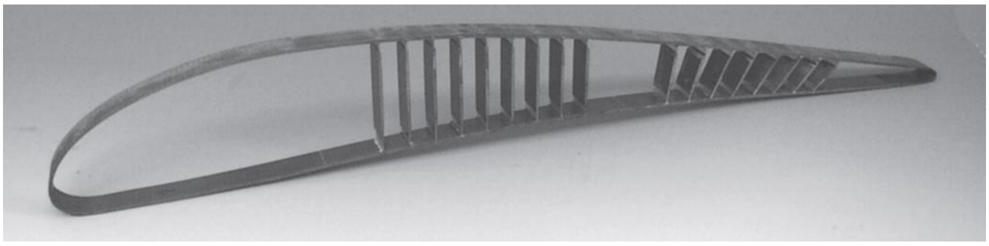

Figure 2.9 – The "Belt-Rib" airfoil morphing concept [48].

Woods et al. (2012) [50] introduced a biologically inspired "Fish Bone Active Camber" concept, which features a thin chordwise bending spine with stringers branching off like a fish's ribs. These stringers connect the spine to a pretensioned Elastomeric Matrix Composite (EMC) skin surface, maintaining the airfoil thickness by supporting the skin at a constant distance from the spine. Deflections are induced by bending moments in the spine via an antagonistic tendon drive system mounted inside the D-spar. One end of the tendon is anchored to the trailing-edge, while the other is wrapped around a spooling pulley connected to an actuator through a non-back-drivable mechanism such as a worm gear, as illustrated in *Figure 2.10*. A prototype of this concept, 3D-printed from Acrylonitrile Butadiene Styrene (ABS) plastic, was tested in a wind tunnel. Comparative experimentation with traditional trailing-edge flaps demonstrated an increased lift-to-drag ratio [51]. The non-back-drivable mechanism and the implementation of the tensioned antagonistic tendon drive system were also tested [52]. Initially, the design, analysis, and prototyping were performed using a one-dimensional model based on Euler-Bernoulli beam theory. Rivero et al. (2018) [53] further addressed the two-dimensional structural formulation for the concept based on Kirchhoff-Love plate theory, and the three-dimensional deflections using Mindlin-Reissner plate theory [54].

This concept permits the creation of a load-carrying capable structure with aerodynamic benefits and relatively large deflections. However, the limitations associated with the pretensioned elastomer skin persist. Additionally, in the event of tendon failure, the structure would be unable to support the applied loads, which compromises the overall integrity and safety of the system. Therefore, further improvements are needed to make this concept fail-safe, ensuring that it can maintain structural integrity and functionality even in the case of partial system failures.

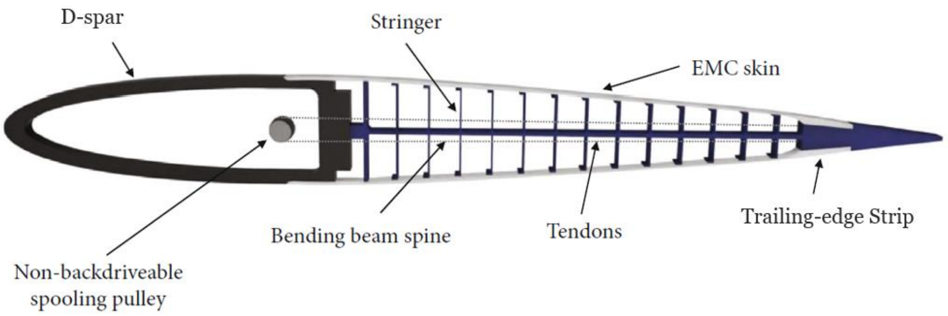

Figure 2.10 – The “Fish Bone Active Camber” airfoil morphing concept, adapted from [7].

Wu et al. (2017) [55] proposed a multiple degrees-of-freedom camber morphing concept, which allows for the generation of various morphing configurations. This concept, illustrated in *Figure 2.11*, features an internal structural layout that includes a wingbox and multiple compliant truss elements. One end of each truss element is hinged to the upper flexible skin of the trailing-edge, while the other end is driven by independently controlled compliant runners powered by an electrical actuation system – specifically, a linear ultrasonic motor. Morphing is achieved by fixing one or more runners at the lower surface of the trailing-edge and allowing the truss elements to slide along these runners through the motors. This movement bends or straightens the structure, enabling the desired morphing. The design’s morphing process, aerodynamic benefits, and load-carrying capacity were tested using carbon fibre composite airfoil prototypes and validated through computational analysis.

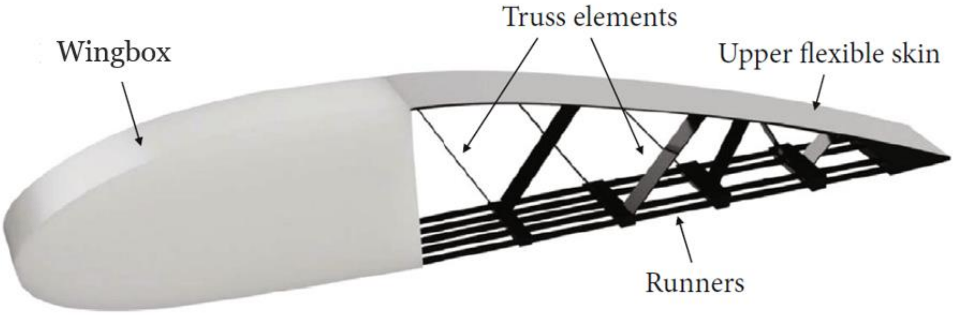

Figure 2.11 – Multiple degrees-of-freedom airfoil morphing design concept, adapted from [7].

This airfoil camber variation concept was compared with equivalent aileron deflections, and the findings indicated that this morphing mechanism could achieve greater lift-to-drag ratios, but only for lower angles-of-attack. The main advantage of this mechanism is its ability to actuate with a high number of degrees-of-freedom and to achieve significant morphing amplitudes. However, the limitation of the lower skin remains, necessitating the use of elastomer materials, which have their own set of drawbacks. Additionally, the motors in this design function as structural elements, fixing the geometry of the airfoil. This means that in the event of motor failure, the structure would lose its capacity to support the applied loads, compromising its integrity. Therefore, while the concept offers promising capabilities for morphing and improving aerodynamic performance, these limitations highlight the need for further refinement and fail-safe measures to ensure reliability and effectiveness in practical applications.

Several proposed mechanisms for airfoil morphing are based on ribs divided into parts that can rotate relative to each other. Examples of these mechanisms include those investigated by Meguid et al. (2017) [56], Zhao et al. (2019) [57] – concept illustrated in *Figure 2.12*, and Xiasheng et al. (2024) [58]. These concepts involve distributed actuation and are capable of carrying loads, making them structurally robust. However, they still require elastomer skins, which come with inherent limitations. An alternative approach involves using a non-elastomer skin, but this would introduce gaps between segments, leading to a non-continuous surface which could adversely affect aerodynamic performance by increasing drag and potentially leading to undesirable flow characteristics over the airfoil. A critical need for these mechanisms is a reliable locking mechanism to maintain structural integrity in the event of actuator failure.

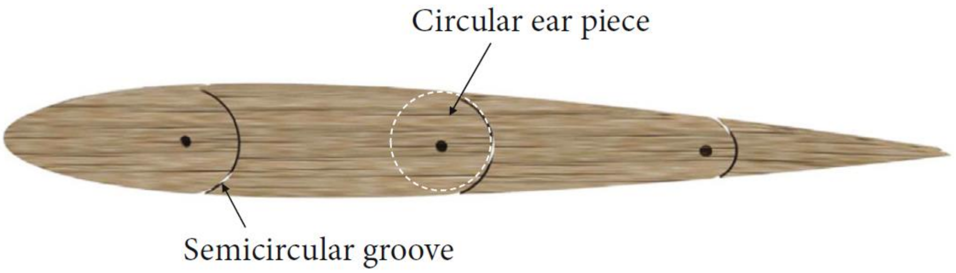

Figure 2.12 – The “Double Rib Sheet” airfoil morphing concept [7].

Other mechanisms that enable camber changes in an airfoil and are based on the concept of a gap or sliding skin were proposed by Fasel et al. (2020) [59], Moulton et al. (2021) [60] – concept showed in *Figure 2.13*, and Jia et al. (2022) [61]. Some mechanisms involve having the gap filled with a V-shaped elastomer material. However, this introduces the previously discussed limitations associated with using elastomers. The considerable advantages of these concepts are the simplicity and fast actuation using servomotors, which makes them attractive for certain applications.

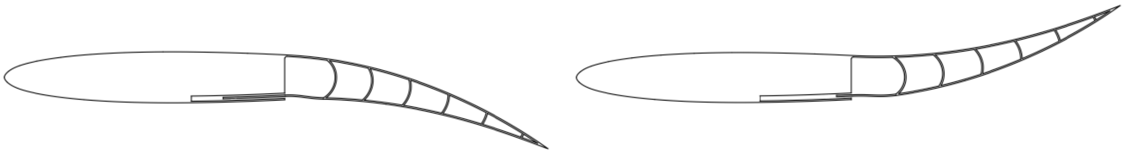

Figure 2.13 – Sliding lower surface skin airfoil morphing concept [60].

In this section were reviewed the main advantages and limitations of various proposed concepts for airfoil morphing. Mechanisms using elastomer materials allow for the extension and retraction of the skin, facilitating variations in airfoil camber and thickness; however, these designs require pretensioned skins to resist aerodynamic loads, which leads to the creep phenomenon and necessitates the consequent frequent skin replacements. Some morphing mechanisms use gaps or sliding skins to permit structural deformation; while these designs enable morphing, they can cause boundary layer separation and increase drag. Additionally, they require fail-safe locking systems in case of actuator failure, which adds complexity and weight. Other concepts involve additional actuation systems, which provide precise control over morphing mechanisms; however, these systems increase the aircraft's weight and complexity, raising the probability of failure and limiting their practical applications.

Piezoelectric materials offer high and fast force output over a wide frequency range, making them suitable for micro UAVs; despite this, their low strain output and the significant weight increase present challenges that need to be addressed. SMAs are advantageous for adapting an airfoil to different flight conditions but require additional heating and cooling systems and exhibit relatively slow actuation speeds. These characteristics make them unsuitable for real-time aircraft control. Compliant mechanisms have emerged as a promising technology, allowing for controlled and localized actuation to achieve the desired airfoil geometries. However, the internal structures of these mechanisms can suffer from high strains during long periods, which leads to creep, and stress concentrations that may reduce the structural lifespan.

In summary, while each airfoil morphing concept offers unique advantages, they also come with specific limitations impacting their practical application. Future developments must address these limitations to enhance the feasibility and efficiency of airfoil morphing technologies.

2.3 Challenges in Airfoil Morphing Implementation

In the previous section were reviewed the advantages and limitations associated with current airfoil morphing mechanisms. These mechanisms bring various challenges to their implementation, which have been investigated by several authors. In this section, these challenges will be discussed in detail.

As described by Wagg et al. [44], conciliating the conflicting requirements of deformability, load-carrying capability, and low weight is the predominant issue in the mechanical design of shape-adaptable systems. While established technologies and disciplines can successfully meet any two of these three requirements, achieving all there simultaneously presents a significant challenge. *Figure 2.14* illustrates the relationship between these three disciplines: lightweight structures, conventional mechanisms, and compliant mechanisms.

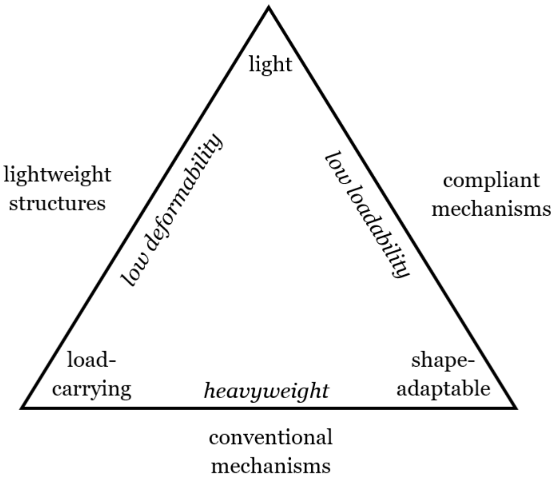

Figure 2.14 – Triangle of requirements for lightweight shape adaptation in morphing wing design [44].

The first discipline is lightweight design, encompassing a wide range of procedures, criteria, and techniques for analysing and synthesizing structures with high strength-to-weight ratio. Lightweight structures, however, typically exhibit a low degree-of-deformability. This is a direct consequence of the fundamental principle of lightweight design, which aims to achieve a stress state predominantly characterized by skin loading, while avoiding bending and torsion loading of individual components. The second discipline, which successfully combines two of the three aforementioned requirements, is the science of conventional mechanisms. These mechanisms are highly deformable and capable of carrying substantial loads, but they are far from being optimized for lightweight applications. Lastly, the third discipline addresses the remaining pair of requirements: the science of compliant mechanisms. Compliant mechanisms offer an excellent combination of deformability and low weight, but they are currently limited in their load-carrying capability. Systems with lumped compliance, featuring cut-outs or other forms of solid-state hinges, typically suffer from stress concentration effects in the compliant regions. In contrast, systems with distributed compliance are more challenging to control due to their low stiffness across numerous degrees-of-freedom.

In regard to skins, Thill et al. [4] noted that elastomer and anisotropic materials hold promise for this application. However, elastomers possess relatively low Young's modulus values (ranging from 0.5 to $50\ MPa$ [4]), meaning they require low actuation forces but are ill-suited to withstand aerodynamic loads. Kikuta [62] conducted experimental tests on various commercially available thermoplastic polyurethanes, copolyesters, and woven materials. The characteristics of these materials were examined, and their suitability for application in morphing aircraft wing skins was assessed. Initially, the author defined the properties that these skins should exhibit: high out-of-plane stiffness to endure aerodynamic loads, low in-plane stiffness to minimize actuation forces, toughness and resistance to abrasion and chemicals, resilience to different weather conditions, high strain capability and recovery rate, and fatigue resistance. Unfortunately, none of the selected materials met all these requirements simultaneously.

In conclusion, we can summarize the main challenges in implementing airfoil morphing mechanisms in small-to-medium size UAVs by deducting the necessary characteristics such mechanisms should possess:

- **Fail-safe structure**: the structure should maintain its integrity and be able to withstand aerodynamic loads in the event of an actuator failure.
- **Integrated actuators**: actuators should ideally be integrated as structural elements to minimize weight, without compromising the fail-safe behaviour.
- **Optimized actuator quantity**: the number of actuators should be minimized to reduce weight, while ensuring there are enough to achieve a wide range of airfoil morphing degrees-of-freedom and movement amplitudes.
- **Fast actuation**: the actuation speed must be sufficient to allow for aircraft control as well as adaptability to flight conditions, potentially eliminating the need for a separate conventional control system and thus reducing weight.
- **Avoid secondary systems**: secondary systems for morphing should be avoided as they add weight, complexity, and increase the probability of failure.

- **Skin material**: elastomer materials should be avoided, as a pretensioned skin configuration induces the creep phenomenon and reduces its lifespan.
- **Avoid sliding skins**: avoiding sliding skins can decrease structural weight and ensure the structure’s integrity even if the locking mechanism fails.
- **Long service life of the structure**: structural elements should not be subjected to high strains to minimize creep phenomena, and stress concentrations should be avoided to extend the structure’s lifespan.
- **Continuous skin surface**: the skin should remain continuous and free of edges and gaps to reduce unwanted aerodynamic phenomena, such as boundary layer separation, which increases drag.

These characteristics will guide the design and implementation of the airfoil morphing concept proposed and discussed in *Chapter 3*.

Chapter 3

Proposed Airfoil Morphing Concept and its Evaluation Methodology

This chapter aims to propose the airfoil morphing concept, detailing its characteristics and potential operational advantages. It outlines the methodology employed to evaluate the feasibility of its practical implementation, along with the results derived from this approach.

3.1 Airfoil Morphing Concept

The proposed airfoil morphing concept, designed for application in small-to-medium size UAVs and aimed at addressing some of the limitations of existing mechanisms reviewed in *Chapter 2*, is presented in *Figure 3.1*.

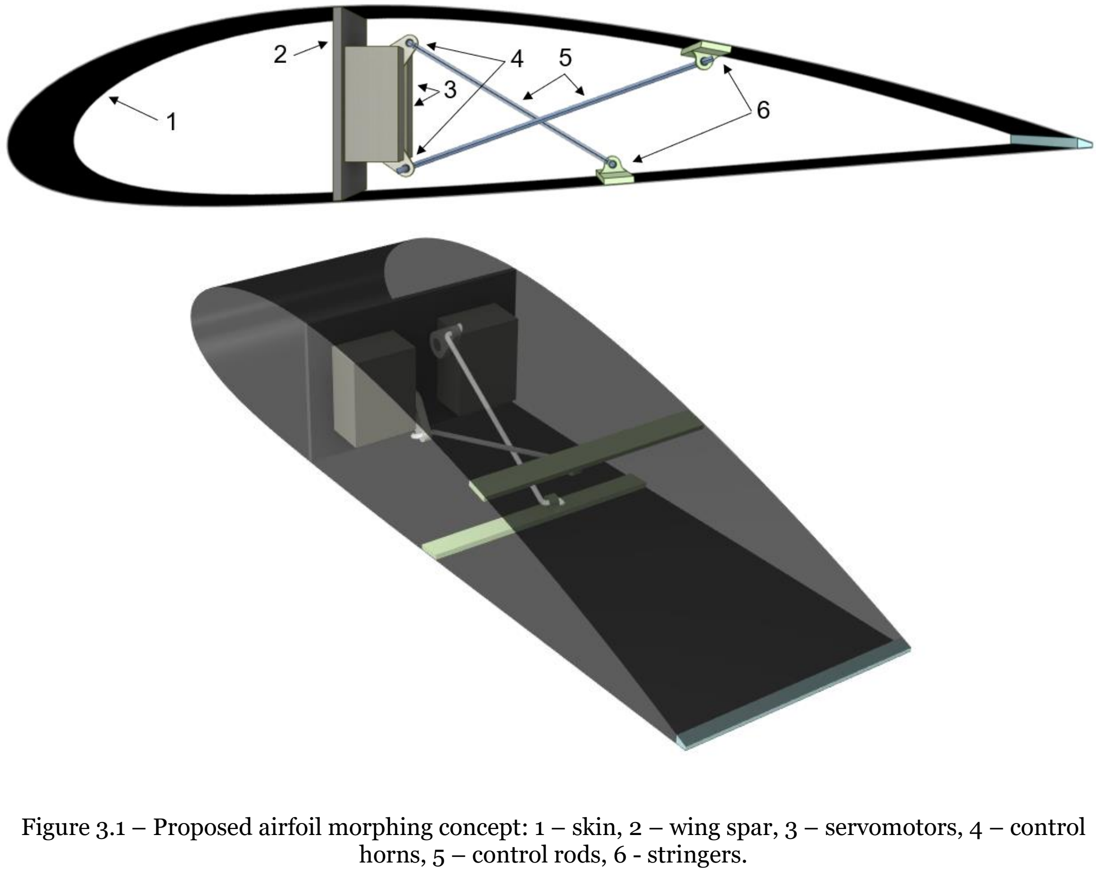

Figure 3.1 – Proposed airfoil morphing concept: 1 – skin, 2 – wing spar, 3 – servomotors, 4 – control horns, 5 – control rods, 6 - stringers.

The mechanism is composed of a fixed geometry portion of the wing – formed by the wing spar and the skin that extends from it to the leading-edge – assembling the wingbox, and a morphing extension comprising the skin extending from the wing spar to the trailing-edge. Both the morphing upper and lower surfaces of the wing are actuated by two servomotors fixed to the wing spar. These servomotors connect to the skins through hinged control rods at both ends and stringers, converting the rotational movement of the control horns into translational movement of the stringers and, consequently, of the stringers to skins connection surfaces. The trailing-edge allows for relative variation of the slopes of the upper and lower airfoil surfaces at the trailing-edge point. In this way, this concept enables the alteration of the camber and the thickness from the wing spar to the trailing-edge of the airfoil.

In this concept, the positions along the wing's chord of the wing spar and of the stringers, as well as the thicknesses of the upper and lower surfaces skins, can vary. Different types of actuators could also be employed – linear actuators, for instance, would be a suitable option. Using two actuators allows for either separate or coordinated actuation of both surfaces. The position of the wing spar along the chord will determine the morphing extension of the airfoil and the dimensions of the wingbox; the positions of the stringers will define the possible airfoil geometries achieved through morphing; and the thicknesses of the skins will determine the structure's capability to support aerodynamic loads, as well as the force or energy required for actuation. The thickness of the lower surface skin relative to the thickness of the upper surface skin could primarily influence the geometry of the upper surface during its isolated actuation.

Therefore, the concept becomes versatile in accordance with the structural and aerodynamic characteristics desired for the wing, allowing for a significant variation of the discussed parameters. It is thus designed with a large number of degrees-of-freedom. Furthermore, if more than one pair of actuators is implemented along the semi-span of a wing, the concept could enable out-of-phase actuation, facilitating variation in airfoil geometry along the wing.

This concept effectively addresses the challenges posed for an airfoil morphing mechanism. It features a fail-safe structure, ensuring that even in the event of actuator failure, the skin can still withstand aerodynamic loads. The actuators, along with the control rods, serve as structural elements, integrating the actuation system into the wing's structure and thereby reducing its weight. Actuation is rapid and enables significant airfoil morphing amplitudes. The concept allows for control akin to plain flaps and ailerons, providing not just aircraft adaptation to flight conditions but also its control, eliminating the need for an additional control system. It operates without requiring additional systems beyond the electrical system typically found in every UAV. The wing surface is continuous, without gaps, also ensuring continuous surface curvature and minimizing the risk of boundary layer separation. Importantly, no structural member is subjected to significant strains that could lead to creep phenomena and limit the structural lifespan.

Implementing this morphing concept in a UAV offers several operational advantages. The actuation system, as long as there is a precise control of the displacement or rotation of the actuators, ensures high accuracy in achieving the desired airfoil geometry. Additionally, the wing structure can be easily repaired if any component fails, and as no unconventional systems are employed, the integration of this concept in a UAV is simplified.

Regarding the design of a wing utilizing the presented morphing concept, several key considerations must be addressed. The thickness design of the upper and lower surface skins must be integrated with the number of actuator pairs used in the wing. This is to ensure a fail-safe behaviour where the skin can withstand aerodynamic loads even if an actuator fails. The position of the wing spar along the chord defines both the dimension of the wingbox and the morphing extension of the airfoil. This creates a necessary compromise between structural weight and aerodynamic benefits. Moreover, the selection of actuators based on their force (or torque) output capacity will impact the skin thickness design. Actuators with integrated locking mechanisms, which prevent any movement when inactive, offer advantages as they require no energy to maintain the current airfoil geometry. This design approach aims to balance the structural and aerodynamic needs while ensuring the system's reliability and efficiency.

The concept envisions the use of composite materials for the skin to obtain a lighter wing structure, with thickness carefully limited to prevent exceeding the maximum strain limit when subjected to bending during morphing. The thickness is also limited to avoid the need for considered large actuation forces.

However, the concept requires a compliant trailing-edge that joins both upper and lower surface skins, allowing for their relative slope variation at that point. This can be achieved by using a hinged joint between the skins or elastomer materials. A hinged joint might generate additional drag if it is large but could be a viable solution if kept relatively small. On the other hand, using elastomers could be advantageous: as a thin layer with a small width, the strains from morphing would not be excessively high, minimizing the impact of the creep phenomenon. Additionally, replacing the elastomer would be straightforward, and the amount needed for each repair would be relatively minimal.

Finally, it is important to note that for a given wing chord dimension, airfoils with a lower relative maximum thickness would face limitations in terms of the dimensions of the actuators to be implemented and the achievable morphing amplitudes. This is due to the reduced distance between the upper and lower surface skins, which restricts the relative displacement of the stringers and consequently limits the morphing potential.

3.2 Methodology

The evaluation methodology of the proposed airfoil morphing concept comprises two main components: a physical prototype and its numerical model. The prototype involves both its manufacturing and the mechanical characterization of the materials used, with the obtained properties serving as inputs for the numerical model. The numerical model itself is divided into two types: a detailed model that closely represents the manufactured prototype and a simplified model. The detailed model is actuated similarly to the physical prototype, and the results from both are compared to evaluate the accuracy of the numerical model and the quality of the prototype's manufacturing. The simplified numerical model is used to develop a surrogate model, which identifies the key design variables and their impact on the aerodynamic performance of the morphing airfoils. The conclusions drawn from these components will assess the practical viability, potential applications, and advantages and limitations of the proposed wing morphing concept.

In addition to this methodology, case studies are incorporated to provide a more detailed analysis of the potential aerodynamic benefits of the morphing concept. These studies also compare the performance of the proposed concept with conventional hinged surfaces (CHSs), such as ailerons or plain flaps.

This methodology necessitates both structural and aerodynamic analyses of the proposed morphing concept. For structural analysis, the Finite Element Method (FEM) is an appropriate choice, as it allows for the efficient simulation of both linear and nonlinear deformations in complex structures. FEM works by discretizing the structure into smaller elements connected at their nodes and along hypothetical interelement boundaries [63], applying the necessary boundary conditions. For the computational FEM analysis, the software selected is *Ansys* [64].

For the aerodynamic analysis, the aim is to evaluate the key aerodynamic coefficients of the airfoil geometries resulting from morphing. *XFOIL* [65] is identified as a suitable software for this purpose, that uses a higher-order panel method to compute the pressure distribution around the airfoil [66]. This tool is advantageous for this work as it provides a more straightforward and computational cost-efficient analysis compared to CFD simulations, also facilitating rapid evaluations of CHSs.

Figure 3.2 presents a block diagram that summarizes the overall methodology applied in this work.

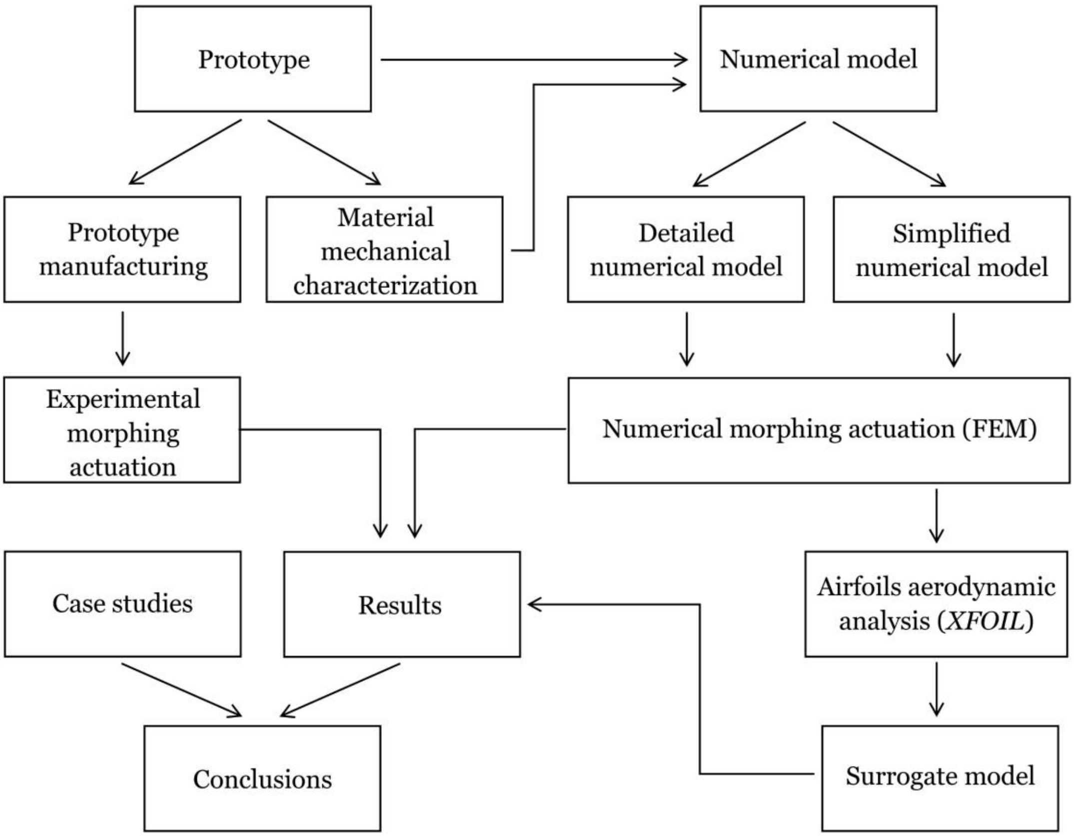

Figure 3.2 – Block diagram of the overall methodology.

3.3 Prototype

3.3.1 Prototype Manufacturing

The presented airfoil morphing concept is implemented in a wing panel with the characteristics listed in *Table 3.1*, where the placement of its components is provided as a percentage of the wing panel's chord length.

Table 3.1 – Wing panel characteristics.

Wing panel span	$200.0\ mm$
Wing panel chord	$250.0\ mm$
Airfoil	"NACA 4418"
Wing spar placement	$30.0\ \%$
Upper surface stringer placement	$65.0\ \%$
Lower surface stringer placement	$55.0\ \%$
Upper surface skin thickness	$0.45\ mm$
Lower surface skin thickness	$0.30\ mm$

The characteristics of the wing panel represent the design degrees-of-freedom for the proposed airfoil morphing concept and are chosen to facilitate the mechanism's implementation and testing. The "NACA 4418" airfoil, with a maximum relative thickness of 18.0%, provides several advantages. Its increased thickness allows for a greater distance between the upper and lower surface skins, simplifying the integration of the actuation system and enabling a clearer visualization of its operation. Additionally, this design enables larger skin displacements during actuation, making it feasible to compare experimental results with numerical ones. The maximum thickness of this airfoil occurs at 30.0% of the chord, which is also the chosen location for the wing spar. For a chord length of $250\ mm$, this placement corresponds to a spar height of $45\ mm$.

The placement of the stringers is strategically selected to ensure that the displacements achieved in the wing panel skins are relatively significant. To avoid the reduced airfoil thickness near the trailing-edge and the structural limitations near the wing spar, the upper and lower surface stringers are positioned at 65.0% and 55.0% of the chord, respectively. These positions strike a balance between maximizing displacement and maintaining structural feasibility.

The thicknesses of the upper and lower surface skins are determined by analysing the pressure distribution around the airfoil, extrapolated to a small wing panel. This analysis does not account for the loads applied to a full-scale wing on an actual UAV but aims to approximate realistic thickness values for practical application. Two key requirements are enforced: avoiding maximum stress in the skin and ensuring a fail-safe condition with a maximum displacement of $1.0\ mm$ $(0.4\%$ of the chord) at any point on the skins in the absence of actuators. These requirements are evaluated under various operational conditions (angles-of-attack), with Reynolds numbers ranging from 250×10^3 to

1×10^6. An iterative process is conducted to identify the minimum possible thickness values that satisfy both criteria.

Applying the aerodynamic load uniformly along the span of the wing panel enables the use of a unidirectional Carbon Fibre Reinforced Polymer (CFRP) skin with fibres aligned along the chord. This approach minimizes the required skin thickness, resulting in values of $0.45\ mm$ and $0.30\ mm$ for the upper and lower surfaces, respectively.

The process of manufacturing the prototype, including its materials, is described as follows:

1) Two Polylactic Acid (PLA) moulds are 3D-printed – one containing the geometry of the upper surface and the other of the lower surface of the wing panel.
2) The moulds are polished, and a thin layer of varnish is applied and polished to achieve a smooth finish.
3) A thin layer of mould release agent, Polyvinyl Alcohol (PVA), is applied on the moulds before lamination.
4) The upper and lower surface skins are laminated separately using unidirectional carbon fibre with a weight of $100\ g/m^2$ and epoxy resin “L” with “W300” hardener (*Faserverbundwerkstoffe*), achieving a fibre volume fraction of $60.0\ \%$, with the fibres oriented along the chord.
5) The CFRP cure is conducted in a vacuum bag at room temperature.
6) A $4\ mm$ thick plywood wing spar, with embedded servomotors (fitted with control horns), and 3D-printed PLA stringers with unidirectional CFRP caps are bonded to the skins using epoxy glue.
7) Control rods made of $0.8\ mm$ diameter steel beams are assembled.
8) Both skins are joined at the leading-edge using three layers of CFRP and at the trailing-edge with a thin $4\ mm$ wide layer of “CS25” condensation cure silicone rubber (*Easy Composites*). Due to poor adhesion between silicone rubber and CFRP [67, 68], a film of silicone glue (*Boost*) is applied to enhance the bond between the two materials.

Figures 3.3 and *3.4* display the 3D-printed wing panel moulds and the manufactured wing panel, respectively.

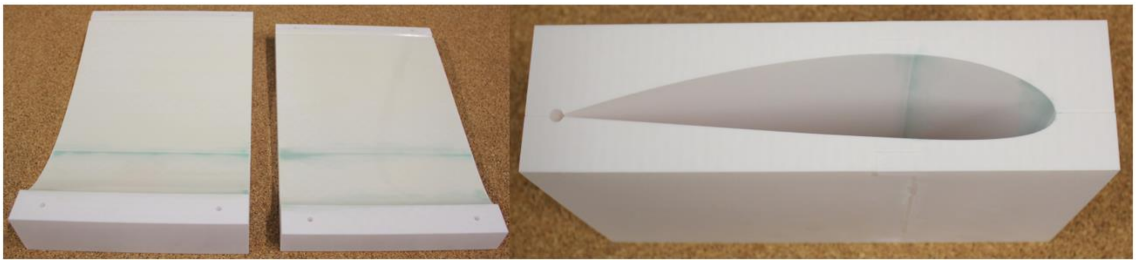

Figure 3.3 – 3D-printed wing panel moulds.

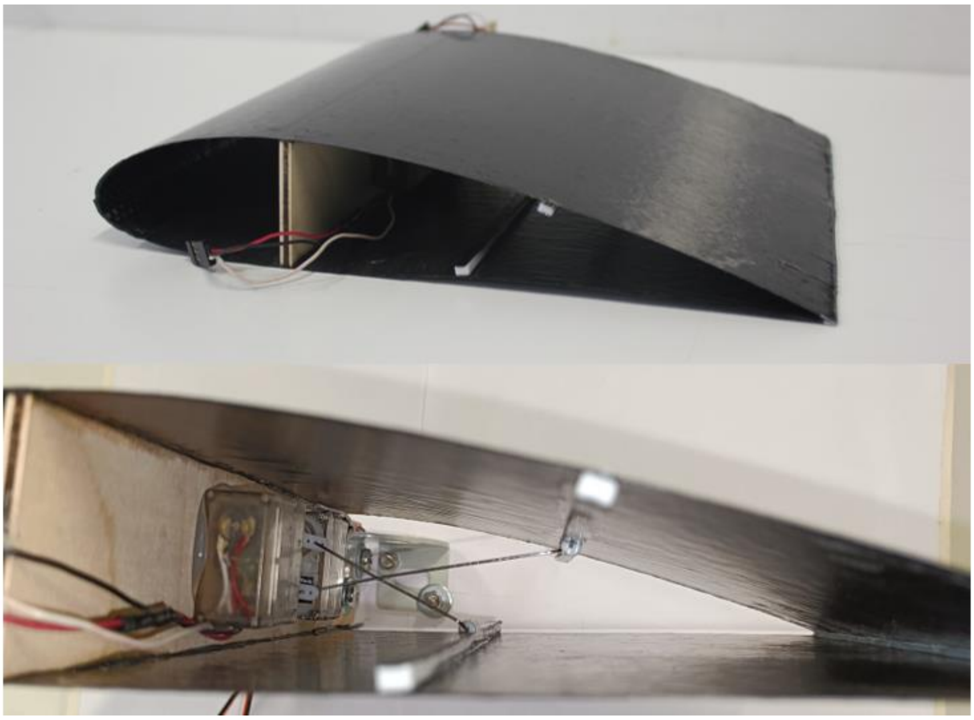

Figure 3.4 – Manufactured wing panel with the morphing mechanism.

3.3.2 Material Mechanical Characterization

The mechanical characterization of the material used for the wing panel skin – a unidirectional CFRP composite – is conducted through experimental tests on specimens to determine the material's flexural and tensile properties (specifically the modulus of elasticity and strength), in accordance with *ASTM D 790* [69] and *ASTM D 3039* [70] standards, respectively.

The process of obtaining the specimens involves manufacturing and cutting a CFRP plate using the same fibre and resin volume proportion as in the prototype. The curing process is performed in a vacuum bag at room temperature to ensure consistency with the conditions used for the wing panel skin.

Both the flexural and tensile tests are conducted using the “Shimadzu” universal testing machine, equipped with a $50\ kN$ load cell. For the flexural test, following the *ASTM D 790* [69] standard recommendations, a support span-to-depth ratio of $40{:}\,1$ is used due to the highly anisotropic nature of the material caused by the unidirectional fibre orientation. For the tensile test, aluminium tabs are assembled to the specimens. Five specimens are tested for both flexural and tensile tests. *Table 3.2* summarizes the mean dimensions of the specimens and each test characteristics. *Figure 3.5* shows images of the tensile and flexural tests setups.

Table 3.2 – Tensile and flexural tests characteristics and specimens mean dimensions.

		Tensile test	**Flexural test**
Mean specimen width	mm	14.80	14.79
Mean specimen thickness	mm	2.00	2.00
Displacement rate	mm/min	2.00	
Mean distance between tabs	mm	177.0	–
Span length	mm	–	80.0

Figure 3.5 – Experimental setup of the tensile (on the left) and flexural (on the right) tests.

The tensile test provides the load carried by the test specimen, P_t, and the corresponding extensional displacement, d_t. The specimen cross-sectional area, A_t, is calculated at three equally spaced cross-sections using the specimen’s width, b_t, and thickness, t_t, measured at these points, following *Equation 3.01*. The tensile stress, σ_t, is then computed with the specimen minimum cross-sectional area, $A_{t,min}$ (selected as the smallest cross-sectional area from the three sections), as shown in *Equation 3.02*. The tensile strain is calculated based on the specimen length, L_t, as indicated in *Equation 3.03*.

$$A_t = b_t t_t \qquad (3.01)$$

$$\sigma_t = \frac{P_t}{A_{t,min}} \qquad (3.02)$$

$$\varepsilon_t = \frac{d_t}{L_t} \qquad (3.03)$$

The flexural test provides the transversal load supported by the specimen, P_f, and the corresponding specimen midspan deflection, d_f. The flexural stress, σ_f, is computed using the support span, L_f (with a value of 80.0 mm), the specimen width, b_f, and the specimen thickness, t_f, as shown in *Equation 3.04*. The flexural strain, ε_f, is calculated using *Equation 3.05*.

$$\sigma_f = \frac{3P_f L_f}{2b_f t_f^2} \qquad (3.04)$$

$$\varepsilon_f = \frac{6d_f t_f}{L_f^2} \qquad (3.05)$$

The tensile modulus of elasticity, E_t, and the flexural modulus of elasticity, E_f, are obtained using the chord modulus, which corresponds to the slope of the linear portion of the stress-strain curve from both tests and each specimen, and are calculated using two points of this linear portion, 1 and 2, following *Equations 3.06* and *3.07*, respectively.

$$E_t = \frac{\sigma_{t,2} - \sigma_{t,1}}{\varepsilon_{t,2} - \varepsilon_{t,1}} \qquad (3.06)$$

$$E_f = \frac{\sigma_{f,2} - \sigma_{f,1}}{\varepsilon_{f,2} - \varepsilon_{f,1}} \qquad (3.07)$$

The tensile and flexural strengths, $\sigma_{t,ult}$ and $\sigma_{f,ult}$, respectively, are determined from the maximum stresses supported by each specimen during the tests. For both tests, the material properties – modulus of elasticity and strength – are obtained by averaging the values from each specimen, with the corresponded standard deviation also reported. The mean of some property Z, denoted as $\bar{Z}$, is calculated using *Equation 3.08*, and the standard deviation, SD_Z, is calculated using *Equation 3.09*.

$$\bar{Z} = \frac{\sum_{i=1}^{n_s} Z_i}{n_s}, i = 1, n_s \qquad (3.08)$$

$$SD_Z = \sqrt{\frac{\sum_{i=1}^{n_s} Z_i^2 - n_s \bar{Z}^2}{n_s - 1}}, i = 1, n_s \qquad (3.09)$$

where n_s is the number of test specimens, $n_s = 5$.

Table 3.3 presents the results of the tensile and flexural tests, highlighting the mechanical properties of the CFRP material, specifically the modulus of elasticity and strength, for both tests. These values include the mean and standard deviation for each property.

Table 3.3 – Experimentally obtained carbon fibre reinforced polymer mechanical properties.

	Property		**Value**
Tensile test	Tensile modulus	GPa	37.0 (±1.2)
	Tensile strength	MPa	671.7 (±35.0)
Flexural test	Flexural modulus	GPa	48.9 (±3.6)
	Flexural strength	MPa	388.1 (±31.9)

The obtained CFRP mechanical properties exhibit standard deviation values below 10%, reflecting high quality in both specimen fabrication and test execution. Finally, Soares [68] experimentally obtained the mechanical properties of the silicone rubber used in the prototype, specifically its modulus of elasticity and Poisson's ratio. These properties were combined with those provided by the silicone rubber manufacturer [71], and are presented in *Table 3.4*.

Table 3.4 – Silicone rubber mechanical properties.

Property		**Value**	**Reference**
Modulus of elasticity	MPa	0.505	[68]
Poisson's ratio	–	0.35	
Tensile strength	MPa	4.0	[71]
Elongation at break	%	525.0	

3.3.3 Servomotors Calibration

The process of servomotors calibration is necessary to determine its output torques. For a constant input voltage value, the torque, T, is directly proportional to the input current, I, by the motor torque constant, k_T, as given by *Equation 3.10* [72].

$$T = k_T I \qquad (3.10)$$

The experimental setup is shown in *Figure 3.6*, where the servomotor is securely mounted using two perpendicular surfaces, allowing its control horn to support a specified weight. A multimeter is connected to the battery-servomotor circuit to measure the current supplied to the servomotor.

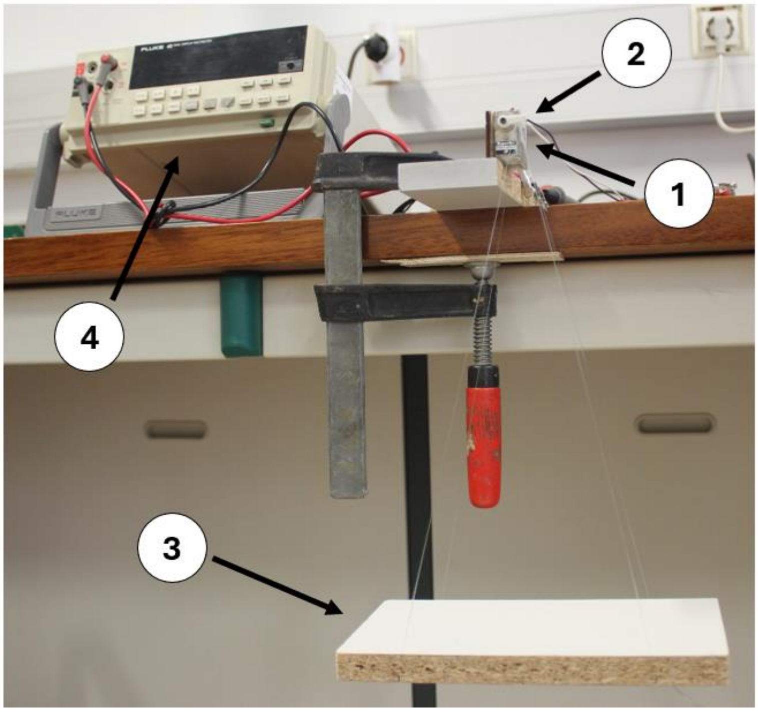

Figure 3.6 – Servomotors calibration setup: 1 – servomotor, 2 – control horn, 3 – weight support, 4 - multimeter.

The experimental procedure involves placing a mass on the weight support and actuating the servomotor until its control horn reaches and maintains a horizontal position. At this point, the input current value is recorded using the multimeter. The test is conducted with various mass values, and the resulting output torque of the servomotor, T_{out}, is calculated by multiplying the supported weight, W_{supp}, by the length of the control horn (the distance between its rotational centre and the weight suspension point), l_{CH}, as shown in *Equation 3.11*.

$$T_{out} = W_{supp} l_{CH} \quad (3.11)$$

The tests are conducted using two servomotors, and for each supported weight value, three input current measurements are taken. The output torque is subsequently plotted as a function of the average input current value and a linear regression is performed on this data to determine the equation that relates the output torque to the input current.

Figure 3.7 presents the output torque of the servomotors – one designated for actuating the upper surface skin of the wing panel ("Servomotor US") and the other for the lower surface skin ("Servomotor LS") – plotted against the input current, with an input voltage of 6.64 V. Linear regression applied to both datasets results in *Equations 3.12* and *3.13*, which define the output torque of the "Servomotor US" and "Servomotor LS", T_{US} and T_{LS}, respectively, as functions of their corresponding input current values, I_{US} and I_{LS}.

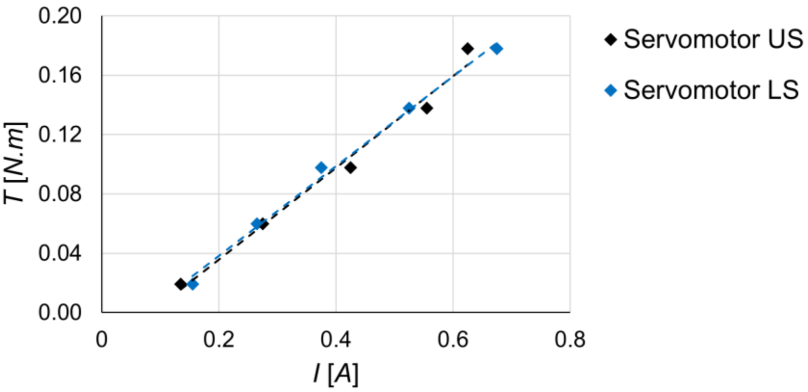

Figure 3.7 – Servomotors output torque as a function of the input current.

$$T_{US} = 0.309 I_{US} - 0.026 \quad (3.12)$$

$$T_{LS} = 0.302 I_{LS} - 0.022 \quad (3.13)$$

These results show that the slopes of the output torque versus input current curves for both servomotors are very similar, confirming proper performance, as the servomotors used are of the same model. However, there is a non-zero y-intercept, which derivates from the theoretical expectation. This can be attributed to effects at low input current values, such as internal friction, the servomotors' efficiency (less than 100%), or measurement errors and noise. Nevertheless, the y-intercept values remain relatively slow.

3.3.4 Prototype Testing

The wing panel is tested using the experimental setup depicted in *Figure 3.8*. The wing panel spar if fixed in place and a remote control, along with its receiver, is employed to actuate the two servomotors – one for actuating the upper surface skin and the other for the lower surface skin. Two multimeters are utilized to measure the input current of each servomotor, allowing for the determination of the output torque when the servomotors' control horns are in a stable position.

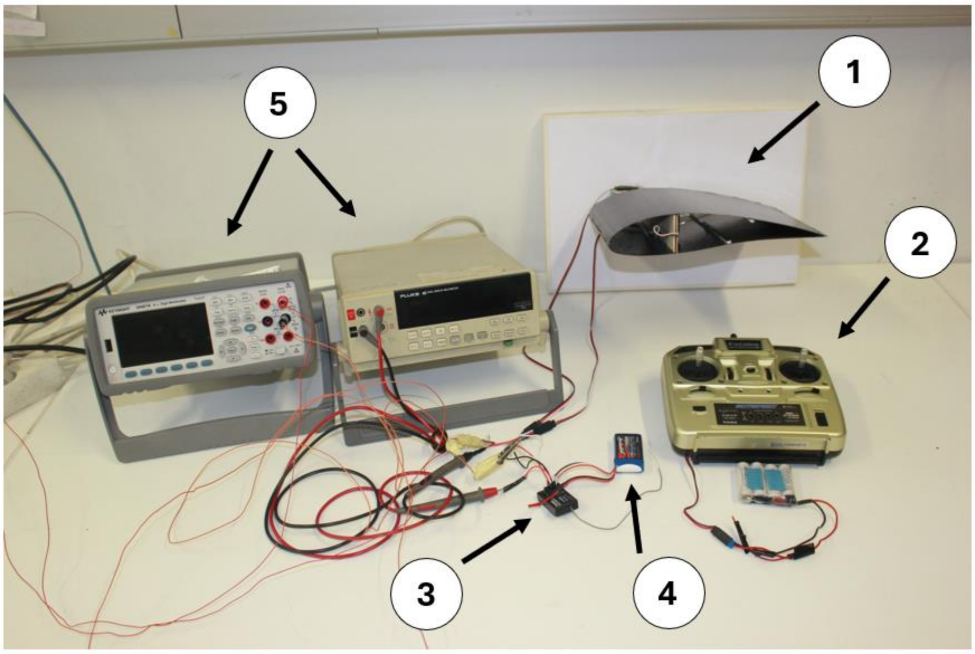

Figure 3.8 – Prototype testing setup: 1 – wing panel, 2 – remote control, 3 – receiver, 4 – battery, 5 - multimeters.

Five actuation cases are conducted to compare the experimentally obtained structural displacements with those obtained numerically. The geometry of the morphing airfoils is captured through image processing, with photographs taken from a lateral viewpoint of the wing panel during actuation. It is important to note that when only one skin is actuated, the control horn of the other servomotor remains stationary due to the locking mechanism present in the servomotors used.

These five cases of wing panel actuation are detailed in *Table 3.5*, where the actuation torques are computed using *Equations 3.12* and *3.13*, based on the experimentally measured input current values. *Figure 3.9* shows images of the actuated wing panel for each of these cases.

Table 3.5 – Wing panel experimental actuation input current and output torque values.

	Upper Surface		**Lower Surface**	
Case	$I_{US}\ [A]$	$T_{US}\ [N \cdot m]$	$I_{LS}\ [A]$	$T_{LS}\ [N \cdot m]$
1	0.000	0.000*	0.350	0.084
2	0.000	0.000*	0.815	0.224
3	0.960	0.271	0.185	0.034
4	0.780	0.215	0.305	0.070
5	0.795	0.220	0.725	0.197

* The servomotor was not actuated, thus *Equation 3.12* does not apply.

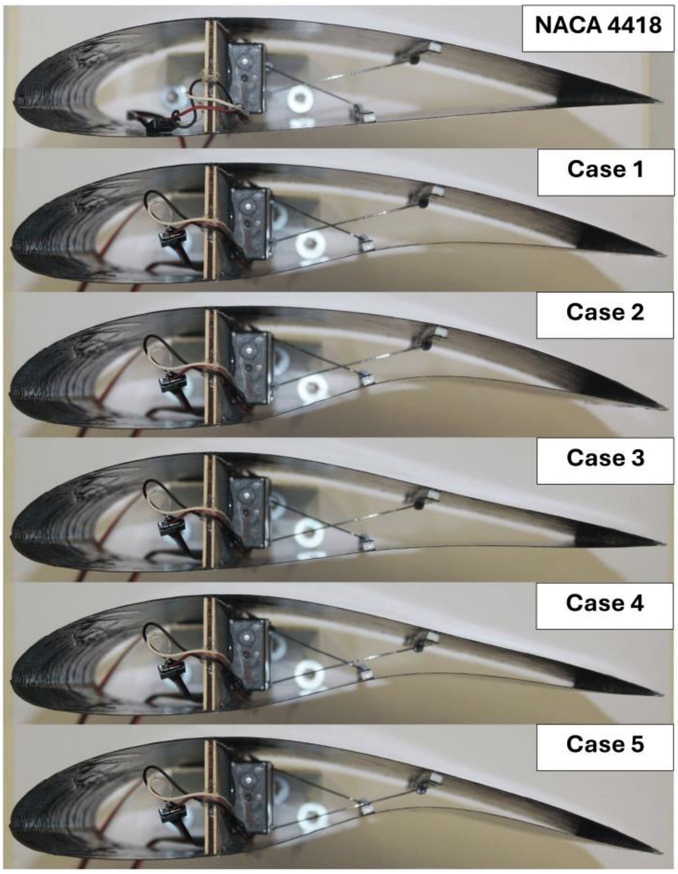

Figure 3.9 – Wing panel experimental actuation results.

In this prototype experimental test, successful actuation of both skins was achieved, effectively demonstrating airfoil morphing. However, the morphing amplitude was limited by the stringers positioning, as the control rod actuating the upper surface approached the lower surface stringer in experimental case "5". This issue could be avoided by adjusting the positioning of both stringers as intended – in this particular case, the upper surface stringer could be positioned closer to the wing spar.

3.4 Structural Numerical Model

This section details the development of two computational models of the morphing concept. The first model seeks to accurately represent the manufactured prototype to validate both the numerical model and the quality of the wing panel manufacturing, as well as the testing conducted on the CFRP composite material. The second model serves as a foundation for constructing a surrogate model, offering a simplified representation to reduce the computational cost associated with the analyses.

In both models, the skin is represented using regular shell-type finite elements, while the other components are modelled with 3D quadrilateral finite elements. The properties of the shell-type finite elements are defined within the *Ansys* software, where the user specifies the composite lay-up configuration and the material mechanical properties for each ply in the "Ansys Composite PrepPost" module. The CFRP properties utilized in the numerical models correspond to those experimentally determined, while the silicone rubber properties are detailed in *Table 3.4*.

Mesh refinement studies are conducted on the skin to ensure that the mesh density does not significantly influence the structural displacements. Specifically, the maximum trailing-edge deflection is used as a reference. The mesh is deemed adequate when the deflection result deviates by less than 1.0% compared to the deflection obtained with the previous mesh, as the consequent new mesh has an increased number of finite elements.

The computational calculations impose boundary conditions that fix all six degrees-of-freedom (three linear displacements and three rotations in 3D space) at the elements of the wing spar and any control horn or stringer that is not actuated. The interface between the skin elements and the wing spar and stringers employs the Node-to-Point Contact (NPC) formulation approach. Additionally, the large deflections option is enabled.

Both models simulate the structural morphing actuation. Once the computations are completed, the resulting airfoil geometries are derived from the centre-panel nodal displacements and subsequently analysed using *XFOIL* with a resolution of 257 panel nodes.

Finally, *Table 3.6* summarizes the hardware specifications of the computer utilized for the FEM computations.

Table 3.6 – Computer hardware specifications.

Processor	Model	Intel Core i5-8250U
	Core count	4
	Clock speed	1.60 GHz
Random-access memory	8.00 GB	

3.4.1 Detailed Structural Numerical Model

The representative numerical model of the prototype includes a detailed representation of the servomotors, complete with their control horns and control rods, which are modelled as hinged at both ends. In this approach, these components, along with the stringers, are treated as rigid bodies, under the assumption that they do not experience significant strains in the manufactured prototype. Actuation is simulated by applying moments at the articulations of the control horns where they connect to the servomotors, thereby replicating the real-world actuation of the prototype. *Figure 3.10* illustrates this comprehensive computational model.

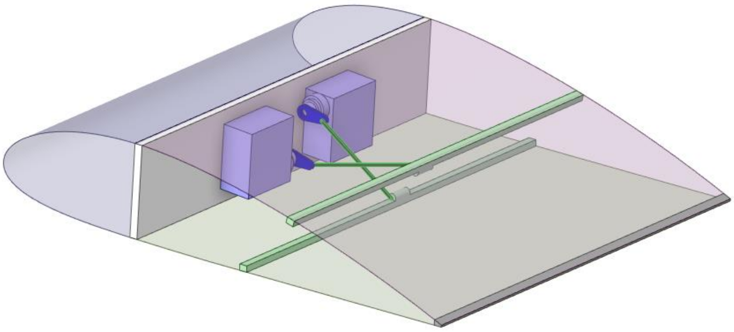

Figure 3.10 – Detailed wing panel computational model.

Although the control rods in the numerical model have a different geometry from those used in the prototype, this discrepancy is justified by the use of rigid body modelling. This approach simplifies the modelling of the control rods' hinged connections and produces actuation consistent with that of the prototype.

3.4.2 Simplified Structural Numerical Model

The simplified numerical model of the concept excludes the servomotors, control rods, and control horns, applying forces directly to the stringers, which are modelled as rigid bodies. These forces are distributed along the wing span and directed to the connections between the wing spar and the opposite skin. This approach focuses primarily on investigating the structural displacements of the structure's skin and the resulting airfoil geometries. *Figure 3.11* illustrates this model.

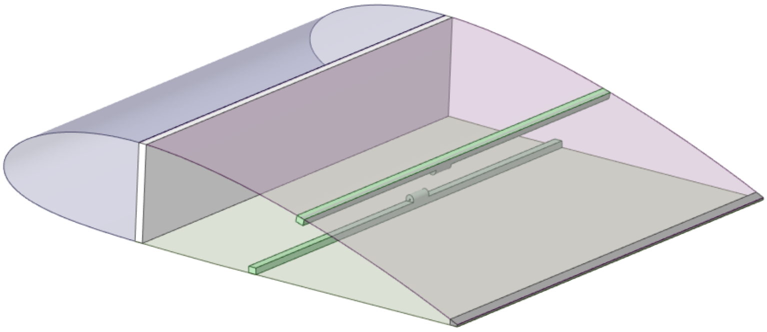

Figure 3.11 – Simplified wing panel computational model.

3.4.3 Results

The study conducted to determine which properties – tensile or flexural – are better suited for the numerical model of the morphing concept skin revealed that the flexural properties yield more precise results, which were subsequently used in the final numerical model. The mesh refinement study on the modelled skin is illustrated in *Figure 3.12*, which plots the maximum trailing-edge deflection as a function of the number of finite elements per unit area.

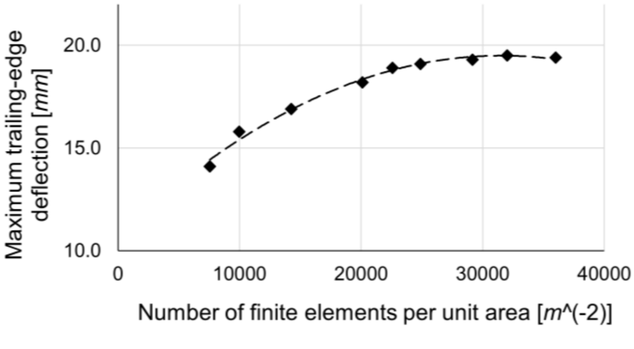

Figure 3.12 – Mesh refinement study on the modelled wing panel skin.

Using a criterion of 1.0 % deflection variation, the value of 24.9×10^3 finite elements per unit area was selected for the FEM computations. This results in a total of 2594 shell-tpe finite elements.

For the comparison of experimental and computational results, *Figure 3.13* illustrates the airfoil geometries obtained from experimental tests and numerical FEM computations using the detailed model. Additionally, *Table 3.7* provides a comparison of the trailing-edge deflection values for both cases, along with the associated deviation relatively to the wing panel chord.

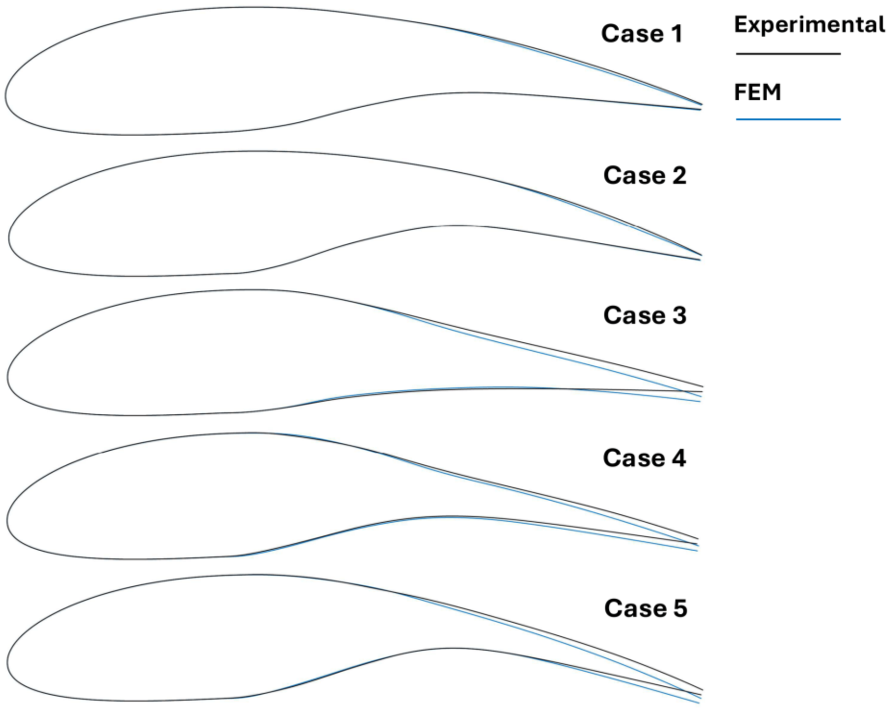

Figure 3.13 – Experimental and numerical wing panel morphing airfoil geometries comparison.

Table 3.7 – Trailing-edge deflection value comparison between the experimental and computational results.

Case	**Trailing-edge deflection** $[mm]$		**Deviation [%]**	**Deviation relative to chord [%]**
	FEM	Experimental		
1	4	3	33.3	0.4
2	7	7	0.0	0.0
3	8	4	100.0	1.6
4	11	8	37.5	1.2
5	15	11	36.4	1.6

Comparing the experimental results with the computational ones, it is possible to conclude that in two cases – where only the lower surface skin was actuated – the airfoil geometries obtained are very similar, with a trailing-edge deflection difference of $0.4\ \%$ of the chord in the first case and no difference in the second. However, when the upper surface skin was actuated, the discrepancies between the results became more pronounced. The numerical results showed a greater displacement of the upper surface skin points, increasing the trailing-edge deflection compared to the experimental tests. Nonetheless, the difference between these values did not exceed $1.6\ \%$ of the chord (with the maximum difference being $4\ mm$); however, the relative deviations reach up to $100.0\ \%$ of the experimentally obtained values. This occurs because the measured deflections are relatively small, causing even minor absolute deviations to result in significant relative differences.

In fact, errors in the experimental setup may have influenced these results, as two different multimeters were used to measure the input current of the servomotors. The multimeter measuring the current of the lower surface servomotor provided more stable readings over time, while the other showed erratic fluctuations, making the current values more challenging to measure accurately. However, the computational model itself demonstrated a high level of accuracy when compared to the physical model, allowing the morphing concept to be reliably implemented and analysed through computational simulations with a significant degree of precision.

Regarding the CFRP properties obtained from the experimental tests, it can be stated that they were accurately determined, as they were used in the computational model of the wing panel, and the results were close to the experimental ones. For this model, the properties obtained from the flexural test were used, as they proved to be the most accurate for the specific scenario, especially since the skin was indeed subjected to bending loads.

To compare the equivalence between the detailed and simplified numerical models under actuation case "5", the actuation torques of the servomotors, their corresponding moment arms and positions of the control horns in the final stable morphing wing panel configuration were analysed. The torque of $0.220\ N \cdot m$ from the upper surface servomotor corresponds to a distributed force of $87.3\ N/m$ on the upper surface stringer, while the torque of $0.197\ N \cdot m$ from the lower surface servomotor corresponds to a distributed force of $73.5\ N/m$ on the lower surface stringer. *Figure 3.14* illustrates the numerical wing panel geometries for this morphing configuration, detailing the structural displacements.

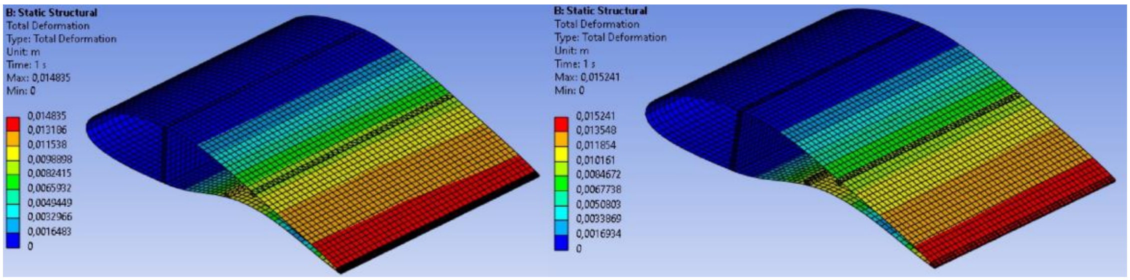

Figure 3.14 – Detailed (on the left) and simplified (on the right) numerical models' wing panel morphing geometries comparison.

The results demonstrate a strong equivalence between the detailed and simplified numerical models, as both produced nearly identical morphing wing panel geometries under equivalent actuation conditions. The detailed numerical model calculated a trailing-edge displacement of $14.8\,mm$, while the simplified model yielded a value of $15.2\,mm$, resulting in a relative deviation of 2.63%. This deviation is considered relatively small, highlighting the reliability of the simplified model.

In fact, the detailed numerical model required approximately 3 hours of computation per actuation case, whereas the simplified numerical model completed its calculations in just 10 minutes. These findings underscore the importance of computational simplification for the structure and actuation of the real wing panel, provided that the equivalence between the detailed and simplified numerical models is maintained to a high degree of accuracy. This further validates the use of a surrogate model for the design of a real wing incorporating the morphing concept. By limiting FEM calculations to a select number of specific cases, the surrogate model enables predictions across the entire design space, significantly reducing the overall computational cost and ensuring an efficient design process.

Chapter 4

Surrogate Model

This chapter presents the development of a surrogate model designed to evaluate the potential aerodynamic benefits of implementing the airfoil morphing concept. It begins with an overview of surrogate models in general, followed by a detailed explanation of the methodology used for constructing a surrogate model, and concludes with the results obtained.

4.1 Overview of Surrogate Models

Forrester et al. [73] provided a detailed explanation of the process involved in constructing a surrogate model, covering its key concepts. These ideas were combined with those presented by Martins et al. [74] to form the basis of this section, as well as the methodology and equations used in the surrogate model development.

Engineering design involves decision-making based on analysis, but these analyses, particularly computational ones, can be resource-intensive. A surrogate model serves as an approximate representation of a functional output, essentially creating a "curve fit" to underlaying data [74]. Its simplest and most common application is to supplement the results of a single, resource-heavy simulation code, which needs to be run for a range of possible inputs dictated by a design strategy [73]. Additionally, surrogate models are valuable for exploring the design space, helping to understand how objectives and outputs vary with respect to design variables, and identifying which variables most impact the objective function, as well as their interrelationships.

The process of constructing a surrogate model involves the following steps:

1) **Selection of key design variables**: in complex, multi-variable engineering problems, it is essential to identify the variables that significantly affect the objective function to simplify the surrogate model construction.
2) **Sampling**: a sampling plan is developed to explore the design space, choosing points (combinations of design variable values) where the objective function will be evaluated.

3) **Computation of the objective function**: the objective function is calculated at the sampled points using computational simulations or physical experiments to gather necessary data.
4) **Model construction**: the surrogate model is built by selecting the base functions that best fit the data obtained from the objective function computations.
5) **Result visualization**: the surrogate model results are visualized to analyse and understand the design space. While optimization of the objective function is often a part of this process, it is not covered in this work.

4.1.1 Sampling

The sampling methods, or sampling plans, determine the points used in constructing a surrogate model. Since the approximation models tend to be more accurate in the vicinity of the points where the objective function is evaluated, it is crucial to ensure a uniform distribution of points to achieve consistent model precision across the entire design space. A sampling plan that features well-distributed points throughout the design space is referred to as *space-filling*. The most commonly employed sampling methods are as follows [74]:

- **Full Factorial Sampling (FFS)**: this method involves discretizing each dimension of the problem and selecting points for all combinations of the resulting grid. As the number of design variables increases, the number of points grows exponentially, making it an inefficient sampling plan for high-dimensional problems.
- **Latin Hypercube Sampling (LHS)**: this method is based on a random process but is more efficient than purely random sampling, ensuring a uniform projection of points across all dimensions. However, since this method may not inherently produce a space-filling distribution, an optimization problem must be formulated to maximize the distance between sampling points.
- **Low-Discrepancy Sequences (LDS)**: this approach generates deterministic sequences of points that are well-distributed across the design space by varying point density. It is particularly suitable for models where an initial sampling plan is needed, which can then be supplemented with additional points in key locations to optimize the objective function.

4.1.2 The Modelling Process

The modelling process begins by dividing the points generated from the sampling plan into two sets: one for model training and the other for model testing. During the model training phase, the basis functions of the model are selected. These basis functions define the structure of the model, and their parameters are estimated using an optimization method to achieve the best fit for the provided data points. The following basis functions are among the most commonly used [74]:

- **Polynomial Functions**: polynomial functions consist of terms with coefficients that need to be estimated. These polynomials can be of any desired order, and each term can involve one or more variables. The terms can be linear or nonlinear. Polynomials offer several advantages, including simplicity of interpretation and the ability to derive.
- **Radial Basis Functions**: radial basis functions rely on the distance between a point in space and the sampling points. They provide a way to model the function based on its proximity to known data points, making them particularly useful for capturing the local behaviour of the function.
- **Kriging**: Kriging is a widely used surrogate modelling technique that falls under the category of radial basis functions. Rather than tuning the parameters of a functional form that describes what the function is, Kriging adjusts the parameters of a statistical model to describe how the function behaves. This method also provides a probability estimate for the function's value at any point in the design space, making it suitable for highly nonlinear simulations where a parametric form of the function is not required.
- **Deep Neural Networks**: deep neural networks are also particularly effective for modelling highly nonlinear functions. Inspired by the neural structure of the human brain, these networks consist of layers of interconnected nodes or neurons. Each neuron represents a simple function, and the network forms complex composite functions by chaining these simple functions together.

One effective methodology for selecting the most appropriate basis functions for a particular set of data is cross validation. This approach is also valuable for characterizing the error after the basis functions have been chosen and for preventing overfitting. Overfitting occurs when a model has too many degrees-of-freedom and fits the data set too closely, resulting in poor model predictive ability.

Cross validation involves splitting the training data into two subsets: one subset is used for training the model, while the other is used to assess the model's predictive error. The most commonly used methods of cross validation are as follows [73]:

- **Simple Cross Validation**: the training data is randomly divided into a training set and a validation set, typically in proportions such as 70% and 30%, respectively. Each candidate model is trained using the training set, and its predictive error is assessed with the validation set. The model with the lowest error is selected as the best.
- **k-fold Cross Validation**: the training data is randomly divided into a defined number of subsets, or folds. The model is trained on all but one fold, which is reserved for validation. This process is repeated for each possible combination of training and validation folds, and the model with the lowest generalized error is selected as the best. Hastie et al. [75] suggest dividing the data into compromise values of 5 or 10 folds.

The next phase is model testing, which involves evaluating the model using the testing set of data. This phase assesses the predictive capabilities of the model and verifies whether the sampling plan provides a good fit to the data. Various metrics are employed for this evaluation, including the root mean squared error and the correlation coefficient.

Finally, the process of constructing the surrogate model concludes with the visualization of the results. This step is crucial for interpreting and understanding the function's behaviour and the design space.

4.2 Surrogate Model Construction

The objective is to model the objective function f with an approximate function $\hat{f}$. $f(\boldsymbol{x})$ is a function or performance metric defined by a *k-vector* of design variables $\boldsymbol{x} \in D \subset \mathbb{R}^k$, where D is the *design space*. The only available information about f, beyond the assumption of continuity, is obtained through discrete *observations* or *samples* $\{\boldsymbol{x}^{(i)} \rightarrow y^{(i)} = f(\boldsymbol{x}^{(i)}), i = 1, m\}$ (where m is the number of sampling points), which are treated as realizations of a stochastic process.

The objective functions are selected to best characterize the aerodynamic performance of the airfoil obtained through morphing and to assess the potential benefits of applying the presented concept. Therefore, the chosen objective functions are: the maximum lift coefficient, $C_{l_{max}}$, the maximum lift-to-drag ratio, $(C_l/C_d)_{max}$, and the pitching moment coefficient corresponding to the maximum lift-to-drag ratio, $C_{m_{(C_l/C_d)_{max}}}$.

4.2.1 Design Variables

The description of the proposed airfoil morphing concept has already outlined all its potential design variables. Given the large number of these variables, it is essential to identify which ones have a significant influence, not only on the values of the objective functions but also on the resulting morphing airfoil geometries:

- **Airfoil**: the airfoil is a critical design variable in the morphing concept that significantly influences the objective functions outcomes. A preliminary study was carried out using three different airfoils – “NACA 2412”, “NACA 2415”, and “NACA 4418” (with maximum relative thicknesses of 12%, 15 %, and 18%, respectively). The study demonstrated that while the morphing actuation affected the objective functions similarly across all three airfoils, the morphing amplitude and the magnitudes of the objective functions varied. Due to its greater maximum relative thickness, the “NACA 4418” airfoil was selected for prototype implementation, facilitating both manufacturing and experimental testing. Consequently, the surrogate model is based on this airfoil, as it is intended to assess the potential benefits of the morphing concept’s practical application, which remain consistent across the three airfoils preliminarily studied.
- **Upper and lower surface skin thicknesses**: these two design variables are crucial for the morphing concept. However, they must be designed with the structure’s fail-safe behaviour in mind, as well as the specific application case, which also depends on other design variables. As a result, they are not included in the surrogate model. A preliminary study indicated that increasing the skin thickness primarily leads to higher actuation forces for the same morphing amplitude, without significantly influencing other aspects of performance. Therefore, these variables are not relevant for the current study, and the base values used for the surrogate model are the same as those applied in the prototype.
- **Wing spar placement**: this design variable plays a critical role, significantly influencing the objective functions values and the potential benefits of morphing, as shown by preliminary studies. Consequently, it is considered in the construction of the surrogate model.

- **Lower surface stringer placement**: this design variable significantly influences the geometry of the morphing airfoils, and consequently impacts the objective functions. Therefore, it is included in the surrogate model.
- **Upper surface stringer placement**: to ensure the fail-safe behaviour of the structure, the upper surface, subjected to higher aerodynamic loads than the lower surface, must have a greater skin thickness. As a result, the upper surface stringer placement does not significantly affect the morphing airfoil geometry and is not considered in the surrogate model.
- **Reynolds number**: this design variable has a significant impact on the values of the objective functions and is thus included in the surrogate model.
- **Actuation forces**: the actuation forces applied to the upper and lower surface skins affect the geometry of the morphing airfoil and, consequently, the objective functions. For this reason, they are also considered in the surrogate model.

Therefore, the following five design variables are considered in the construction of the surrogate model: wing spar placement relative to the airfoil's chord, x_{WS}, lower surface stringer placement relative to the airfoil's chord, x_{LS}, Reynolds number, Re, upper surface stringer distributed force, f_{US}, and lower surface stringer distributed force, f_{LS}, resulting in a five-dimensional problem ($k = 5$). These variables are normalized between 0 and 1, i.e., scaled to the unit cube, making the design space $D = [0,1]^k$. This normalization simplifies the surrogate model construction process and prevents scaling issues. The normalized design variable x_i, $x_i{}'$, is calculated using *Equation 4.01*,

$$x_i' = \frac{x_i - x_{i,min}}{x_{i,max} - x_{i,min}}\,, i = 1, k \qquad (4.01)$$

where $x_{i,min}$ and $x_{i,max}$ are the minimum and maximum values that the variable x_i can assume, respectively. It is important to note that the maximum values of the distributed forces depend on the wing spar placement. In this case, conditional normalization is used, where the maximum value of the variable x_j is a function of other variable x_i value, i.e., $x_{j,max} = x_{j,max}(x_i)$. *Table 4.1* presents the minimum and maximum values that each design variable can assume, with the maximum values of the distributed forces determined through a dedicated study.

Since the upper surface stringer cannot maintain a constant position as the wing spar placement varies, its placement, x_{US}, is calculated using *Equation 4.02*.

Table 4.1 – Design variables minimum and maximum values.

Variable		Minimum value	Maximum value
$\boldsymbol{x_{WS}}$	$-$	0.30	0.50
$\boldsymbol{x_{LS}}$	$-$	0.55	0.70
$\boldsymbol{Re}$	$-$	250×10^3	1×10^6
$\boldsymbol{f_{US}}$	N/m	0	$3x_{WS} + 10$
$\boldsymbol{f_{LS}}$	N/m	0	$3x_{WS} + 10$

$$x_{US} = 0.5x_{WS} + 0.5 \qquad (4.02)$$

4.2.2 Sampling

To obtain the sampling plan, the LHS method with the space-filling property is chosen. Since the objective is not to advance with the optimization of the objective functions, there is no need to add extra points to the initial sampling plan. One of the most widely used measures to evaluate the uniformity (*space-fillingness*) of a sampling plan is the *maximin* metric introduced by Johnson et al. [76].

Let d_1, d_2, ..., d_m represent the unique values of distances between all possible pairs of points in a sampling plan $\boldsymbol{X}$ ($\boldsymbol{X} = \{\boldsymbol{x}^{(1)}, \boldsymbol{x}^{(2)}, \dots, \boldsymbol{x}^{(m)}\}$), sorted in ascending order. Further, let $J_1, J_2, \dots, J_m$ be defined such that J_i is the number of pairs of points in $\boldsymbol{X}$ separated by the distance d_j. Considering the following: *we call* $\boldsymbol{X}$ *the maximin plan among all available plans if it maximizes* d_1*, among plans for which this is true, minimizes* J_1*, among plans for which is true, maximizes* d_2*, among plans for which is true, minimizes* J_2*, ..., minimizes* J_m. The distance between the points is computed using the most-widely used *p-norm* of the space, d_p, given by *Equation 4.03*.

$$d_p\left(\boldsymbol{x}^{(i_1)}, \boldsymbol{x}^{(i_2)}\right) = \left(\sum_{j=1}^{k} \left|x_j^{(i_1)} - x_j^{(i_2)}\right|^p\right)^{\frac{1}{p}} \qquad (4.03)$$

For $p = 1$, the distance metric is the rectangular distance, while $p = 2$ corresponds to the *Euclidean norm*. Although the rectangular distance is computationally less expensive, the *Euclidean norm* is used in this work.

Searching across a space of potential sampling plans can be achieved through pairwise comparisons. In theory, an optimization algorithm could use the *maximin* metric as a comparative objective. However, experimental evidence (Morris et al. [77]) suggests that the resulting landscape may be deceptive and challenging to navigate effectively. Therefore, the following scalar-valued criterion function, as defined by Morris et al. [77], is employed to rank competing sampling plans, as expressed in *Equation 4.04*.

$$\Phi_q(\boldsymbol{X}) = \left(\sum_{j=1}^{m} J_j d_j^{-q} \right)^{\frac{1}{q}} \qquad (4.04)$$

The value of Φ_q indicates the quality of the space-filling properties of $\boldsymbol{X}$; smaller values of Φ_q signify better space-filling characteristics. Morris et al. [77] recommend minimizing Φ_q for $q = 1{,}2{,}5{,}10{,}20{,}50$, and 100, and then selecting the best plan based on the actual *maximin* definition.

To establish the space-filling sampling plan, $m = 25$ sampling points are selected. These points are then combined with those from the case studies presented in *Chapter 5*, forming the final sampling plan with a total of 211 points.

4.2.3 Modelling

With five design variables, visualizing the results becomes a complex challenge. One key goal of constructing this surrogate model is to identify which variables have the most significant impact on the objective functions, how they influence these functions, and how they interact with each other. To achieve this, a polynomial model is chosen as a foundational approach, as it provides a clear equation that relates the values of the objective functions to the design variables. This simplifies results visualization and can indicate the ease of design and implementation of the proposed morphing concept – especially if the resulting polynomial functions are simple.

However, if the objective function turns out to be highly nonlinear, a Kriging model becomes a more suitable option. Although it does not yield a parametric form for the objective function approximation, the Kriging model allows for determining and comparing the influence of design variables through numerical values. Following this approach, the most influential design variables are identified. A sensitivity analysis is then performed to compute the derivates of the objective functions' approximations with respect to each variable, allowing those which provide the smallest gradients to be fixed. This reduces the number of variables and makes graphical result visualization more manageable.

Starting with the polynomial model, we consider a linear combination of the terms of a polynomial, as given by *Equation 4.05*, also considering that only variables with exponents of positive (or null) integer numbers are included, and the ψ's are picked from a catalogue of all possible terms of order not greater than the polynomial order, o.

$$\hat{f}(\boldsymbol{x}) = \sum_{i=1}^{n_b} w_i \psi^{(i)} \qquad (4.05)$$

where w_i is the polynomial term i coefficient and n_b is the number of basis functions (polynomial terms).

The selection of the polynomial order that best fits the data while preventing overfitting is achieved using *k-fold* cross validation, with $q_f = 10$ folds. Nine of these ten folds are used for model training, where the polynomial coefficients (included in the polynomial terms coefficients vector, $\boldsymbol{w}$) are obtained via the Maximum Likelihood Estimation method (MLE). The goal is to minimize the squared difference between the actual function values and the values estimated by the polynomial approximation, as described in *Equation 4.06*,

$$\min_{\boldsymbol{w}} \sum_{i=1}^{m_{tr}} \left[y^{(i)} - \hat{f}(\boldsymbol{x}, \boldsymbol{w}) \right]^2 \qquad (4.06)$$

where m_{tr} is the number of training points. It can be demonstrated that the MLE is equivalent to the Least Squares Method (LSM).

The tenth fold is used to validate the polynomial model. If a mapping $\xi\colon \{1, \dots, m_{tr}\} \to \{1, \dots, q_f\}$ describes the allocation of the m_{tr} training points to one of the q_f subsets and $\hat{f}^{-\xi(i)}(\boldsymbol{x})$ is the value (at $\boldsymbol{x}$) of the predictor obtained by removing the subset $\xi(i)$ (i.e. the subset to which observation i belongs), the cross validation measure, which is employed here as an estimate of the prediction error, is

$$\varepsilon_{cv}(\boldsymbol{w}) = \frac{1}{m_{tr}} \sum_{i=1}^{m_{tr}} L\left[y^{(i)}, \hat{f}^{-\xi(i)}\left(\boldsymbol{x}^{(i)}, \boldsymbol{w}\right) \right] \qquad (4.07)$$

The loss-function, L, is selected as the squared error, and thus the cross validation error is expressed as shown in *Equation 4.08*.

$$\varepsilon_{cv}(\boldsymbol{w}) = \frac{1}{m_{tr}} \sum_{i=1}^{m_{tr}} \left[y^{(i)} - \hat{f}^{-\xi(i)}\left(\boldsymbol{x}^{(i)}, \boldsymbol{w}\right) \right]^2 \qquad (4.08)$$

This process is repeated for all combinations of the folds, and for each polynomial order, the generalized cross validation error, ε_{cvg}, is then computed as shown in *Equation 4.09*.

$$\varepsilon_{cvg} = \sum_{i=1}^{q_f} \varepsilon_{cv,i} \qquad (4.09)$$

The optimal polynomial order is selected by identifying the one that yields the lowest generalized cross validation error. Given the limited number of sampling points – specifically, 159 points available for model training – and considering the five design variables, the polynomial degree is capped at 4. This is necessary to ensure that the number of data points exceeds the number of coefficients, which for a 4th-degree polynomial would be 126 points.

Upon selecting the polynomial degree, all training data points are utilized to compute the coefficients that yield the best fit for the approximation polynomial according to the MLE. Once the final polynomial is established, model testing is conducted using two key metrics: the Root Mean Squared Error, $RMSE$, and the correlation coefficient, r^2, defined by *Equations 4.10* and *4.11*, respectively.

$$RMSE = \sqrt{\frac{\sum_{i=1}^{m_{te}} \left(y^{(i)} - \hat{y}^{(i)} \right)^2}{m_{te}}} \qquad (4.10)$$

$$r^2 = \left(\frac{m_{te} \sum_{i=1}^{m_{te}} y^{(i)} \hat{y}^{(i)} - \sum_{i=1}^{m_{te}} y^{(i)} \sum_{i=1}^{m_{te}} \hat{y}^{(i)}}{\sqrt{\left[m_{te} \sum_{i=1}^{m_{te}} y^{(i)2} - \left(\sum_{i=1}^{m_{te}} y^{(i)} \right)^2 \right] \left[m_{te} \sum_{i=1}^{m_{te}} \hat{y}^{(i)2} - \left(\sum_{i=1}^{m_{te}} \hat{y}^{(i)} \right)^2 \right]}} \right)^2 \qquad (4.11)$$

where m_{te} is the number of model testing points.

The $RMSE$ is normalized by the range of the objective function. If r^2 exceeds 0.8 and the $RMSE$ falls below 0.1, we can conclude that the surrogate model demonstrates good predictive capabilities and is well-saturated with data.

Continuing with the Kriging model, it employs the following basis function of the form:

$$\psi^{(i)} = \exp\left(-\sum_{j=1}^{k} \theta_j \left|x_j^{(i)} - x_j\right|^{p_j}\right) \qquad (4.12)$$

where θ_j is a parameter that indicates how "active" the function is in the variable x_j, while p_j is a "smoothness" parameter that affects the correlation between two sampling points. Examining θ_j for all variables reveals the most influential ones.

Forrester et al. [73] provided a set of *MATLAB* functions that implement the Kriging model, which includes likelihood parameter estimation for this approach. These functions are adapted and utilized in the present work. After constructing the model, it undergoes a testing phase using the $RMSE$ and r^2 metrics, as presented in *Equations 4.10* and *4.11*, respectively.

Finally, for the sensitivity analysis, the gradients of the approximation function with respect to each variable are calculated using the partial derivative with the Finite Differences Method – FDM (with the central finite difference), as presented in *Equation 4.13*.

$$\frac{\partial \hat{f}(\boldsymbol{x})}{\partial x_i} = \frac{\hat{f}(x_1, \dots, x_i + h, \dots, x_k) - \hat{f}(x_1, \dots, x_i - h, \dots, x_k)}{2h} \qquad (4.13)$$

where h is a small step size, selected as $h = 1 \times 10^{-3}$.

4.2.4 Methodology Implementation

The computational implementation of the surrogate model construction is carried out using *MATLAB* [78], as several functions provided by Forrester et al. [73] are written in *MATLAB* and adapted for the present work.

The sampling plan is defined recurring to a set of functions provided by Forrester et al. [73].

For the polynomial model, the following functions are implemented:

- Main function: the sampling data (with normalized design variables and the corresponding obtained values of the objective function) is introduced, followed by a random split into model training and testing sets. The functions *polynomial* and *test_model* are called for model training and testing, respectively, and the results are then presented.

- *polynomial*: this function performs the model training, including the cross validation process to identify the polynomial order that best fits the known objective function values, constrained to a maximum degree of four, and that prevents overfitting. For each polynomial degree and fold, it invokes the *polyfitn* function (provided by D'Errico [79]), which employs the LSM to calculate the polynomial coefficients. The cross validation error is computed using *Equation 4.08*, and the generalized cross validation error is determined through *Equation 4.09*, using the *polyvaln* function, which computes the approximation function value with the obtained polynomial coefficients. The polynomial degree that yields the lowest generalized error is selected for the final model. Subsequently, the final polynomial is calculated using the entire training set, and the corresponding coefficients are presented. Since the design variables are normalized between 0 and 1, polynomial terms with coefficients significantly smaller in magnitude may be negligible. To address this, the user specifies a threshold value, below which the terms are filtered out, and the polynomial coefficients are recalculated to ensure only meaningful terms contribute to the objective function approximation.
- *test_model*: this function performs the testing of the obtained model by calculating the values of the $RMSE$ and the correlation coefficient, as defined in *Equations 4.10* and *4.11*, respectively. The testing is carried out using the data from the training set, which was reserved during the model training phase.

For the Kriging model implementation, the following functions are used:

- Main function: this function begins by introducing the sampling data and randomly splitting it into training and testing sets. It calls the *likelihood* and *pred* functions, provided by Forrester et al. [73], for model training, which involves determining the Kriging parameters and estimating the objective function values at other points within the design space, respectively. The *test_model* function is also invoked, performing the same testing process as described in the polynomial model implementation. Additionally, the variables with the greatest influence on the objective function are identified using the θ parameter, and sensitivity analysis is conducted for these variables using the *sensitivity_analysis* function. Finally, the results are displayed.
- *sensitivity_analysis*: this function computes the gradients of the objective function approximation with respect to a specified variable, as shown in *Equation*

4.13. It identifies the regions of the design space where this variable has minimal influence on the objective function. Consequently, the corresponding value of this variable is fixed, allowing for graphical presentation of the results. The function is adapted to accommodate the number of the most influential design variables identified in the previous step.

The *MATLAB* code implementing the above description is presented in *Appendix A*.

4.3 Results

Starting with the polynomial model, the results of the best polynomial fit for the objective functions – maximum lift coefficient, maximum lift-to-drag ratio, and the corresponding pitching moment coefficient – are expressed in *Equations 4.14*, *4.15*, and *4.16*, respectively. The results of the model testing, including the correlation coefficient and the $RMSE$ values, are also detailed.

$$C_{l,max} = 1.53 - 0.15x'_{WS}f'_{LS} + 0.12f'_{US}f'_{LS} + 0.34f'_{LS} + 0.11Re' \quad (4.14)$$

with $r^2 = 0.927$ and $RMSE = 0.0580$.

$$(C_l/C_d)_{max} = 70.2 + 33.4f'_{US}Re' - 29.1{Re'}^2 + 69.1Re' \quad (4.15)$$

with $r^2 = 0.926$ and $RMSE = 0.0738$.

$$C_{m_{(C_l/C_d)_{max}}} = -0.0882 + 0.0643x'_{WS}f'_{LS} - 0.0404x'_{LS}f'_{LS} - 0.1143f'_{LS} \quad (4.16)$$

with $r^2 = 0.896$ and $RMSE = 0.0962$.

It is important to note that the cross validation revealed that the second-order polynomial best fits all three objective functions, while preventing overfitting.

Regarding the Kriging model, the θ parameters for the three objective functions are presented in *Tables 4.2* to *4.4*. A higher value of θ indicates a grater influence of the corresponding variable on the objective function.

Maximum Lift Coefficient

Table 4.2 – Maximum lift coefficient Kriging model parameter θ value for each design variable.

Variable	f'_{US}	f'_{LS}	x'_{WS}	x'_{LS}	Re'
$\boldsymbol{\theta}$	7.60	6.66	1.90	0.70	0.45

This model achieved an r^2 value of 0.946 and an $RMSE$ of 0.0512.

The most influential design variables affecting the maximum lift coefficient are the distributed forces on the upper and lower surface stringers, followed by the wing spar placement. Therefore, the variable x'_{WS} can be fixed at the value where its variation causes negligible changes in the objective function. This occurs at $x'_{WS} = 0.13$, as shown in *Figure 4.1*, where the partial derivative of the objective function in order of this variable becomes zero. For this fixed value of x'_{WS}, and with x'_{LS} and Re' set to 0.5, *Figure 4.2* presents the plot of $C_{l_{max}}$ as a function of f'_{US} and f'_{LS}.

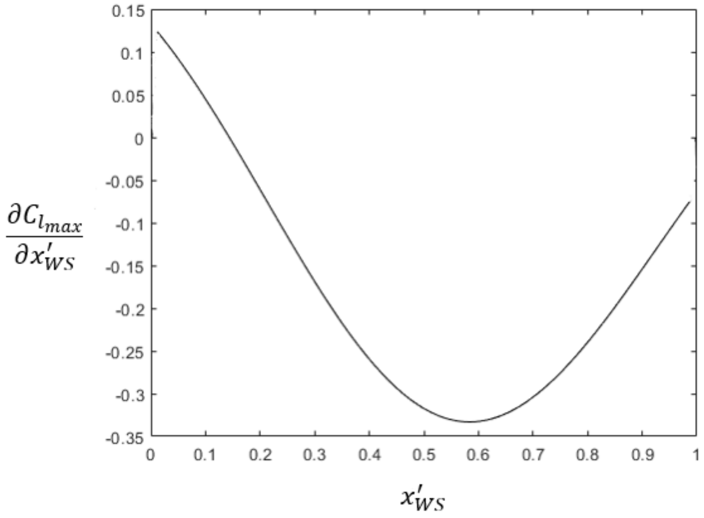

Figure 4.1 – Maximum lift coefficient partial derivative as a function of the wing spar placement.

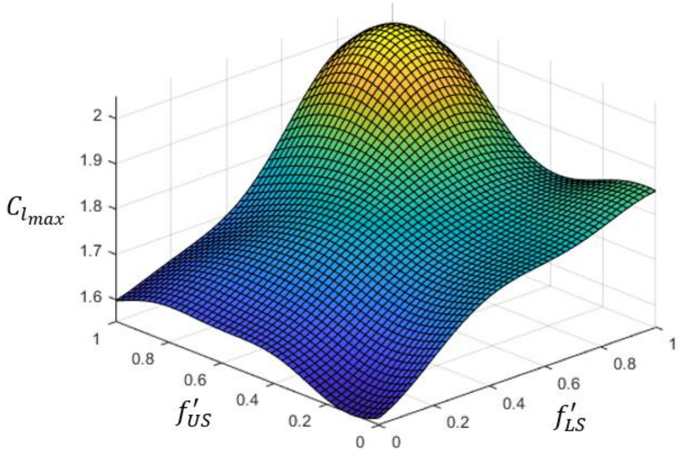

Figure 4.2 – Maximum lift coefficient as a function of the upper and lower surface stringers distributed forces.

Maximum Lift-to-drag Ratio

Table 4.3 – Maximum lift-to-drag ratio Kriging model parameter θ value for each design variable.

Variable	f'_{US}	Re'	f'_{LS}	x'_{WS}	x'_{LS}
θ	5.43	5.41	3.53	0.83	0.09

This model achieved an r^2 value of 0.966 and an $RMSE$ of 0.0483.

The most influential design variables affecting the maximum lift-to-drag ratio are the distributed force on the upper surface stringer and the Reynolds number, followed by the distributed force on the lower surface stringer. Therefore, the variable f'_{LS} can be fixed at the value where its variation causes negligible changes in the objective function. This first occurs at $f'_{LS} = 0.33$, as shown in *Figure 4.3*, where the partial derivative of the objective function in order of this variable becomes zero. For this fixed value of f'_{LS}, and with x'_{WS} and x'_{LS} set to 0.5, *Figure 4.4* presents the plot of $(C_l/C_d)_{max}$ as a function of f'_{US} and Re'.

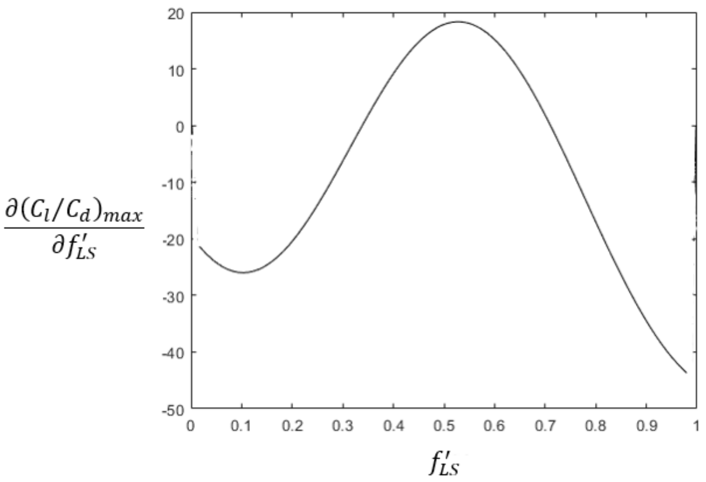

Figure 4.3 – Maximum lift-to-drag ratio partial derivative as a function of the lower surface stringer distributed force.

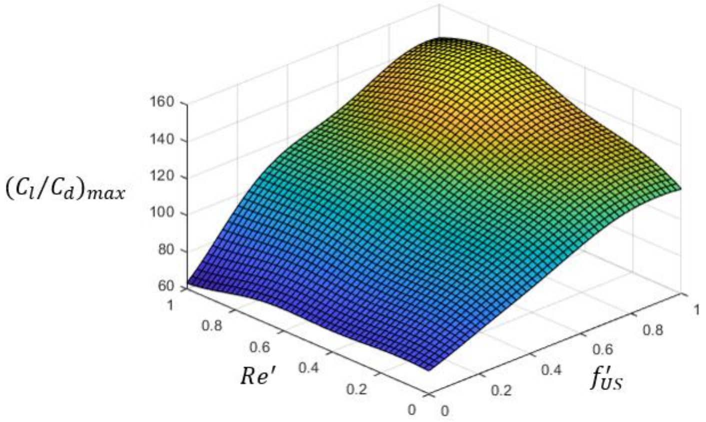

Figure 4.4 – Maximum lift-to-drag ratio as a function of the Reynolds number and the upper surface stringer distributed force.

Pitching Moment Coefficient for Maximum Lift-to-drag Ratio

Table 4.4 – Pitching moment coefficient corresponding to maximum lift-to-drag ratio Kriging model parameter θ value for each design variable.

Variable	f'_{US}	f'_{LS}	x'_{WS}	Re'	x'_{LS}
$\boldsymbol{\theta}$	8.99	8.77	1.10	0.63	0.58

This model achieved an r^2 value of 0.842 and an $RMSE$ of 0.0986.

The most influential design variables affecting the pitching moment coefficient at the maximum lift-to-drag ratio are the distributed forces on the upper and lower surface stringers, followed by the wing spar placement. Therefore, the variable x'_{WS} can be fixed at the value where its variation causes minimal changes in the objective function. This occurs at $x'_{WS} = 0.02$, as shown in *Figure 4.5*, where the partial derivative of the objective function in order of this variable becomes minimal over its range. For this fixed value of x'_{WS}, and with x'_{LS} and Re' set to 0.5, *Figure 4.6* presents the plot of $C_{m_{(C_l/C_d)_{max}}}$ as a function of f'_{US} and f'_{LS}.

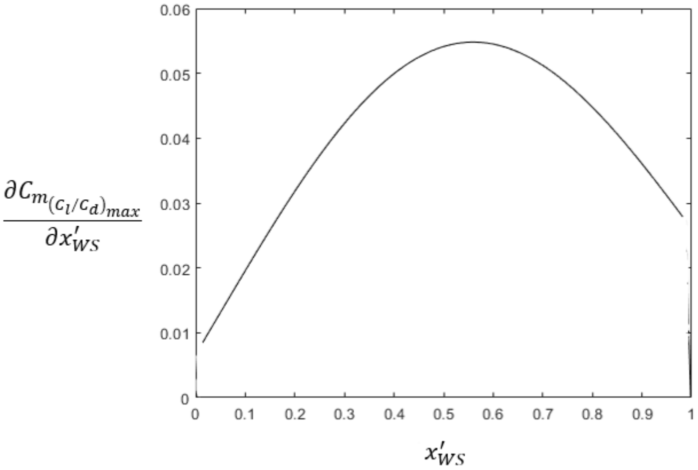

Figure 4.5 – Pitching moment coefficient corresponding to maximum lift-to-drag ratio partial derivative as a function of the wing spar placement.

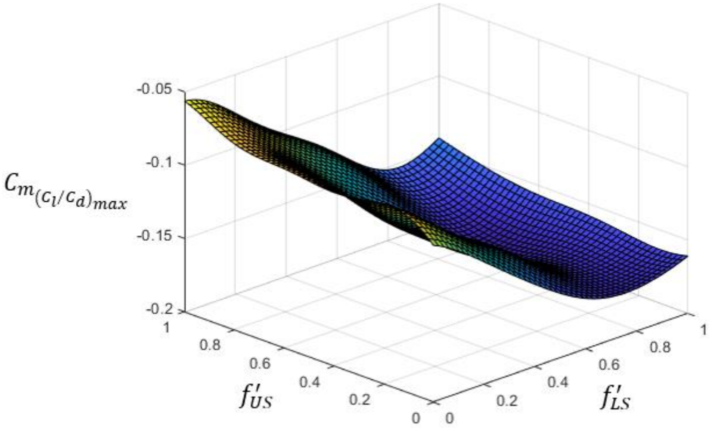

Figure 4.6 – Pitching moment coefficient corresponding to maximum lift-to-drag ratio as a function of the upper and lower surface stringers distributed forces.

The results from the surrogate model enabled a detailed analysis of the most influential design variables in the morphing concept, particularly concerning its aerodynamic performance. The polynomial model provided well-fitting second-degree polynomials for the given data, achieving a correlation coefficient greater than 0.8 and $RMSE$ values below 0.1 for all objective functions – maximum lift coefficient, maximum lift-to-drag ratio, and the corresponding pitching moment coefficient. These results indicate that the models possess good predictive capabilities and that the dataset was well saturated. Similarly, the Kriging model also exhibited these performance metrics, confirming its strong predictive ability and adequate data saturation for all three objective functions.

The polynomial model indicated that the maximum lift coefficient can be approximated by a second-degree function with a constant term equal to 1.53. This value corresponds to the maximum lift coefficient when all variables (normalized from 0 to 1) assume a value of zero, and it is the maximum lift coefficient of the "NACA 4418" airfoil in this condition, as shown in *Table 5.3*. The variables influencing this coefficient include the wing spar placement, the distributed forces on both stringers, and the Reynolds number. The variable with the most significant impact on this maximum coefficient is the distributed force on the lower surface stringer, as its term has the highest coefficient and interacts with other variables in additional terms. The Reynolds number term has a positive coefficient, which is corroborated by the case studies conducted, as a higher Reynolds number tends to increase the maximum lift coefficient. The term for the wing spar placement value has a negative coefficient, interacting with the force on the lower surface stringer. This is also supported by the case studies, as moving the wing spar closer to the trailing-edge limits the amplitude of the trailing-edge deflection, resulting in lower maximum lift coefficient values for the morphing airfoil. The term for the distributed force on the lower surface stringer has a positive coefficient, which is also validated by the case studies, as a higher value of this distributed force increases the trailing-edge deflection, thereby raising the maximum lift coefficient. Additionally, the term of the distributed force on the upper surface stringer interacts with the distributed force on the lower surface stringer, and equally has a positive coefficient. In fact, the force on the upper surface stringer contributes to increasing the trailing-edge deflection, which, when combined with the deflection caused by the force on the lower surface stringer, further enhances this deflection and increases the maximum achieved lift coefficient.

The Kriging model predicted that the distributed force on the lower surface stringer has the greatest effect on the maximum lift coefficient, followed by the distributed force on the upper surface stringer and the wing spar placement. However, the Reynolds number was shown to have the least influence on this maximum coefficient, which contrasts with the results from the polynomial model and the case studies. Despite this, the Kriging model achieved a higher correlation coefficient than the polynomial model. The plot of the maximum lift coefficient as a function of the distributed forces on both stringers (*Figure 4.2*), with the remaining variables fixed, shows that increasing these two variables leads to an increase in the maximum lift coefficient, which is also indicated by the polynomial model.

Regarding the maximum lift-to-drag ratio, the polynomial model produced a second-degree polynomial with the independent term coefficient equal to 70.2, which is very close to the value obtained for the "NACA 4418" airfoil under the condition where all variables are zero (72.8, as shown in *Table 5.3*). The variables that demonstrated the most significant influence on this coefficient were the Reynolds number and the distributed force on the upper surface stringer. The coefficient for the term of the distributed force (which interacts with the Reynolds number) is positive, indicating that its increase (together with the Reynolds number) leads to an increase in the maximum lift-to-drag ratio, as also confirmed by the case studies. Regarding the Reynolds number, this variable appears with a negative coefficient in its quadratic term and a positive coefficient in its linear term. Since the variables are normalized between 0 and 1, and the coefficient of the positive term is greater in absolute value than that of the negative term, an increase in the Reynolds number results in an increase in maximum lift-to-drag ratio, which is also validated by the case studies. However, the influence of the distributed force on the lower stringer was not captured by the resulting polynomial, despite the fact that this variable globally reduces lift-to-drag ratio.

The Kriging model, on the other hand, predicted that the distributed force on the upper surface stringer and the Reynolds number are the most influential variables on maximum lift-to-drag ratio, followed closely by the distributed force on the lower surface stringer, which also has a relatively high impact. This suggests that the Kriging model is more suitable for estimating the maximum lift-to-drag ratio. The graph of this parameter as a function of the Reynolds number and the distributed force on the upper surface stringer, shown in *Figure 4.4*, exhibits the same behaviour predicted by the polynomial model, as an increase in the values of these two variables leads to an increase in maximum lift-to-drag ratio.

For the pitching moment coefficient corresponding to maximum lift-to-drag ratio, the polynomial model predicted an independent term value of -0.0882, which is very close to the value determined in the case studies under null variable conditions (-0.0875, as shown in *Table 5.3*). This model predicted a greater influence from the wing spar position and the distributed force on the lower surface stringer. The term of the wing spar position (which interacts with the distributed force) has a positive coefficient, indicating that the pitching moment coefficient increases as this variable increases, as observed in the case studies. This effect is linked to the limitation it imposes on the trailing-edge deflection, which is largely influenced by the distributed force on the lower surface stringer. However, an increase in this distributed force leads to a reduction in the pitching moment coefficient (since the associated terms have negative coefficients), which is also confirmed by the case studies. The exception lies in the term where the wing spar position interacts with this distributed force, which does not seem to align with the expected results. In contrast, the case studies indicate that the one of the variables with a significant influence on this coefficient is the distributed force on the upper surface stringer, a factor not captured by the polynomial model.

However, the Kriging model reveals that the variable with the greatest influence on the pitching moment coefficient corresponding to maximum lift-to-drag ratio is the distributed force on the upper surface stringer, followed by the distributed force on the lower surface stringer and the wing spar position, which appears to be more consistent with the case studies results. The plot of the pitching moment coefficient for maximum lift-to-drag ratio, presented in *Figure 4.6*, shows that an increase in the upper surface stringer force leads to an increase in the pitching moment coefficient, while an increase in the lower surface stringer force causes a decrease in this coefficient. This behaviour is indeed consistent with the results from the case studies.

Chapter 5

Case Studies

This chapter presents the case studies chosen to further evaluate the proposed airfoil morphing concept, offering a more detailed analysis of its potential aerodynamic advantages in various scenarios, including different original airfoil geometries and the placement of its components within the wing structure.

The case studies complement the surrogate model analysis by providing an in-depth examination of the aerodynamic performance of the morphing concept. The objective is to obtain curves for key aerodynamic parameters: the lift coefficient as a function of the angle-of-attack (α), the lift-to-drag ratio as a function of the lift coefficient, and the pitching moment coefficient as a function of the lift coefficient. The specific case studies considered are outlined in *Table 5.1*, where the upper and lower surface skin thicknesses and airfoil chords match those used in the prototype.

Table 5.1 – Case studies characteristics.

Case study	**1**	**2**	**3**	**4**
Airfoil	“NACA 4418”	“NACA 4418”	“NACA 2412”	“NACA 2415”
x_{WS}	0.30	0.50	0.30	0.30
x_{US}	0.65	0.75	0.65	0.65
x_{LS}	0.55	0.70	0.55	0.55

Furthermore, the morphing concept is compared in performance with CHSs considering the case study “1”. The comparison employs the morphing configuration with maximum actuation forces applied to both stringers. Two equivalent deflections for the CHSs, denoted as δ_{HS}, are considered: one corresponding to an equal trailing-edge perpendicular-to-chord displacement value relative to the airfoil’s chord, d_{TE}, and the other corresponding to an equal increase in lift coefficient at zero angle-of-attack, $\Delta C_{l,\alpha_0}$. For the CHSs, two cases are examined: one with a chord ratio, c_{HS}, of 15.0% and another with a chord ratio of 30.0%.

Continuing with the results of these case studies, the nomenclature for the morphing airfoil geometries follows this template: “OriginalAirfoil_WS_US_LS_UF_LF”. This naming convention begins with the original airfoil’s name (prior to morphing), followed by the wing spar placement (WS), upper surface stringer placement (US), and lower surface stringer placement (LS), each expressed as percentage of the airfoil’s chord. Additionally, it includes the upper (UF) and lower (LF) surfaces distributed forces, given in N/m.

Case Study 1

Regarding the first case study, *Figures 5.1* to *5.3* show the resulting airfoil geometries for lower skin actuation only, upper skin actuation only, and both skins actuation, respectively. *Figures 5.4* to *5.6* present the aerodynamic metric curves – lift coefficient, lift-to-drag ratio, and pitching moment coefficient – corresponding to Reynolds numbers of 250×10^3, 500×10^3, and 1×10^6, respectively.

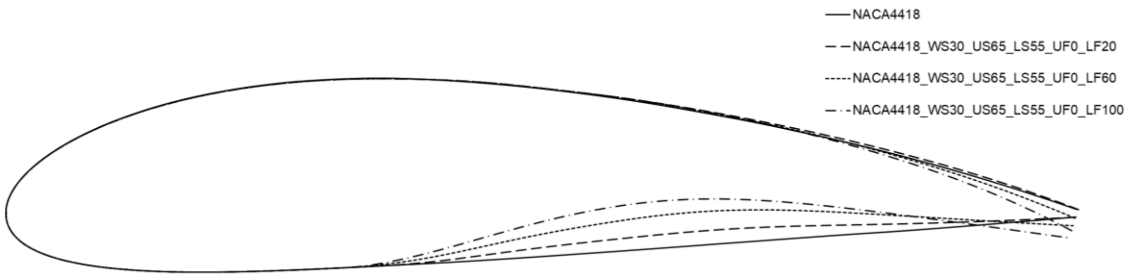

Figure 5.1 – Airfoil geometries obtained for lower surface skin actuation in case study 1.

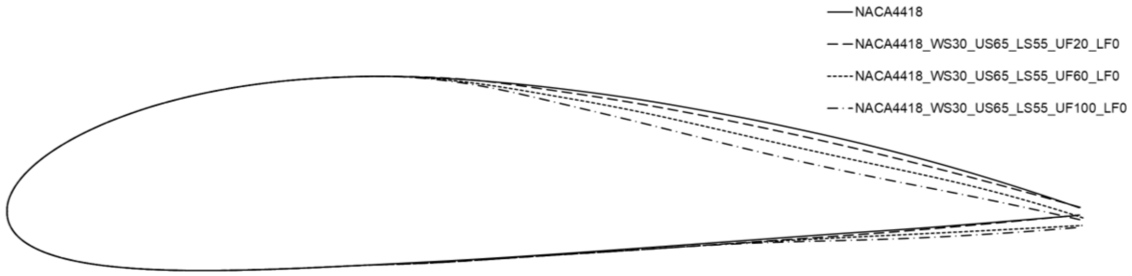

Figure 5.2 – Airfoil geometries obtained for upper surface skin actuation in case study 1.

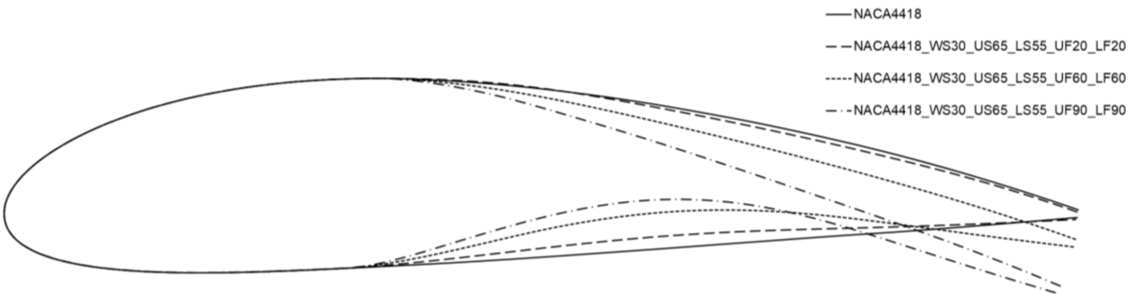

Figure 5.3 – Airfoil geometries obtained for upper and lower surface skins actuation in case study 1.

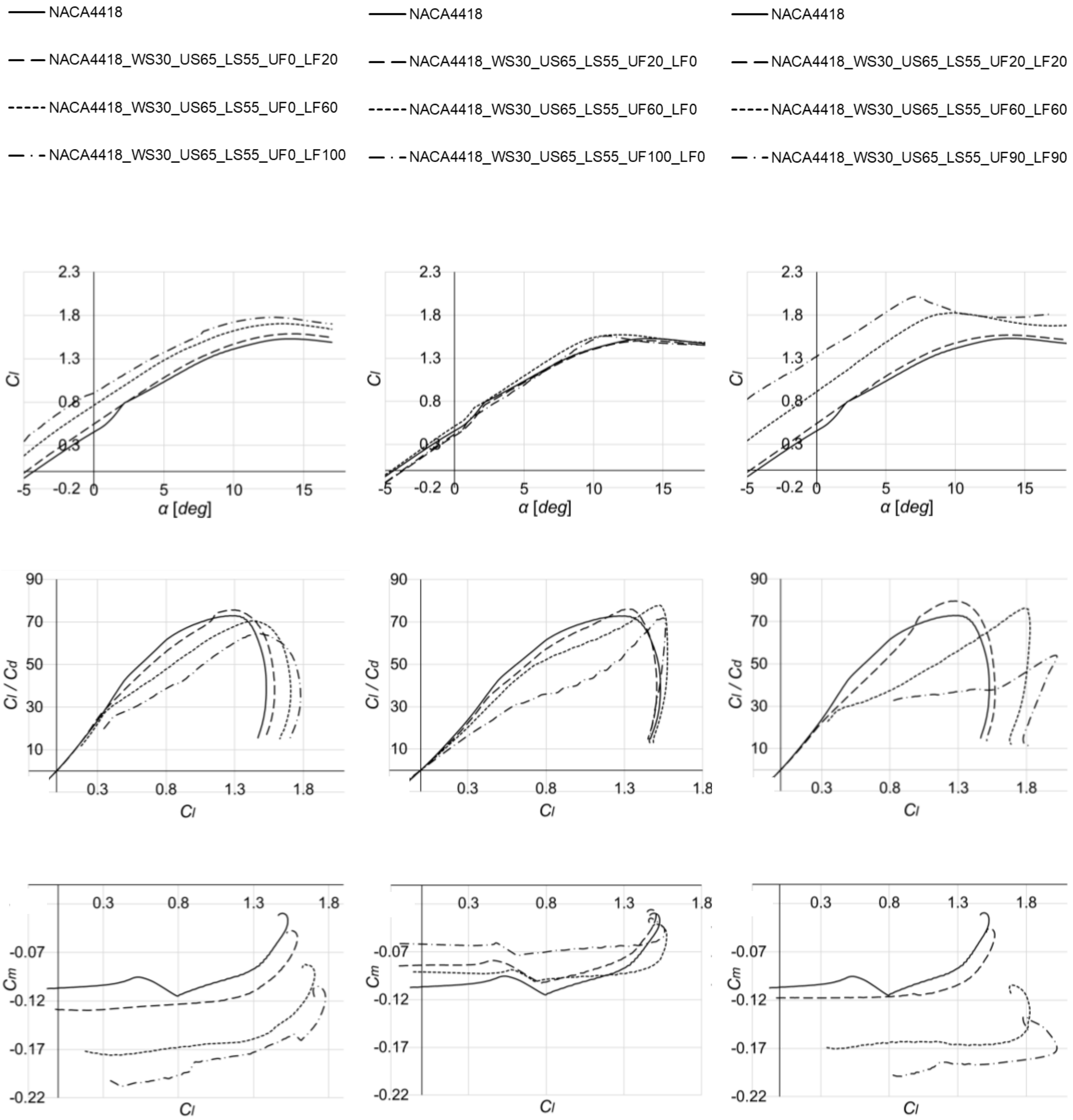

Figure 5.4 – Airfoils aerodynamic performance metrics for case study 1 and $Re = 250 \times 10^3$.

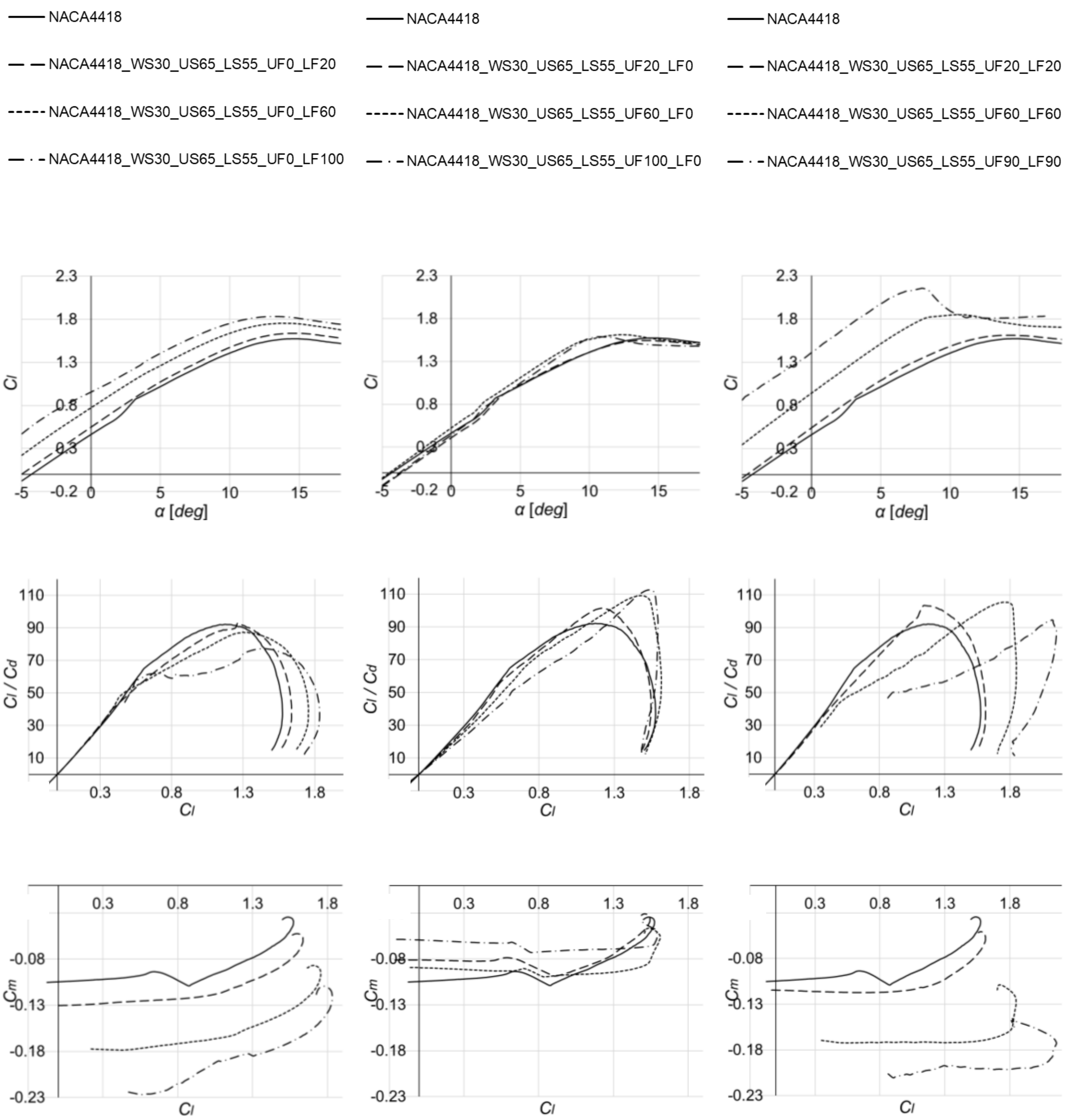

Figure 5.5 – Airfoils aerodynamic performance metrics for case study 1 and $Re = 500 \times 10^3$.

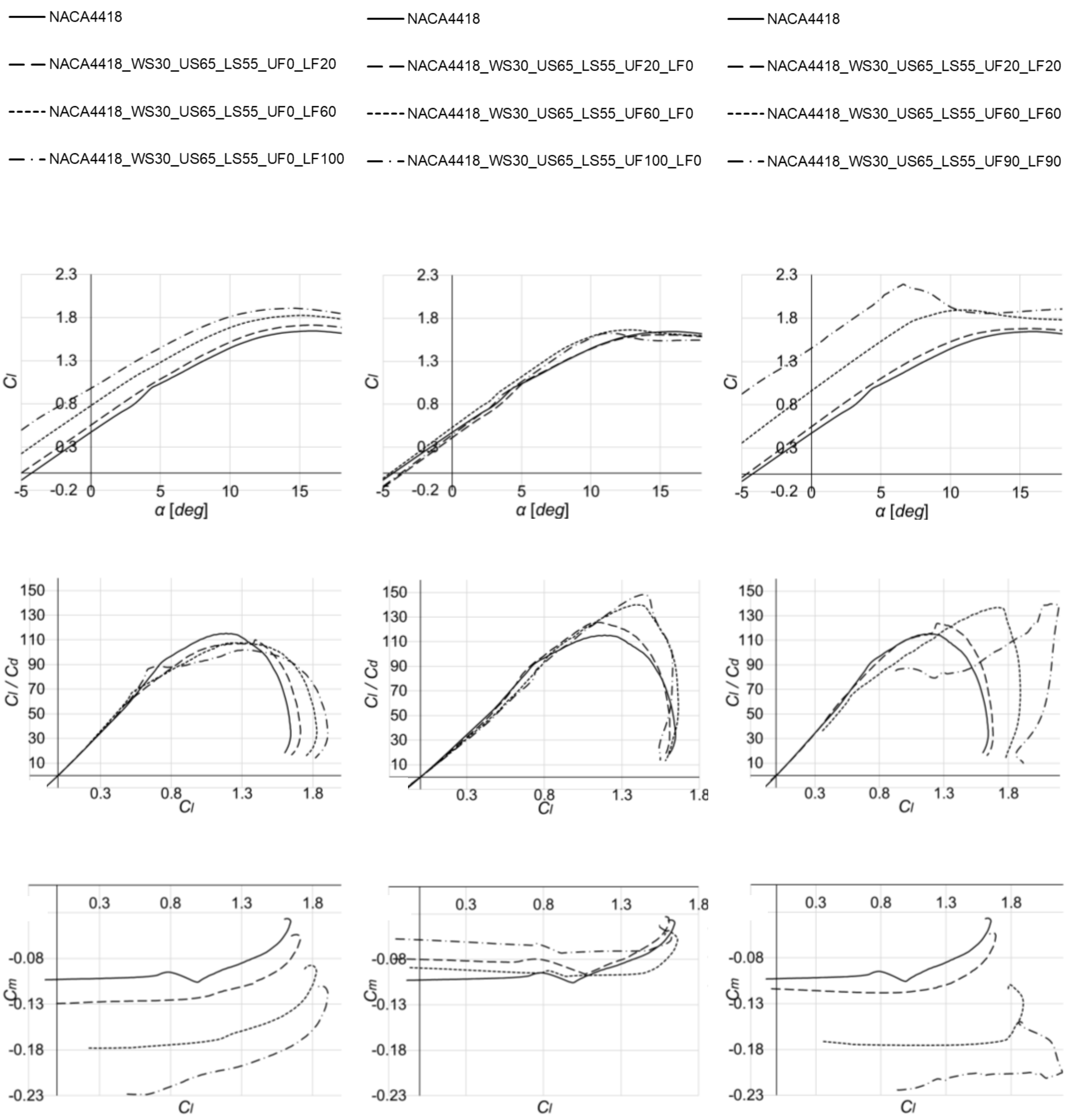

Figure 5.6 – Airfoils aerodynamic performance metrics for case study 1 and $Re = 1 \times 10^6$.

Additionally, *Figure 5.7* presents the safety margin values for each finite element of both the upper and lower skins, obtained using the maximum stress criteria.

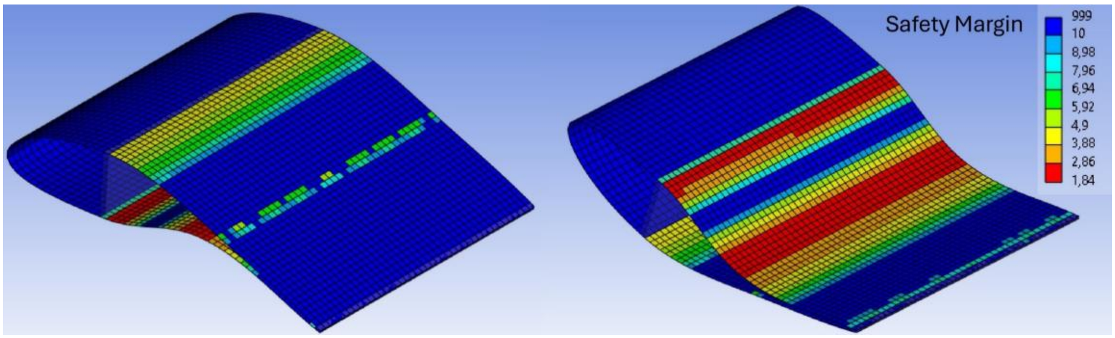

Figure 5.7 – Safety margin values for the upper and lower surface skins in case study 1.

Case Study 2

Regarding the second case study, *Figures 5.8* to *5.10* show the resulting airfoil geometries for lower skin actuation only, upper skin actuation only, and both skins actuation, respectively. *Figures 5.11* to *5.13* present the aerodynamic metric curves corresponding to Reynolds numbers of 250×10^3, 500×10^3, and 1×10^6, respectively.

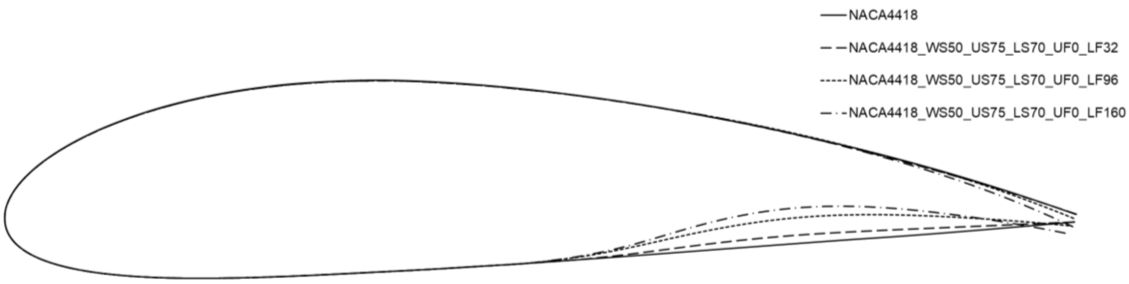

Figure 5.8 – Airfoil geometries obtained for lower surface skin actuation in case study 2.

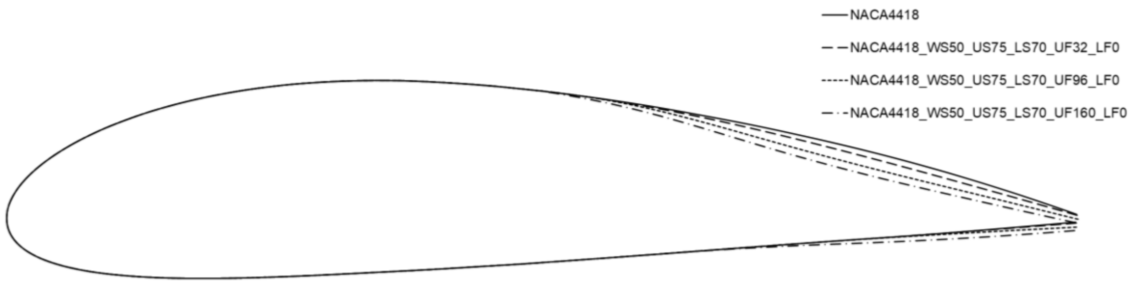

Figure 5.9 – Airfoil geometries obtained for upper surface skin actuation in case study 2.

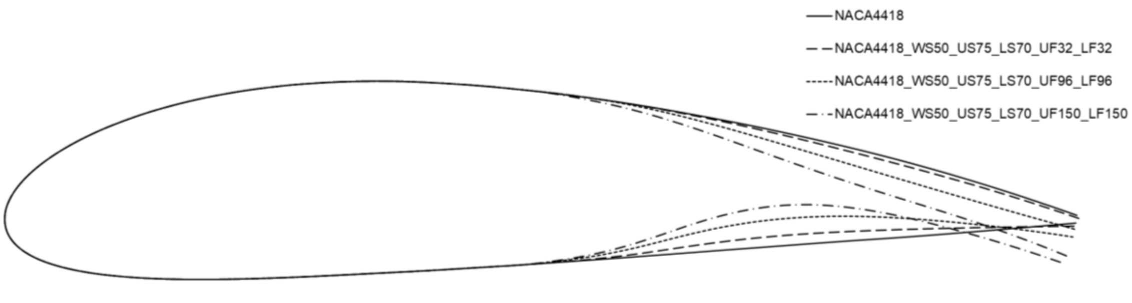

Figure 5.10 – Airfoil geometries obtained for upper and lower surface skins actuation in case study 2.

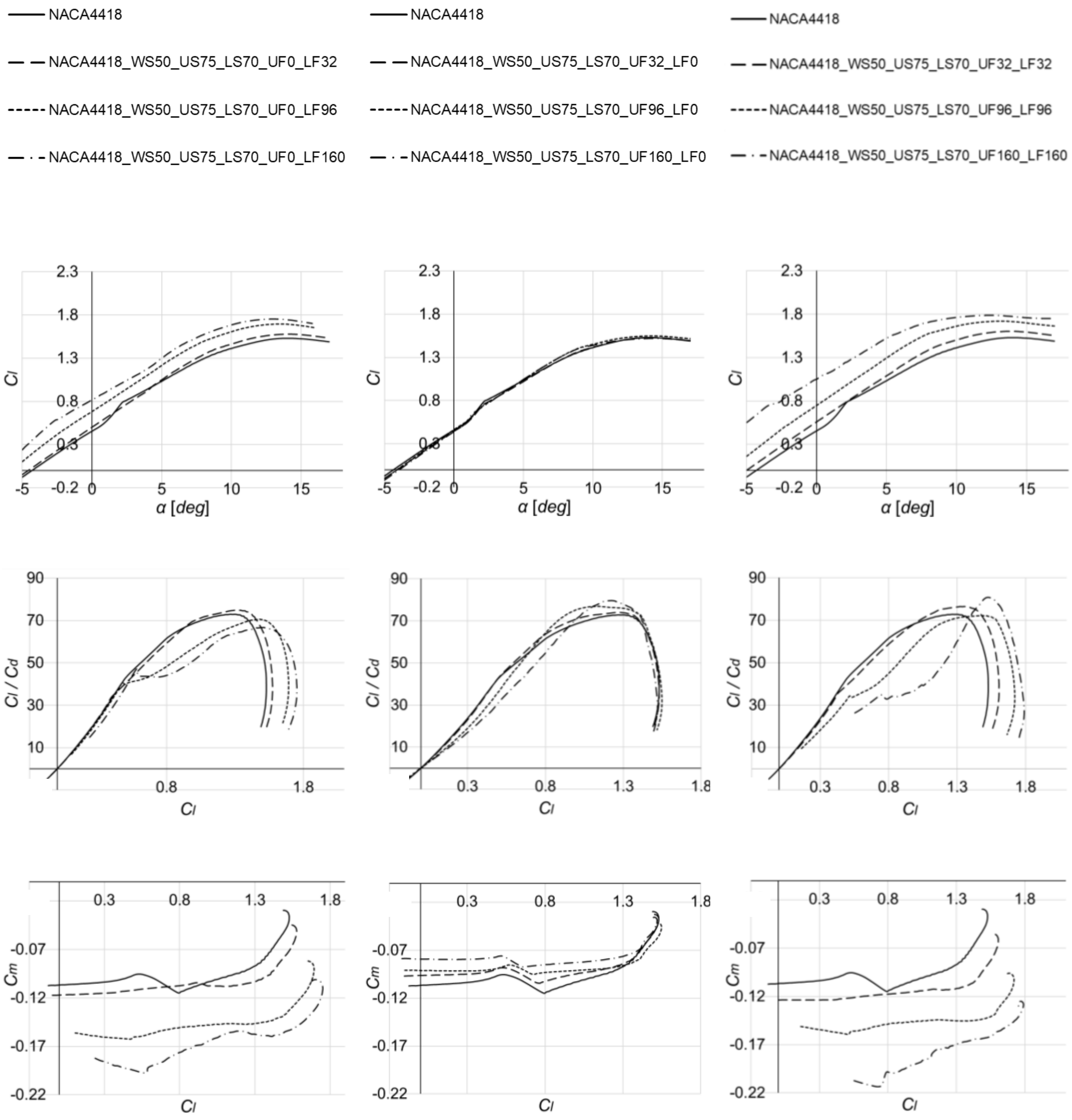

Figure 5.11 – Airfoils aerodynamic performance metrics for case study 2 and $Re = 250 \times 10^3$.

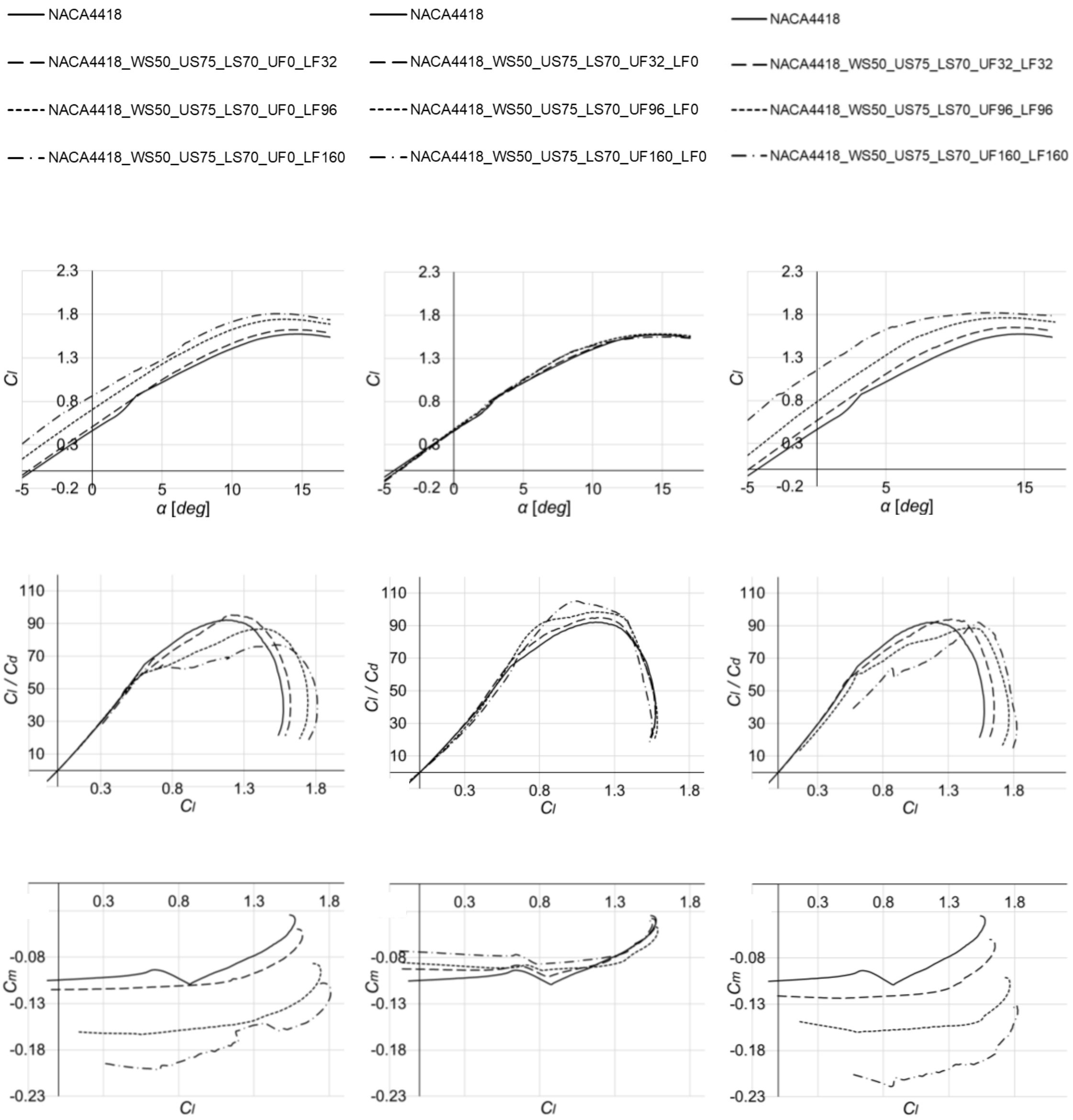

Figure 5.12 – Airfoils aerodynamic performance metrics for case study 2 and $Re = 500 \times 10^3$.

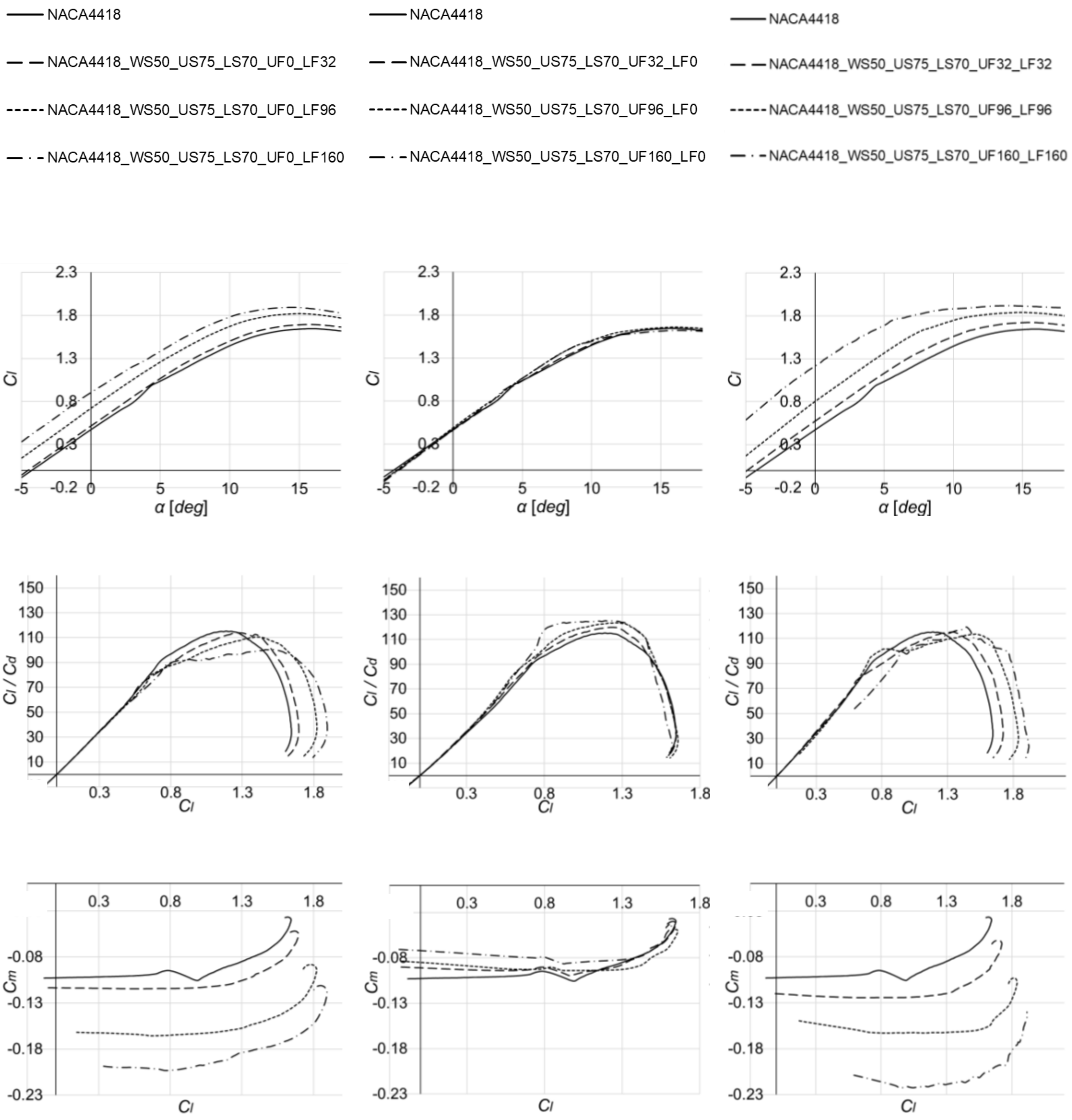

Figure 5.13 – Airfoils aerodynamic performance metrics for case study 2 and $Re = 1 \times 10^6$.

Case Study 3

Regarding the third case study, *Figures 5.14* to *5.16* show the resulting airfoil geometries for lower skin actuation only, upper skin actuation only, and both skins actuation, respectively. *Figure 5.17* presents its aerodynamic metric curves.

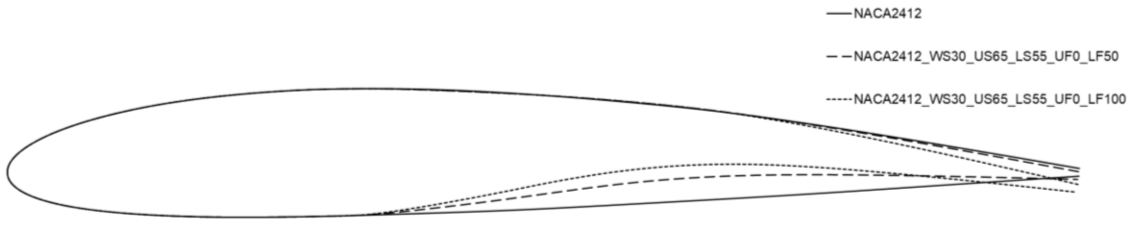

Figure 5.14 – Airfoil geometries obtained for lower surface skin actuation in case study 3.

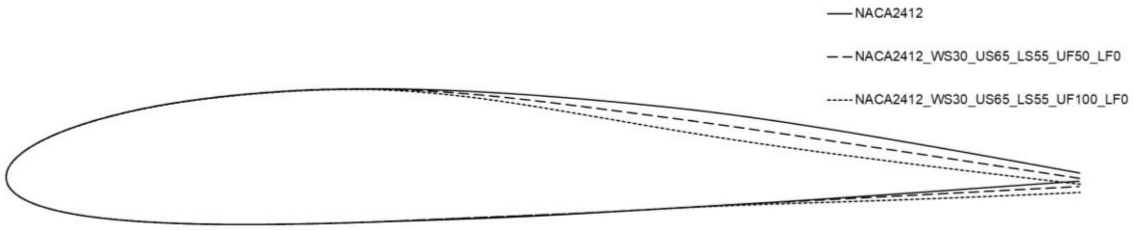

Figure 5.15 – Airfoil geometries obtained for upper surface skin actuation in case study 3.

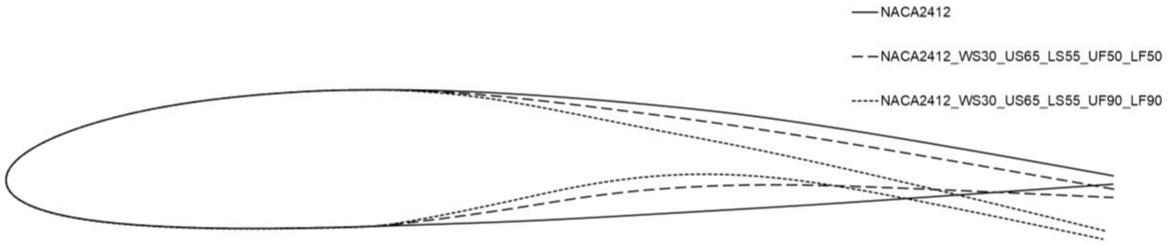

Figure 5.16 – Airfoil geometries obtained for upper and lower surface skins actuation in case study 3.

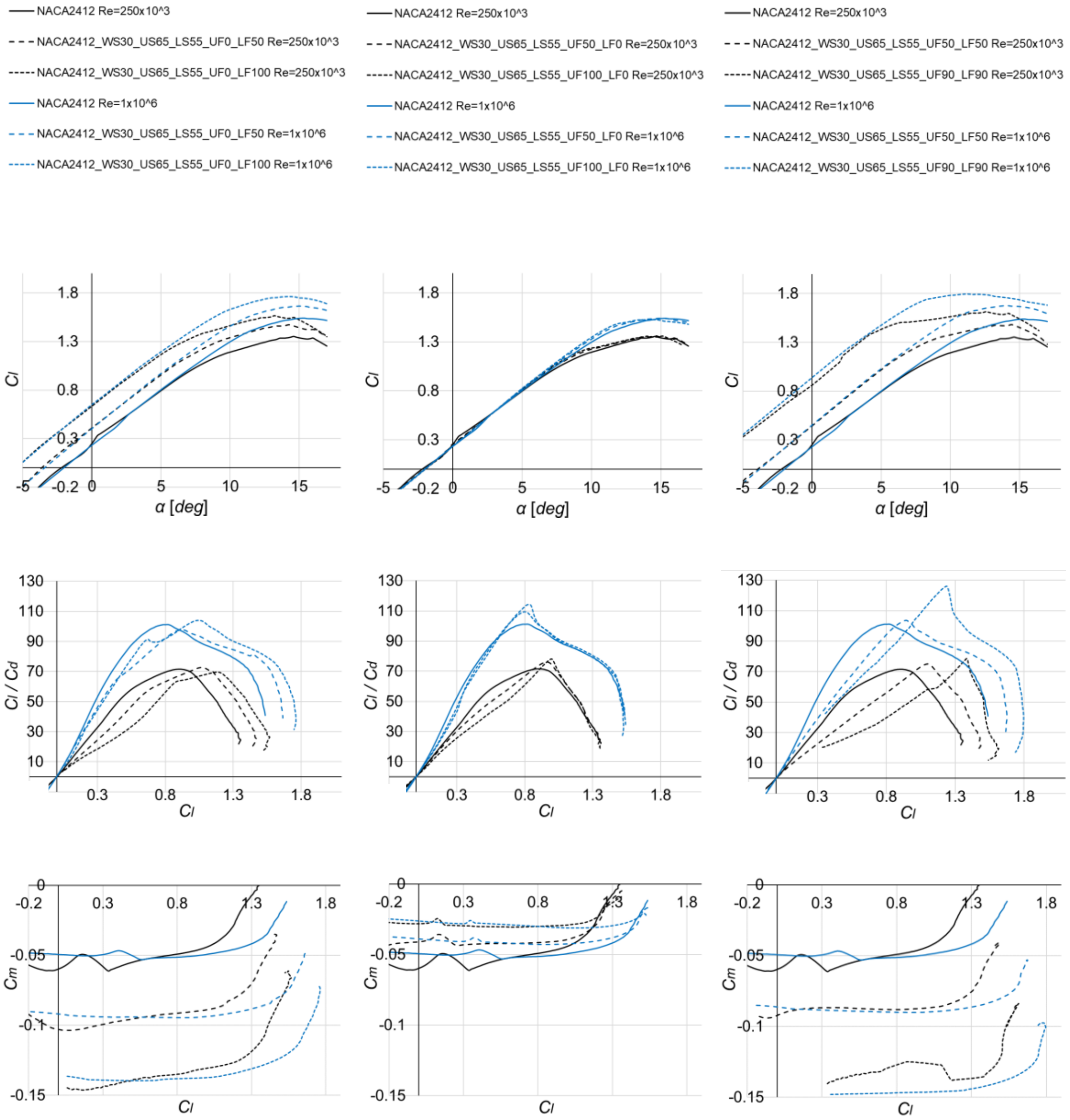

Figure 5.17 – Airfoils aerodynamic performance metrics for case study 3.

Case Study 4

Regarding the fourth case study, *Figures 5.18* to *5.20* show the resulting airfoil geometries for lower skin actuation only, upper skin actuation only, and both skins actuation, respectively. *Figure 5.21* presents its aerodynamic metric curves.

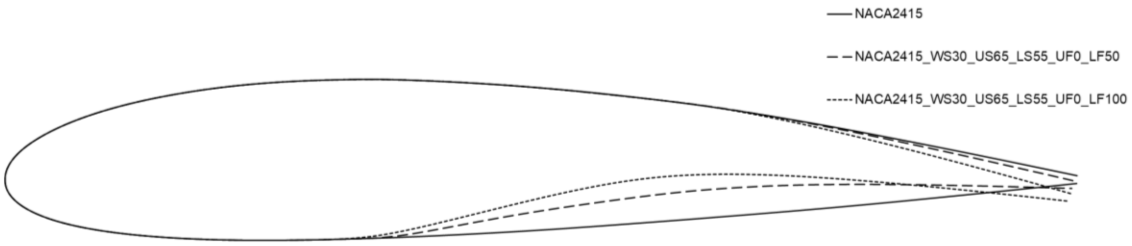

Figure 5.18 – Airfoil geometries obtained for lower surface skin actuation in case study 4.

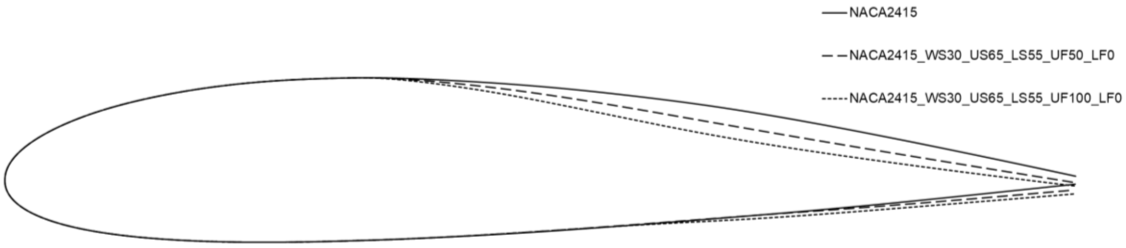

Figure 5.19 – Airfoil geometries obtained for upper surface skin actuation in case study 4.

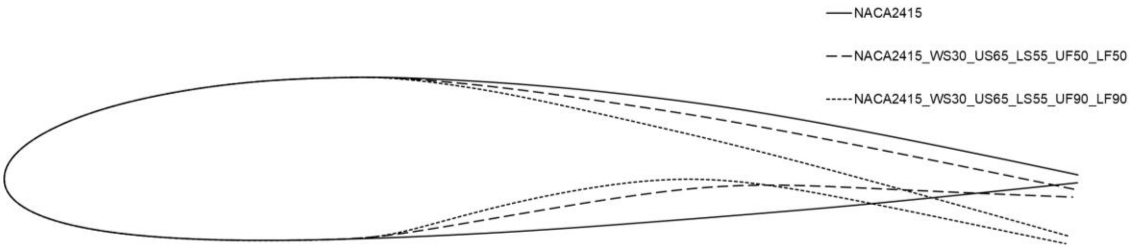

Figure 5.20 – Airfoil geometries obtained for upper and lower surface skins actuation in case study 4.

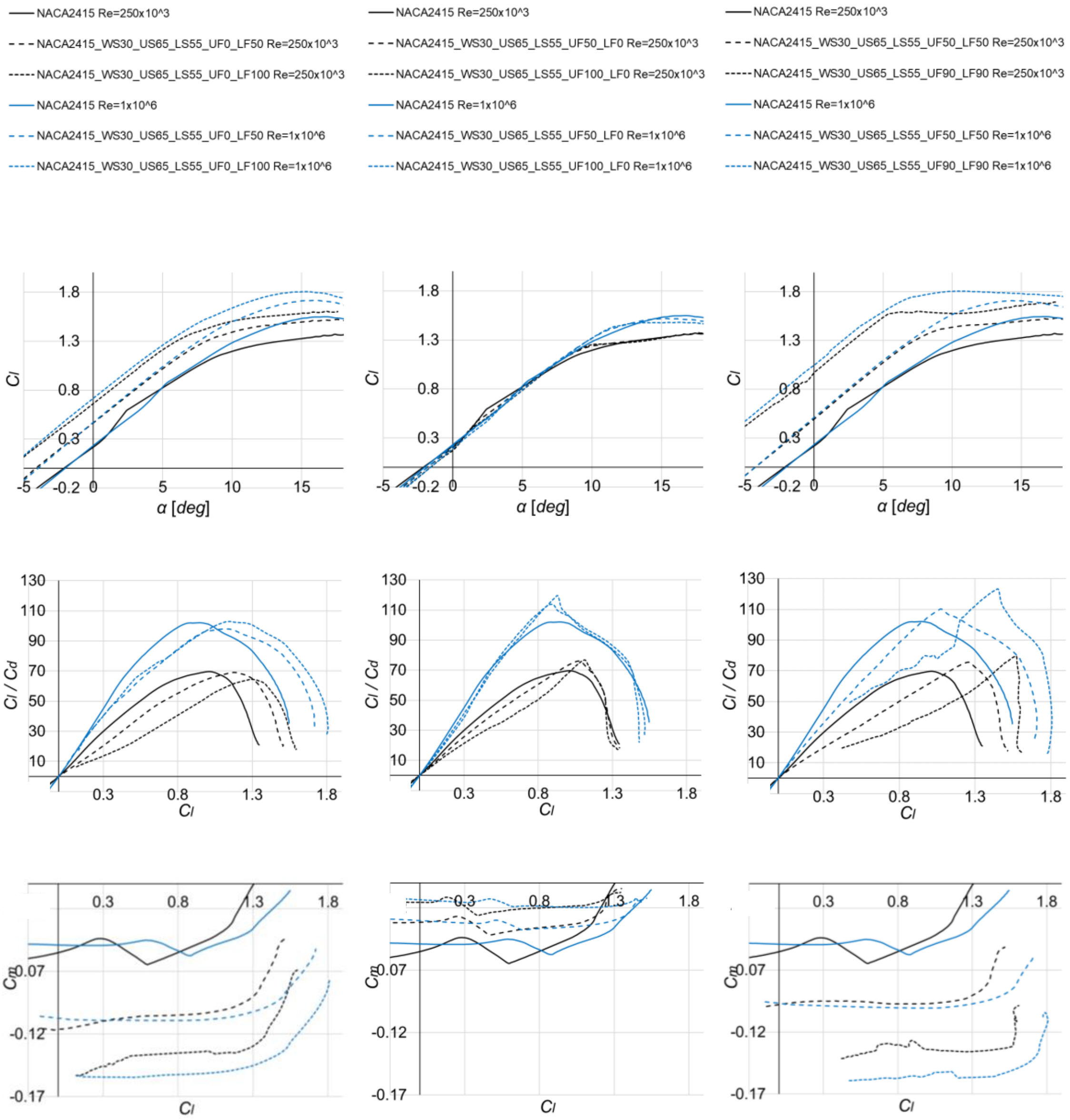

Figure 5.21 – Airfoils aerodynamic performance metrics for case study 4.

Conventional Hinged Surfaces

Regarding the CHSs, *Table 5.2* presents the deflections required to match the trailing-edge perpendicular-to-chord displacement value relative to the airfoil's chord and an equal increase in lift coefficient at zero angle-of-attack of the morphing case study "1", with maximum applied distributed forces on both stringers.

Table 5.2 – Conventional hinged surface equivalent deflections values.

Case	**Equivalent $\Delta C_{l,\alpha_0}$**			**Equivalent d_{TE}**		
		$\delta_{HS}\ [deg]$			$\delta_{HS}\ [deg]$	
$\boldsymbol{Re}$	$\Delta C_{l,\alpha_0}$	$c_{HS} = 15.0\%$	$c_{HS} = 30.0\%$	d_{TE} [%]	$c_{HS} = 15.0\%$	$c_{HS} = 30.0\%$
$\mathbf{250 \times 10^3}$	0.88	33.0	23.0	7.7	30.0	14.0
$\mathbf{500 \times 10^3}$	0.96	37.0	26.0			
$\mathbf{1 \times 10^6}$	1.00	37.0	27.0			

Figures 5.22 and *5.23* illustrate the airfoils with the obtained equivalent CHS deflections, corresponding to chord ratios of 15.0 % and 30.0 %, respectively. The naming convention for these airfoils follows the template: “OriginalAirfoil_SC_DA”, where the designation starts with the original airfoil’s name, followed by the CHS chord ratio (SC) and its deflection angle (DA) in degrees.

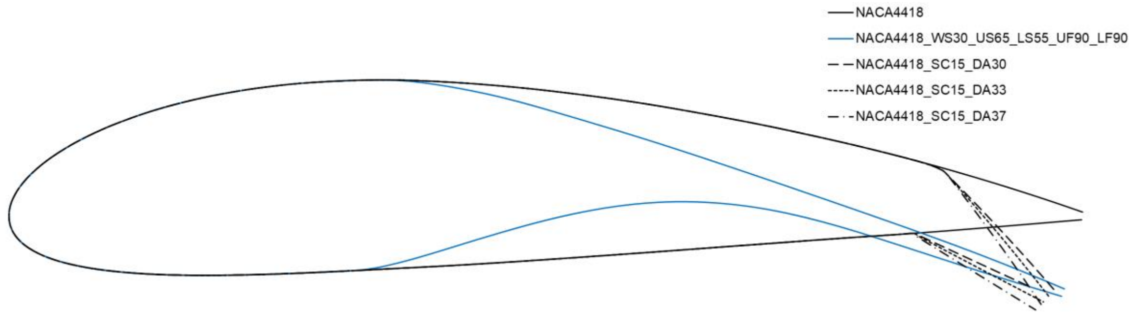

Figure 5.22 – Airfoil geometries of 15.0 % chord ratio conventional hinged surfaces case study.

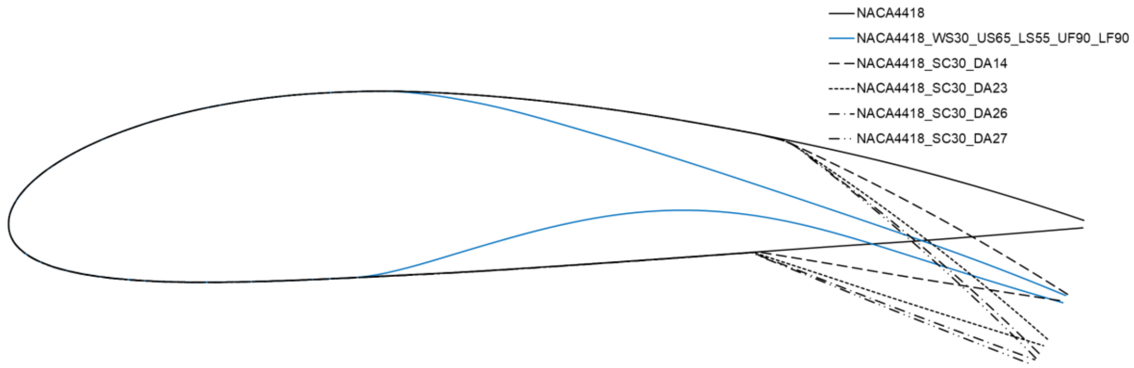

Figure 5.23 – Airfoil geometries of 30.0 % chord ratio conventional hinged surfaces case study.

Figure 5.24 presents the analysed aerodynamic coefficients, comparing both the CHS cases and the morphing airfoil.

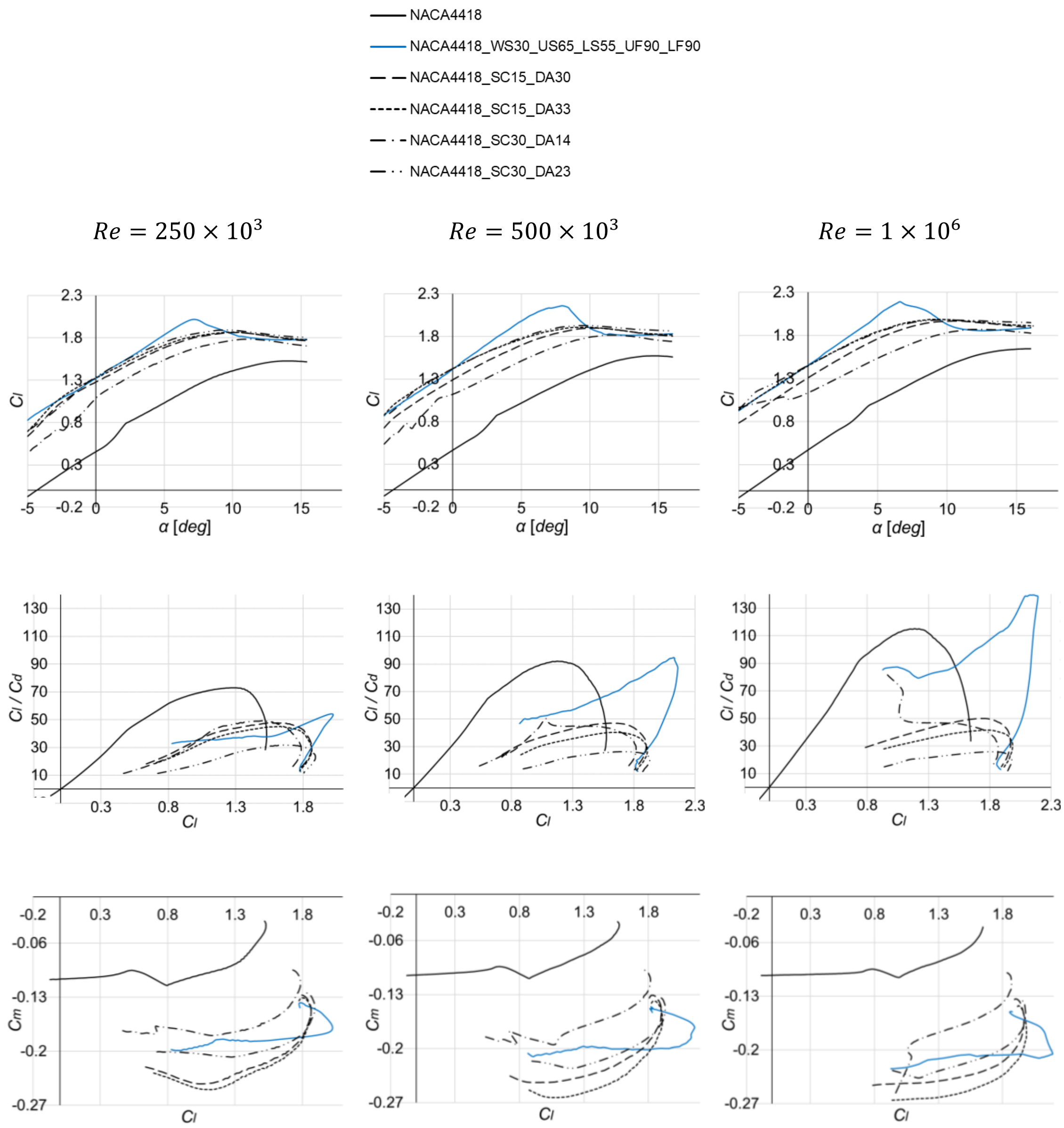

Figure 5.24 – Airfoils aerodynamic performance metrics for conventional hinged surfaces case study.

Finally, *Table 5.3* summarizes the maximum values of the lift coefficient, lift-to-drag ratio, and the corresponding pitching moment coefficient for the maximum lift-to-drag ratio for the “NACA 4418” airfoil. Additionally, *Table 5.4* provides a comparative analysis of these parameters between the morphing airfoil and the CHS cases (selecting the scenario that maximizes each parameter), along with the relative increase or decrease (in absolute value) compared to the values obtained for the “NACA 4418” airfoil.

Table 5.3 – "NACA 4418" aerodynamic performance metrics values.

		NACA 4418	
$\boldsymbol{Re}$	250×10^3	500×10^3	1×10^6
$\boldsymbol{(C_l/C_d)_{max}}$	72.8	92.1	115.2
$\boldsymbol{C_{l_{max}}}$	1.53	1.57	1.64
$\boldsymbol{C_{m_{(C_l/C_d)_{max}}}}$	−0.0875	−0.0880	−0.0912

Table 5.4 – Comparison of the aerodynamic performance metrics values between the morphing and conventional hinged surfaces cases.

		Morphing			**Conventional Hinged Surface**	
$\boldsymbol{Re}$	250×10^3	500×10^3	1×10^6	250×10^3	500×10^3	1×10^6
$\boldsymbol{C_{l_{max}}}$	2.00 (+30.7 %)	2.16 (+37.6 %)	2.19 (+33.5 %)	1.89 (+23.5 %)	1.93 (+22.9 %)	1.99 (+21.3 %)
$\boldsymbol{\left(\frac{C_l}{C_d}\right)_{max}}$	54.0 (−25.8 %)	94.6 (+2.7 %)	139.7 (+21.3 %)	49.5 (−32.0 %)	50.4 (−45.3 %)	81.5 (−29.3 %)
$\boldsymbol{C_{m_{\left(\frac{C_l}{C_d}\right)_{max}}}}$	−0.1748 (+99.8 %)	−0.1855 (+110.8)	−0.2073 (+127.3 %)	−0.1636 (+87.0 %)	−0.1948 (+121.4 %)	−0.2561 (+180.8 %)

The safety margin analysis for case study “1”, with the maximum distributed forces applied to both stringers, as shown in *Figure 5.7*, revealed positive safety margins, demonstrating that the skin material did not reach its maximum stress limits. Furthermore, the minimum safety margin value obtained for the skin finite elements was 1.84, indicating that stresses experienced were approximately three times lower than the maximum allowable stress.

The three analysed airfoils – “NACA 2412”, “NACA 2415”, and “NACA 2418” – exhibited similar behaviour in their aerodynamic metrics when subjected to morphing actuation. While the actuation of the lower surface skin increases the airfoil’s camber, increasing the maximum lift coefficient and the pitching moment coefficient (in absolute value), the actuation of the upper surface skin decreases the airfoil’s thickness from the wing spar to the trailing-edge, increasing the maximum lift-to-drag ratio while maintaining the lift coefficient approximately constant, and enhancing lift-to-drag ratio over a significant range of intermediate lift coefficients, while also reducing the pitching moment coefficient within that range. The simultaneous actuation of both skins results in an increase not only in the maximum lift coefficient but also in lift-to-drag ratio across a range of higher lift coefficients, combining both effects.

It is important to note that these effects are more pronounced in the airfoil with the greater maximum relative thickness, as the morphing in this case is able to achieve larger relative increases in both the maximum lift coefficients and the maximum lift-to-drag ratios. For example, the "NACA 4418" airfoil achieves a 37.6 % increase in the maximum lift coefficient and a 29.0 % increase in the maximum lift-to-drag ratio. In comparison, the "NACA 2415" sees increases of 16.8 % and 20.5 %, while the "NACA 2412" shows gains of 20.1 % and 24.4 % for these metrics, respectively. Furthermore, these effects are generally amplified at higher Reynolds numbers.

A wing spar placed closer to the trailing-edge also limits the increase in both the maximum lift coefficient and the maximum lift-to-drag ratio. However, it has the advantage of maintaining a lift-to-drag ratio very close to its peak over a wider range of lift coefficients, as can be seen in *Figure 5.13*.

Regarding CHSs case study, the results show that the morphing concept achieves a higher maximum lift coefficient and greater maximum lift-to-drag ratio compared to equivalent deflections of CHSs. Additionally, morphing enables a smaller increase (in absolute value) in the pitching moment coefficient relative to most of the studied equivalent CHSs deflections. For example, while the morphing concept achieves a maximum lift coefficient 37.6 % higher than the original airfoil ("NACA 4418"), a CHS achieves a maximum increase of 23.5 %. Furthermore, the morphing concept increases the maximum lift-to-drag ratio by 21.3 % (increasing the corresponding pitching moment coefficient by 127.3 % in absolute terms), while a CHS reduces the maximum lift-to-drag ratio by at least 29.3 % (increasing the corresponding pitching moment coefficient by 180.8 %). Furthermore, as in CHSs case, when the morphing concept increases the maximum lift coefficient, this occurs at lower angles-of-attack compared to the original airfoil.

Chapter 6

Conclusions

The present study aimed to propose and evaluate a new concept of wing morphing suited for application in small-to-medium size UAVs, focusing specifically on the airfoil component. The concept was introduced and detailed, discussing its design variables; a surrogate model was developed to assess which of these variables are most crucial for the aerodynamic performance of the concept and how the key aerodynamic performance metrics are influenced by these variables; case studies were analysed to provide a more comprehensive examination of the aerodynamic performance of the concept; and a prototype was constructed to evaluate the manufacturability of the design and to perform a proof-of-concept.

The proposed airfoil morphing concept aims to address several limitations of current mechanisms: it does not employ elastomer materials in the skin; it is designed to be fail-safe, with the skin thickness engineered to withstand aerodynamic loads; the actuation is executed simply and rapidly, allowing for control of the aircraft in flight; the actuation system also functions as structural elements, as the control rods serve as webs; the morphing amplitude enhances the characteristics of the airfoil obtained by morphing; and the wing surface remains continuous, without gaps or edges.

The results from the surrogate model indicated that the most critical design variables impacting aerodynamic performance are the position of the wing spar and the actuation forces on both upper and lower surfaces skins. Specifically, a more forward position of the wing spar facilitates higher maximum lift coefficients and maximum lift-to-drag ratios. Actuation of the upper surface skin enhances the maximum lift-to-drag ratio of the original airfoil, while the actuation of the lower surface skin increases the maximum lift coefficient. When both skins are actuated simultaneously, their combined effects result in an even greater lift-to-drag ratio at even higher lift coefficients. While the Reynolds number is a variable resulting from the operation of an aircraft, it remains crucial to consider during the aircraft's design phase, as the morphing concept enhances its performance with increasing Reynolds numbers.

Furthermore, the results from the polynomial model revealed simple polynomials for the three analysed aerodynamic performance metrics, with the approximation for the maximum lift coefficient being the most accurate and realistic. Nevertheless, the other two polynomial approximations were also deemed to have strong predictive capabilities. Consequently, the design of the morphing concept can be streamlined by utilizing these approximation polynomials (or similar polynomials for other airfoils). The Kriging model demonstrated similar predictive effectiveness and provided a more realistic prediction for the three aerodynamic performance metrics.

An airfoil with a lower maximum relative thickness achieves benefits to that of a thicker one, but to a lesser extent. Among the analysed airfoils, the “NACA 4418” demonstrated the greatest relative increase in both the maximum lift coefficient (37.6 %) and maximum lift-to-drag ratio (29.0 %). Moreover, the morphing concept showcased superior aerodynamic performance compared to conventional hinged surfaces, such as ailerons or plain flaps, when considering equivalent deflections of these surfaces. Unlike these traditional mechanisms, the proposed morphing concept does not exhibit surface discontinuities, abrupt variations in geometry, skin gaps, or externally mounted components, significantly reducing drag.

The manufacturing of the prototype successfully demonstrated proof-of-concept by effectively achieving morphing in the airfoil component. The results from the experimental wing panel’s actuation closely matched those obtained from the computational model, indicating that the concept can indeed be implemented and simulated with a high degree of accuracy. For instance, the maximum difference recorded for the value of the deflection of the trailing-edge was just 1.6 % relative to the wing panel chord. However, when actuating the upper surface skin, the resulting airfoil geometries exhibited greater discrepancies due to experimental errors, particularly related to the suboptimal functioning of the measurement equipment.

The results obtained in this study suggest that a practical application of the morphing concept in small-to-medium size UAVs could lead to reductions in take-off and landing distances, enable efficient flight at low speeds, optimize performance with varying payloads, increase range and endurance, and lower installed power requirements. However, the most significant aspect of implementing this concept lies in its ability to switch between the original airfoil and the morphed configuration, allowing the aircraft to adapt to different flight conditions. This adaptability is one of the primary objectives of morphing technology, enabling the aircraft to perform multiple missions and enhance its performance across all flight scenarios. These conclusions hold true only if the weight increment resulting from the application of this concept does not adversely affect the UAV's overall performance. Nevertheless, the morphing system's capacity for aircraft control may eliminate the need for additional control systems, thereby reducing the UAV's weight. Furthermore, the concept does not require extra systems, as most UAVs already operate with integrated electrical systems and servomotors.

One of the disadvantages of utilizing this morphing concept would be the reduction in the stall angle-of-attack, which could limit the aircraft's manoeuvrability. Another potential drawback is the use of elastomer materials in the connection between the upper and lower surface skins at the trailing-edge, which may be susceptible to creep. However, the extent of strains experienced is relatively small, and replacement is easy and cost-effective, given that the amount of silicone rubber used is minimal. Nonetheless, alternative types of connections could be employed at the junction of the skins, such as a hinged mechanism. However, this approach might introduce additional drag and negatively impact the aerodynamic performance of the morphing concept.

It is also important to note that while the aerodynamic performance benefits of implementing the morphing concept would be relatively smaller in airfoils with lower maximum relative thicknesses, the integration of this concept into such airfoils would also pose greater challenges. This is primarily due to the limited space available for the placement of servomotors or other actuation systems, which can complicate the design and implementation process.

In conclusion, it can be stated that the implementation of the proposed morphing concept could serve as an effective solution for small-to-medium size cargo transport UAVs, especially in urban environments, provided that its operation is proven to be safe. This approach could reduce energy consumption and operational costs during flight and enable the UAV to operate efficiently under varying weight conditions.

6.1 Future Perspectives

The present work introduced a novel concept of wing morphing, highlighting its potential benefits and conducting a proof-of-concept. However, further research is necessary to truly validate the practical implementation of this concept. Therefore, the following future work on this topic is proposed:

- **Investigation of the application of the morphing concept to other airfoils**: explore the application of the morphing concept to different airfoil designs, assessing the resulting aerodynamic characteristics and performance metrics. This research could reveal how variations in airfoil characteristics influence the effectiveness of morphing.

- **Design of a wing with implemented morphing concept**: develop a comprehensive wing design that incorporates the morphing concept, including the sizing of skin thickness and determining the number of actuators needed for effective morphing. Wind tunnel testing should be conducted to assess skin displacements under aerodynamic loads and validate the design choices.
- **Practical application in a UAV and flight testing**: propose the practical implementation of the morphing concept in a UAV, followed by flight testing to validate the aerodynamic benefits predicted through computational models. This phase will help uncover the actual advantages and limitations of the concept in real-world applications, providing critical insights for future development.

These future research directions will contribute to a deeper understanding and refinement of the proposed wing morphing concept, potentially leading to significant advancements in UAV technology and performance.

References

[1] S. Barbarino, O. Bilgen, R. M. Ajaj, M. I. Friswell, and D. J. Inman, "A review of morphing aircraft," *Journal of Intelligent Material Systems and Structures,* vol. 22, no. 9, pp. 823-877, 2011.

[2] A. Sofla, S. Meguid, K. Tan, and W. Yeo, "Shape morphing of aircraft wing: status and challenges," *Materials & Design,* vol. 31, no. 3, pp. 1284-1292, 2010.

[3] V. L. Hattalli and S. R. Srivatsa, "Wing morphing to improve control performance of an aircraft-an overview and a case study," *Materials Today: Proceedings,* vol. 5, no. 10, pp. 21442-21451, 2018.

[4] C. Thill, J. Etches, I. Bond, K. Potter, and P. Weaver, "Morphing skins," *The Aeronautical Journal,* vol. 112, no. 1129, pp. 117-139, 2008.

[5] I. Dimino, L. Lecce, and R. Pecora, *Morphing wing technologies: large commercial aircraft and civil helicopters*. Butterworth-Heinemann, 2017.

[6] J. Sun, Q. Guan, Y. Liu, and J. Leng, "Morphing aircraft based on smart materials and structures: a state-of-the-art review," *Journal of Intelligent Material Systems and Structures,* vol. 27, no. 17, pp. 2289-2312, 2016.

[7] T. Majid and B. W. Jo, "Status and challenges on design and implementation of camber morphing mechanisms," *International Journal of Aerospace Engineering,* vol. 2021, no. 1, p. 6399937, 2021.

[8] A. W. Terrence, "Morphing Aircraft Technology – New Shapes for Aircraft Design," *Multifunctional Structures / Integration of Sensors and Antennas,* pp. 1-20, 2006.

[9] S. Joshi, Z. Tidwell, W. Crossley, and S. Ramakrishnan, "Comparison of morphing wing stategies based upon aircraft performance impacts," in *45th AIAA/ASME/ASCE/AHS/ASC Structures, Structural Synamics & Materials Conference*, Palm Springs, California, 2004, p. 1722.

[10] R. M. Ajaj, C. S. Beaverstock, and M. I. Friswell, "Morphing aircraft: the need for a new design philosophy," *Aerospace Science and Technology,* vol. 49, pp. 154-166, 2016.

[11] K. K. Aminjan *et al.*, "Numerical and experimental investigation to design a novel morphing airfoil for performance optimization," *Propulsion and Power Research,* vol. 12, no. 1, pp. 83-103, 2023.

[12] M. S. Parancheerivilakkathil, J. S. Pilakkadan, M. AMOOZGAR, D. ASADI, Y. ZWEIRI, and M. I. FRISWELL, "A review of control strategies used for morphing aircraft applications," *Chinese Journal of Aeronautics,* 2024.

[13] C. Lingling, L. Qi, G. Feng, D. Xintian, H. Yuqing, and D. Yangchen, "Design, modeling, and control of morphing aircraft: a review," *Chinese Journal of Aeronautics,* vol. 35, no. 5, pp. 220-246, 2022.

[14] I. Kovalev, A. Voroshilova, and M. Karaseva, "Analysis of the current situation and development trend of the international cargo UAVs market," in *Journal of Physics: Conference Series*, 2019, vol. 1399, no. 5, p. 055095: IOP Publishing.

[15] J. Rauleder, B. Van Der Wall, A. Abdelmoula, D. Komp, and S. Kumar, "Aerodynamic performance of morphing blades and rotor systems.," presented at the 74th Annual American Helicopter Society International Forum and Technology Display 2018, Phoenix, Arizona, USA, 2018.

[16] M. Z. Akhter, A. R. Ali, H. K. Jawahar, F. K. Omar, and E. Elnajjar, "Performance enhancement of small-scale wind turbine featuring morphing blades," *Energy,* vol. 278, p. 127772, 2023.

[17] X. Lachenal, S. Daynes, and P. M. Weaver, "Review of morphing concepts and materials for wind turbine blade applications," *Wind Energy,* vol. 16, no. 2, pp. 283-307, 2013.

[18] D. Inman, "Wings: out of the box. Determining actuator requirements for controlled morphing air vehicles aerodynamic loads," in *DARPA Technology Interchange Meeting*, Wright Patterson Air Force Base, Dayton, OH, 2001.

[19] J. Bowman, B. Sanders, B. Cannon, J. Kudva, S. Joshi, and T. Weisshaar, "Development of next generation morphing aircraft structures," in *48th AIAA/ASME/ASCE/AHS/ASC Structures, Structural Dynamics, and Materials Conference,* Honolulu, Hawaii, 2007, p. 1730.

[20] M. Secanell, A. Suleman, and P. Gamboa, "Design of a morphing airfoil using aerodynamic shape optimization," *AIAA journal,* vol. 44, no. 7, pp. 1550-1562, 2006.

[21] T. Majid and B. W. Jo, "Comparative aerodynamic performance analysis of camber morphing and conventional airfoils," *Applied Sciences,* vol. 11, no. 22, p. 10663, 2021.

[22] B. W. Jo and T. Majid, "Enhanced range and endurance evaluation of a camber morphing wing aircraft," *Biomimetics,* vol. 8, no. 1, p. 34, 2023.

[23] J. M. Weaver-Rosen, P. B. Leal, D. J. Hartl, and R. J. Malak Jr, "Parametric optimization for morphing structures design: application to morphing wings adapting to changing flight conditions," *Structural and Multidisciplinary Optimization,* vol. 62, no. 6, pp. 2995-3007, 2020.

[24] J. W. Smith, *Variable-camber systems integration and operational performance of the AFTI/F-111 mission adaptive wing*. National Aeronautics and Space Administration, Office of Management, 1992.

[25] A. Holle, "Plane and the like for aeroplanes," *United States Patent,* no. 1225711, 1923.

[26] Boeing, "Variable camber wing," in "Second Progress Report," 1973.

[27] R. Brissenden, A. Heath, D. Conner, and M. Spearman, "Assessment of variable camber for application to transport aircraft," Boeing Commercial Airplane Company, Contractor Report 1980.

[28] F. Austin, M. J. Rossi, W. Van Nostrand, G. Knowles, and A. Jameson, "Static shape control for adaptive wings," *AIAA Journal,* vol. 32, no. 9, pp. 1895-1901, 1994.

[29] J. J. Joo and B. Sanders, "Optimal location of distributed actuators within an in-plane multi-cell morphing mechanism," *Journal of Intelligent Material Systems and Structures,* vol. 20, no. 4, pp. 481-492, 2009.

[30] S. Barbarino, W. G. Dettmer, and M. I. Friswell, "Morphing trailing edges with shape memory alloy rods," in *21st International Conference on Adaptive Structures and Technologies (ICAST)*, University Park, Pennsylvania, 2010.

[31] L. Yang, Z. Ou, and G. Jiang, "Research progress of elastomer materials and application of elastomers in drilling fluid," *Polymers,* vol. 15, no. 4, p. 918, 2023.

[32] J. D. Bartley-Cho, D. P. Wang, C. A. Martin, J. N. Kudva, and M. N. West, "Development of high-rate, adaptive trailing edge control surface for the smart wing phase 2 wind tunnel model," *Journal of Intelligent Material Systems and Structures,* vol. 15, no. 4, pp. 279-291, 2004.

[33] D. Cadogan, T. Smith, F. Uhelsky, and M. Mackusick, "Morphing inflatable wing development for compact package unmanned aerial vehicles," in *45th AIAA/ASME/ASCE/AHS/ASC Structures, Structural Dynamics & Materials Conference*, Palm Springs, California, 2004, p. 1807.

[34] R. Vos and R. Barrett, "Mechanics of pressure-adaptive honeycomb and its application to wing morphing," *Smart Materials and Structures,* vol. 20, no. 9, p. 094010, 2011.

[35] N. Feng, L. Liu, Y. Liu, and J. Leng, "A bio-inspired, active morphing skin for camber morphing structures," *Smart Materials and Structures,* vol. 24, no. 3, p. 035023, 2015.

[36] J. Cooper, "Adaptive stiffness structures for air vehicle drag reduction," *Multifunctional Structures/Integration of Sensors and Antennas,* p. 15, 2006.

[37] S. M. Lim, S. Lee, H. C. Park, K. J. Yoon, and N. S. Goo, "Design and demonstration of a biomimetic wing section using a lightweight piezo-composite actuator (LIPCA)," *Smart Materials and Structures,* vol. 14, no. 4, p. 496, 2005.

[38] R. Barrett, R. McMurtry, R. Vos, P. Tiso, and R. De Breuker, "Post-buckled precompressed (PBP) elements: a new class of flight control actuators enhancing high-speed autonomous VTOL MAVs," in *Smart Structures and Materials 2005: Industrial and Commercial Applications of Smart Structures Technologies*, 2005, vol. 5762, pp. 111-122: SPIE.

[39] R. Paradies and P. Ciresa, "Active wing design with integrated flight control using piezoelectric macro fiber composites," *Smart Materials and Structures,* vol. 18, no. 3, pp. 35-45, 2009.

[40] O. Bilgen *et al.*, "A novel unmanned aircraft with solid-state control surfaces: analysis and flight demonstration," *Journal of Intelligent Material Systems and Structures,* vol. 24, no. 2, pp. 147-167, 2013.

[41] D. Coutu, V. Brailovski, P. Terriault, and C. Fisher, "Experimental validation of the 3D numerical model for an adaptative laminar wing with flexible extrados," presented at the 18th International Conference of Adaptive Structures and Technologies, Ottawa, Ontario, Canada, 2007.

[42] T. Grigorie, R. Botez, and A. Popov, "How the airfoil shape of a morphing wing is actuated and controlled in a smart way," *Journal of Aerospace Engineering,* vol. 28, no. 1, p. 1943, 2015.

[43] C. G. Diaconu, P. M. Weaver, and F. Mattioni, "Concepts for morphing airfoil sections using bi-stable laminated composite structures," *Thin-Walled Structures,* vol. 46, no. 6, pp. 689-701, 2008.

[44] D. Wagg, I. Bond, P. Weaver, and M. Friswell, *Adaptive structures: engineering applications*. John Wiley & Sons, 2008.

[45] L. Shili, G. Wenjie, and L. Shujun, "Optimal design of compliant trailing edge for shape changing," *Chinese Journal of Aeronautics,* vol. 21, no. 2, pp. 187-192, 2008.

[46] Y. Zhang, W. Ge, Z. Zhang, X. Mo, and Y. Zhang, "Design of compliant mechanism-based variable camber morphing wing with nonlinear large deformation," *International Journal of Advanced Robotic Systems,* vol. 16, no. 6, 2019.

[47] P. D. L. Jensen, F. Wang, I. Dimino, and O. Sigmund, "Topology optimization of large-scale 3D morphing wing structures," in *Actuators*, 2021, vol. 10, no. 9, p. 217: MDPI.

[48] L. Campanile and D. Sachau, "The belt-rib concept: a structronic approach to variable camber," *Journal of Intelligent Material Systems and Structures,* vol. 11, no. 3, pp. 215-224, 2000.

[49] L. Campanile, "Modal synthesis of flexible mechanisms for airfoil shape control," *Journal of Intelligent Material Systems and Structures,* vol. 19, no. 7, pp. 779-789, 2008.

[50] B. K. S. Woods and M. I. Friswell, "Preliminary investigation of a fishbone active camber concept," in *ASME 2012 Conference on Smart Materials, Adaptive Structures and Intelligent Systems*, Stone Mountain, Georgia, USA, 2012, vol. 8058, pp. 555-563: American Society of Mechanical Engineers.

[51] B. K. Woods, O. Bilgen, and M. I. Friswell, "Wind tunnel testing of the fish bone active camber morphing concept," *Journal of Intelligent Material Systems and Structures,* vol. 25, no. 7, pp. 772-785, 2014.

[52] B. K. Woods and M. I. Friswell, "Structural characterization of the fish bone active camber morphing airfoil," in *22nd AIAA/ASME/AHS Adaptive Structures Conference*, 2014, p. 1122.

[53] A. E. Rivero, P. M. Weaver, J. E. Cooper, and B. K. Woods, "Parametric structural modelling of fish bone active camber morphing aerofoils," *Journal of Intelligent Material Systems and Structures,* vol. 29, no. 9, pp. 2008-2026, 2018.

[54] A. E. Rivero, P. M. Weaver, J. E. Cooper, and B. K. Woods, "Structural modeling of compliance-based camber morphing structures under transverse shear loading," *AIAA Journal,* vol. 58, no. 11, pp. 4941-4951, 2020.

[55] R. Wu, C. Soutis, S. Zhong, and A. Filippone, "A morphing aerofoil with highly controllable aerodynamic performance," *The Aeronautical Journal,* vol. 121, no. 1235, pp. 54-72, 2017.

[56] S. Meguid, Y. Su, and Y. Wang, "Complete morphing wing design using flexible-rib system," *International Journal of Mechanics and Materials in Design,* vol. 13, pp. 159-171, 2017.

[57] A. Zhao, H. Zou, H. Jin, and D. Wen, "Structural design and verification of an innovative whole adaptive variable camber wing," *Aerospace Science and Technology,* vol. 89, pp. 11-18, 2019.

[58] S. Xiasheng, X. Jingfeng, Z. Jin, W. Zhigang, W. Wenjuan, and M. Zhang, "Design and validation of a variable camber wing structure," *Chinese Journal of Aeronautics,* vol. 37, no. 2, pp. 1-11, 2024.

[59] U. Fasel, D. Keidel, L. Baumann, G. Cavolina, M. Eichenhofer, and P. Ermanni, "Composite additive manufacturing of morphing aerospace structures," *Manufacturing Letters,* vol. 23, pp. 85-88, 2020.

[60] B. Moulton and D. F. Hunsaker, "3D-printed wings with morphing trailing-edge technology," in *AIAA Scitech 2021 Forum*, Virtual Conference, 2021, p. 0351.

[61] S. Jia, Z. Zhang, H. Zhang, C. Song, and C. Yang, "Wind tunnel tests of 3D-printed variable camber morphing wing," *Aerospace,* vol. 9, no. 11, p. 699, 2022.

[62] M. T. Kikuta, "Mechanical properties of candidate materials for morphing wings," Master's Thesis, Virginia Tech University, 2003.

[63] A. C. Ugural, *Stresses in beams, plates, and shells*. CRC Press, 2009.

[64] Ansys. (10/04/2024). *Ansys: engineering simulation software*. Available: https://www.ansys.com/

[65] M. Drela. (15/04/2024). *XFOIL: subsonic airfoil development system*. Available: https://web.mit.edu/drela/Public/web/xfoil/

[66] S. Gudmundsson, *General aviation aircraft design: applied methods and procedures*. Butterworth-Heinemann, 2013.

[67] E. A. Bubert, B. K. Woods, K. Lee, C. S. Kothera, and N. Wereley, "Design and fabrication of a passive 1D morphing aircraft skin," *Journal of Intelligent Material Systems and Structures,* vol. 21, no. 17, pp. 1699-1717, 2010.

[68] R. M. V. Soares, "Design of a variable camber flap for air cargo challenge aircraft," Master's Thesis, Universidade da Beira Interior, 2020.

[69] ASTM, "Standard test methods for flexural properties of unreinforced and reinforced plastics and electrical insulating materials D790," *Annual Book of ASTM Standards,* 1997.

[70] ASTM, "Standard test method for tensile properties of polymer matrix composite materials D3039," *Annual Book of ASTM standards,* 2008.

[71] EasyComposites, "CS25 condensation cure silicone rubber technical datasheet."

[72] A. Hughes and B. Drury, *Electric motors and drives: fundamentals, types and applications*. Newnes, 2019.

[73] A. Forrester, A. Sobester, and A. Keane, *Engineering design via surrogate modelling: a practical guide*. John Wiley & Sons, 2008.

[74] J. R. Martins and A. Ning, *Engineering design optimization*. Cambridge University Press, 2021.

[75] T. Hastie, R. Tibshirani, J. H. Friedman, and J. H. Friedman, *The elements of statistical learning: data mining, inference, and prediction*. Springer, 2009.

[76] M. E. Johnson, L. M. Moore, and D. Ylvisaker, "Minimax and maximin distance designs," *Journal of Statistical Planning and Inference,* vol. 26, no. 2, pp. 131-148, 1990.

[77] M. D. Morris and T. J. Mitchell, "Exploratory designs for computational experiments," *Journal of Statistical Planning and Inference,* vol. 43, no. 3, pp. 381-402, 1995.

[78] MathWorks. (05/06/2024). *MATLAB*. Available: https://www.mathworks.com/

[79] J. D'Errico. (22/07/2024). *Polyfitn MATLAB function*. Available: https://www.mathworks.com/matlabcentral/fileexchange/34765-polyfitn

Appendix A – MATLAB Code

Polynomial Model

```
clear all
clc

% Maximum Likelihood Estimation and Cross Validation - Polynomial
Model
% Main script to prepare data, fit polynomial, and test the model.

% Input:
% X - Matrix with normalized (between 0 and 1) input data
%     with dimensions [m, k], where m is the
%     number of data points and k is the number of design variables.
%     Variables by column: 1- x'_WS, 2- x'_LS, 3- f'_US, 4- f'_LS, 5-
Re'
% Y - Column vector with response data corresponding to X.
%
% Output:
% BestOrder - The best polynomial order determined through cross-vali-
dation.
% Coeff - Coefficients and terms of the fitted polynomial model.
% RMSE - Normalized Root Mean Squared Error on test data.
% r2 - Correlation coefficient on test data.

X = [...];  % Input data matrix (m rows, k columns)
Y = [...];  % Response vector (m rows)

m = 211;  % Total number of data points
k = 5;    % Number of design variables

% Define the proportion of data to use for training
trainRatio = 0.75;  % 75% of the data for training, 25% for testing

% Split the data randomly into training and test sets
idx = randperm(m);              % Random permutation of indices
m_tr = ceil(trainRatio * m);    % Number of training samples

% Training data
XTrain = X(idx(1:m_tr),:);
YTrain = Y(idx(1:m_tr));

% Test data
XTest = X(idx(m_tr+1:end),:);
YTest = Y(idx(m_tr+1:end));

% Call the polynomial fitting function
[BestOrder, Coeff, significantTerms] = polynomial(XTrain, YTrain);

% Display the final model
fprintf('\nFinal model coefficients and terms:\n');
for i = 1:length(significantTerms)
    % Construct the term string
    termString = '';
```

```
    for varIndex = 1:k
        if Coeff.ModelTerms(significantTerms(i), varIndex) > 0
            termString = [termString sprintf('x%d^%d ', varIndex, Coeff.ModelTerms(significantTerms(i), varIndex))];
        end
    end
    fprintf('Coefficient: %.5f, Term: %s\n', Coeff.Coefficients(significantTerms(i)), strtrim(termString));
end

% Test the model with the test data
[RMSE, r2] = test_model(Coeff, XTest, YTest);

% Display the evaluation metrics
fprintf('\nModel evaluation:\n');
fprintf('Root Mean Squared Error (normalized): %.4f\n', RMSE);
fprintf('r^2 (correlation coefficient): %.4f\n', r2);

% Determine if the model has good predictive capabilities
if r2 > 0.8 && RMSE < 0.1
    fprintf('\nThe model has good predictive capabilities and is well-saturated with data.\n');
else
    fprintf('\nThe model needs more data to improve its predictive capabilities.\n');
end




%% Function: polynomial
function [BestOrder, Coeff, significantTerms] = polynomial(XTrain, YTrain)
    % Fits a multivariable polynomial to training data using cross-validation.
    %
    % Inputs:
    % XTrain - Matrix of training data (normalized, each column is a variable).
    % YTrain - Vector of training responses.
    %
    % Outputs:
    % BestOrder - The polynomial order selected using cross-validation.
    % Coeff - Structure containing the polynomial coefficients and terms.
    % significantTerms - Indices of the significant terms in the final model.

    q_f = 10;         % Number of cross-validation folds, q_f = 5 or 10
    MaxOrder = 4;     % Maximum polynomial order to consider

    % Initialize cross-validation error storage
    CrossVal = zeros(1, MaxOrder);
    m_tr = length(YTrain);           % Number of training samples

    % Loop through possible polynomial orders
    for Order = 1:MaxOrder
        CrossVal(Order) = 0;
```

```
        % Split training data into q subsets
        XS = randperm(m_tr);
        FullXS = XS;
        From = (1:round(m_tr/q_f):m_tr-1);
        To = zeros(size(From));
        for i = 1:q_f-1
            To(i) = From(i+1) - 1;
        end
        To(q_f) = m_tr;

        % Cross-validation loop
        for j = 1:q_f
            Removed = XS(From(j):To(j));
            XS(From(j):To(j)) = [];

            % Fit polynomial to remaining data
            P = polyfitn(XTrain(XS,:), YTrain(XS), Order);

            % Predict on removed data
            yPred = polyvaln(P, XTrain(Removed,:));
            CrossVal(Order) = CrossVal(Order) + sum((YTrain(Removed) -
yPred).^2) / length(Removed);

            % Restore full XS set for next iteration
            XS = FullXS;
        end
    end

    % Find the best order with the minimum cross-validation error
    [~, BestOrder] = min(CrossVal);
    fprintf('The polynomial order that minimizes the generalized error
is %d\n', BestOrder);

    % Fit the final model with the best order on all training data
    Coeff = polyfitn(XTrain, YTrain, BestOrder);

    % Iterative refinement process with threshold
    threshold = 0;  % Initial threshold
    proceed = true;  % Control loop
    significantTerms = 1:length(Coeff.Coefficients);  % All terms ini-
tially

    while proceed
        % Display coefficients and terms in descending order
        [sortedCoeffs, sortIdx] = sort(abs(Coeff.Coefficients),
'descend');
        sortedTerms = Coeff.ModelTerms(sortIdx, :);
        fprintf('\nOriginal coefficients and corresponding terms:\n');
        for i = 1:length(sortedCoeffs)
            fprintf('Coefficient: %.5f\n', sortedCoeffs(i));
        end

        % Ask user for a new threshold
        threshold = input(sprintf('Enter the threshold value to filter
insignificant terms (previous: %.5f): ', threshold));

        % Identify significant terms based on the threshold
        significantTerms = find(abs(Coeff.Coefficients) >= threshold);
```

```
        % If no significant terms are found, retry
        if isempty(significantTerms)
            fprintf('No significant terms found with threshold %.5f.
Please try a lower value.\n', threshold);
            continue;
        end

        % Create a new reduced model with significant terms
        reducedModelTerms = Coeff.ModelTerms(significantTerms, :);

        % Recalculate coefficients with significant terms
        Coeff = polyfitn(XTrain, YTrain, reducedModelTerms);

        % Ask user if they want to continue
        proceed = input('Do you want to apply a new threshold? Enter 1
for Yes, 0 for No: ');
    end
end




%% Function: test_model
function [RMSE, r2] = test_model(Coeff, XTest, YTest)
    % Evaluates the polynomial model on the test data.
    %
    % Inputs:
    % Coeff - Structure containing the polynomial coefficients and
terms.
    % XTest - Matrix of test data.
    % YTest - Vector of true responses corresponding to XTest.
    %
    % Outputs:
    % RMSE - Normalized Root Mean Squared Error.
    % r2 - Correlation coefficient (r^2).

    % Predict Y values using the polynomial model
    YPred = polyvaln(Coeff, XTest);

    % Calculate the Root Mean Squared Error (RMSE)
    RMSE = sqrt(mean((YTest - YPred).^2));

    % Normalize RMSE by the range of YTest
    rangeY = max(YTest) - min(YTest);
    RMSE = RMSE / rangeY;

    % Calculate the correlation coefficient (r^2)
    m_te = length(YTest);
    Numerator = m_te * sum(YTest .* YPred) - sum(YTest) * sum(YPred);
    Denominator = sqrt((m_te * sum(YTest.^2) - sum(YTest)^2) * (m_te *
sum(YPred.^2) - sum(YPred)^2));
    r2 = (Numerator / Denominator)^2;
end
```

Kriging Model

```
clear all
clc

% Kriging Model and Cross Validation
% Main script to prepare data, fit the model, and test the model.

% Input:
% X - Matrix with normalized (between 0 and 1) input data
%     with dimensions [m, k], where m is the
%     number of data points and k is the number of design variables.
%     Variables by column: 1- x'_WS, 2- x'_LS, 3- f'_US, 4- f'_LS, 5-
Re'
% Y - Column vector with response data corresponding to X.
%
% Output:
% RMSE - Normalized Root Mean Squared Error on test data.
% r2 - Correlation coefficient on test data.

global ModelInfo

X = [...];  % Input data matrix (m rows, k columns)
Y = [...];  % Response vector (m rows)

m = 211;  % Total number of data points
k = 5;    % Number of design variables

% Set upper and lower bounds for search of log(theta)
UpperTheta = ones(1, k) * 2;   % Upper bound
LowerTheta = ones(1, k) * -3;  % Lower bound

% Define the proportion of data to use for training
trainRatio = 0.75;  % 75% of the data for training, 25% for testing

% Split the data randomly into training and test sets
idx = randperm(m);              % Random permutation of indices
m_tr = ceil(trainRatio * m);    % Number of training samples

% Training data
XTrain = X(idx(1:m_tr),:);
YTrain = Y(idx(1:m_tr));

% Test data
XTest = X(idx(m_tr+1:end),:);
YTest = Y(idx(m_tr+1:end));

% Store training data in the global ModelInfo structure
ModelInfo.X = XTrain;
ModelInfo.Y = YTrain;

% Run Genetic Algorithm (GA) to optimize likelihood for training data
[ModelInfo.Theta, MinNegLnLike] = ga(@likelihood, k, [], [], [], [],
LowerTheta, UpperTheta);

% Store Cholesky factorization of Psi in ModelInfo
[NegLnLike, ModelInfo.Psi, ModelInfo.U] = likelihood(ModelInfo.Theta);
```

```
% Display theta values (importance of each variable)
fprintf('Theta values for each variable (x1 to x5):\n');
for i = 1:k
    fprintf('x%d: %f\n', i, 10.^ModelInfo.Theta(i));
end

% Select the three most important variables based on largest theta
values
[~, sortedIdx] = sort(ModelInfo.Theta, 'descend');
topVariables = sortedIdx(1:3); % Indices of the top three variables

fprintf('\nThe three most important variables based on theta are:\n');
for i = 1:3
    fprintf('x%d with theta = %f\n', topVariables(i), 10.^Model-
Info.Theta(topVariables(i)));
end

% Call the sensitivity analysis function
num_points = 100; % Number of points for gradient calculation along
var3
h = 0.001;          % Small step size for central difference
fixed_var4 = 0.5;   % Fixed value for variable 4
fixed_var5 = 0.5;   % Fixed value for variable 5
analyze_sensitivity(ModelInfo, num_points, h, fixed_var4, fixed_var5,
sortedIdx);

% Test the model performance using RMSE and r^2
[RMSE, r2] = test_model(ModelInfo, XTest, YTest);

% Display the evaluation metrics
fprintf('\nModel evaluation:\n');
fprintf('Root Mean Squared Error (normalized): %.4f\n', RMSE);
fprintf('r^2 (correlation coefficient): %.4f\n', r2);

% Determine if the model has good predictive capabilities
if r2 > 0.8 && RMSE < 0.1
    fprintf('\nThe model has good predictive capabilities and is well-
saturated with data.\n');
else
    fprintf('\nThe model needs more data to improve its predictive ca-
pabilities.\n');
end




%% Likelihood function - Forrester et al. [73]
function [NegLnLike, Psi, U] = likelihood(x)
    ...
end

%% Kriging prediction function - Forrester et al. [73]
function f = pred(x)
    ...
end
```

```
%% Model testing function
function [RMSE, r2] = test_model(ModelInfo, XTest, YTest)
    % Test the model performance on the testing set.
    % Inputs:
    %   ModelInfo - structure containing the trained model parameters.
    %   XTest - testing input matrix (m x k).
    %   YTest - testing output vector (m x 1).
    % Outputs:
    %   RMSE - Normalized Root Mean Squared Error.
    %   r2 - Correlation coefficient (r^2).

    Y_pred = zeros(size(YTest));       % Preallocate predictions
    for i = 1:length(YTest)
        Y_pred(i) = pred(XTest(i, :)); % Predict output for each test
input
    end

    % Calculate RMSE
    RMSE = sqrt(mean((YTest - Y_pred).^2)) / (max(YTest) -
min(YTest));

    % Calculate the correlation coefficient (r2)
    m_te = length(YTest);
    Numerator = m_te * sum(YTest .* Y_pred) - sum(YTest) *
sum(Y_pred);
    Denominator = sqrt((m_te * sum(YTest.^2) - sum(YTest)^2) * (m_te *
sum(Y_pred.^2) - sum(Y_pred)^2));
    r2 = (Numerator / Denominator)^2;
end




%% Sensitivity analysis function
function analyze_sensitivity(ModelInfo, num_points, h, fixed_var4,
fixed_var5, sortedIdx)
    % Perform sensitivity analysis for the variable var3
    % Inputs:
    %   ModelInfo - structure containing the trained model parameters
    %   num_points - number of points for gradient calculation
    %   h - small step size for central difference
    %   fixed_var4 - fixed value for variable 4
    %   fixed_var5 - fixed value for variable 5
    % Outputs:
    %   None (displays results and generates plots)

    % Reverse index for restoring original variable order
    reverseIdx = zeros(1, length(sortedIdx));
    reverseIdx(sortedIdx) = 1:length(sortedIdx);

    % Create uniformly spaced points for var3
    var3_values = linspace(2*h, 1-2*h, num_points);

    % Preallocate space for the derivatives
    derivatives = zeros(num_points, 1);

    % Calculate derivatives using central difference
    for i = 2:num_points-1
        % Forward and backward points for central difference
```

```
        X_forward = [0.5, 0.5, var3_values(i) + h, fixed_var4,
fixed_var5];
        X_backward = [0.5, 0.5, var3_values(i) - h, fixed_var4,
fixed_var5];

        % Reorder variables to original order
        X_forward_reordered = X_forward(reverseIdx);
        X_backward_reordered = X_backward(reverseIdx);

        % Calculate function values at forward and backward points
        f_forward = pred(X_forward_reordered);
        f_backward = pred(X_backward_reordered);

        % Central difference to calculate the derivative
        derivatives(i) = (f_forward - f_backward) / (2 * h);
    end

    % Find the point where the derivative of var3 is minimal (least
effect)
    [min_deriv, min_index] = min(abs(derivatives));
    best_var3_value = var3_values(min_index); % Best value for var3

    % Plot the derivative against var3 values
    figure;
    plot(var3_values, derivatives, 'k');
    xlabel('var_values');
    ylabel('derivative');
    title('Sensitivity Analysis: Derivative in order of var3');

    % Display the best value for var3
    disp(['Best value for var3 (minimum derivative): ',
num2str(best_var3_value)]);

    % Generate grid of values for var1 and var2
    var1_values = linspace(0, 1, 50);
    var2_values = linspace(0, 1, 50);
    [Var1, Var2] = meshgrid(var1_values, var2_values); % Create mesh
grid
    Z = zeros(size(Var1));   % Preallocate output matrix

    % Calculate function values over the grid for var1 and var2, fix-
ing var3, var4, var5
    for i = 1:length(var1_values)
        for j = 1:length(var2_values)
            X_eval = [var1_values(i), var2_values(j), best_var3_value,
fixed_var4, fixed_var5];
            X_eval_reordered = X_eval(reverseIdx);
            Z(i, j) = pred(X_eval_reordered); % Evaluate function at
grid points
        end
    end

    % Plot 3D surface of the objective function in terms of var1 and
var2
    figure;
    surf(Var1, Var2, Z);
    xlabel('var1');
    ylabel('var2');
    zlabel('Objective Function');
```

```
    title('3D Surface Plot of Objective Function Fixing var3, var4,
and var5');
end
```